TÉCNICO LISBOA

Two-Tier Cellular Networks: Secondary Node MIMO Configuration, Applied to LTE-A

Diogo Filipe Sequeira Martins

Thesis to obtain the Master of Science Degree in

Electrical and Computer Engineering

Supervisors: Prof. Luís Manuel de Jesus Sousa Correia

Prof. Elvino Silveira Medina de Sousa

Examination Committee

Chairperson: José Eduardo Charters Ribeiro da Cunha Sanguino

Supervisor: Prof. Luís Manuel de Jesus Sousa Correia

Members of Committee: Prof. António José Castelo Branco Rodrigues

November 2017

“To strive, to seek, to find, and not to yield”

Alfred Tennyson.

Acknowledgements

Part of the research for this thesis, including the experimental component, was performed at the Wireless Lab, University of Toronto, Canada, under the supervision of Prof. Elvino Sousa. Financial support for this research comes from the Natural Sciences and Engineering research council of Canada (NSERC) under an NSERC Discovery Grant, and an NSERC Collaborative Research and Development (CRD) Grant supported by Telus Inc. I also acknowledge the support of the Canadian Microelectronics Corporation (CMC) who provided the BEECube Equipment (MegaBEE's) and access to the Xilinx design tools used in this research. This thesis could not have been done without the support from Professor Luís M. Correia and Professor Elvino Sousa, by showing their availability from the beginning to establish the collaboration between Instituto Superior Técnico and University of Toronto.

I thank Professor Luís M. Correia for the insights on how to become a true engineer and for all the advices he gave me on the several meetings we had. Professor Luís M. Correia not only helped me in the more technical aspects of the thesis, but also on how to have a work methodology, how to present information in the most appropriate way, and the importance of honoring commitments.

My sincere gratitude goes towards Professor Elvino Sousa for his support and availability during the time I have spent in Toronto, easing my adaptation at the University of Toronto. If not for Professor Elvino Sousa's energy, ideas, patience, and full dedication and confidence in his students, I would not have felt as accomplished as a future Electrical and Computer Engineer as I was in the Wireless Lab.

To Dr. Ahmed Alsohaily for his help during the crucial stages of my thesis, always bringing me an optimistic view of the outcome of it. The knowledge and helpful discussions from Dr. Ahmed Alsohaily enabled me to work in the most autonomous way possible, while knowing that he would always be available to answer any doubts.

To Jun Qian for helping me to solve the puzzle that was the "yellow box" full of antennas, and for the wonderful moments I have spent with all the students in the Wireless Lab, filled with thoughtful discussions in any possible topic.

To all the friends I made in the five years I spent in Instituto Superior Técnico, for all the memories and experiences that will make me miss my university years, and to the always loyal friends that accompanied me since the first year of school.

At last, my final thanks are to my family for all the trust and confidence they have put in me during this journey, for giving me opportunities to invest in my future, for their patience and support, and for the education that made me who I am today.

Abstract

The objective of this thesis was to optimize the link between the primary and secondary nodes in a Two-Tier Cellular Network. The optimization was performed as an LTE-Advanced application, by developing a proposed scheme using multiple Modulation Coding Schemes per Resource Block for Link Adaptation. The proposed scheme was obtained from the calculation of the SINR for each Resource Block, differing from the wideband average value in the expected scheme. The throughput gain is evaluated in percentage by comparing the proposed and expected schemes. Three frequency selective scheduling algorithms are also evaluated, taking fairness improvement and overall cell throughput gain as performance metrics. The model was implemented in hardware for data acquisition in the secondary node, and software for channel characterization, link adaptation and scheduler for both nodes. Two scenarios were considered in terms of cell density, referring to sparse and dense deployments. An average throughput gain of 10.2% was obtained for the sparse deployment scenario considering individual reference signals, and 49.4% for 2x2 MIMO with two arrays of eight antennas. A fairness improvement of 28.9%, 80.2% and 24.1% and overall cell throughput gain of 64.0%, 41.2% and 128.5% were obtained for the Round Robin, Best CQI and Proportional Fair algorithms, respectively. For the dense deployment scenario, one achieves an average 65.0% throughput gain, although most of the capture files do not fit the requirements for the correct performance of the proposed scheme, contrary to the sparse deployment scenario.

Keywords

LTE-Advanced, Two-Tier Cellular Networks, Software Defined Radio, MIMO, RB-dependent AMC, Scheduling.

Resumo

O objetivo desta tese é a otimização da ligação entre os nós primário e secundário de uma Rede Celular de Duas Camadas, mediante uma aplicação LTE-*Advanced*. O esquema proposto foi desenvolvido para múltiplos esquemas de modulação e codificação por bloco de recurso durante a adaptação da ligação. Este esquema é obtido através do cálculo do SINR por bloco de recurso, diferindo do esquema esperado baseado na média para toda a banda. O ganho de débito binário é avaliado em percentagem, comparando os dois esquemas. A melhoria da equidade e do débito binário total por célula é avaliada para três algoritmos de calendarização seletivos em frequência. O modelo foi implementado em *hardware* para aquisição de dados no nó secundário, e *software* para a caracterização do canal, adaptação da ligação e calendarização. Dois cenários são avaliados, correspondendo a implantações esparsa e densa. Um ganho de débito binário médio de 10.2% foi obtido para a implantação esparsa considerando sinais de referência individuais, e de 49.4% para 2x2 MIMO com dois agregados de oito antenas. Uma melhoria de equidade de 28.9%, 80.2% e 24.1%, e de débito binário por célula de 64.0%, 41.2% e 128.5% foram obtidos para os algoritmos *Round Robin*, *Best CQI* e *Proportional Fair*, respetivamente. Relativamente à implantação densa, um ganho de débito binário médio de 65.0% foi obtido, porém a maioria dos ficheiros de captura não cumpre os requisitos para o desempenho correto do esquema proposto, contrariamente ao cenário de implantação esparsa.

Palavras-chave

LTE-*Advanced*, Redes Celulares com Duas Camadas, Rádio Definido por *Software*, AMC por Bloco de Recurso, Calendarização.

Table of Contents

List of Figures

List of Tables

List of Acronyms

2G	2nd Generation
3G	3rd Generation
3GPP	3rd Generation Partnership Project
4G	4th Generation
ACK	Acknowledgement
AMC	Adaptive Modulation Code
ARFCN	Absolute Radio-Frequency Channel Number
AWGN	Additive White Gaussian Noise
BER	Bit Error Ratio
BLER	Block Error Rate
BPS	BEECube Platform Studio
BRAM	Block Random Access Memory
CA	Carrier Aggregation
CAZAC	Constant Amplitude Zero Auto-Correlation
CC	Component Carrier
CN	Core Network
CoMP	Coordinated Multipoint
CP	Cyclic Prefix
CQI	Channel Quality Indicator
CS	Circuit Switch
CSI	Channel State Information
D2D	Device to Device communications
DL	Downlink
DMA	Direct Memory Access
EDGE	Enhanced Data rates for GSM Evolution

eNB	evolved Node-B
EPC	Evolved Packet Core
EPS	Evolved Packet System
E-UTRAN	Evolved Universal Terrestrial Radio Access Network
FDD	Frequency Division Duplexing
FFT	Fast Fourier Transform
FIFO	First-In First-Out
FPGA	Field-Programmable Gate Array
GBR	Guaranteed Bit Rate
GPIO	General Purpose Input Output
GPRS	General Packet Radio Service
GPS	Global Positioning System
GSM	Global System for Mobile Communications
HeNB	Home eNB
HeNB-GW	Home eNB Gateway
IFFT	Inverse Fast Fourier Transform
IMS	IP Multimedia Subsystem
IoT	Internet of Things
ITU-R	International Telecommunication Union Radiocommunications Sector
LTE	Long Term Evolution
LTE-A	Long Term Evolution Advanced
MCS	Modulation Coding Scheme
M2M	Machine to Machine communications
MME	Mobility Management Entity
MMSE	Minimum Mean Square Error
MRC	Maximal Ratio Combining
MT	Mobile Terminal
MU-MIMO	Multiple User MIMO
NACK	Non-Acknowledgement
OFDM	Orthogonal Frequency Division Multiplexing

OFDMA	Orthogonal Frequency Division Multiple Access
PAPR	Peak-to-Average Power Ratio
PBCH	Physical Broadcast Channel
PCEF	Policy and Charging Enforcement Function
PCFICH	Physical Control Format Indicator Channel
PCRF	Policy and Charging Rules Function
PDB	Packet Delay Budget
PDCCH	Physical Downlink Control Channel
PDN-GW	Packet Data Network Gateway
PDSCH	Physical Downlink Shared Channel
PER	Packet Error Loss Ratio
PHICH	Physical Hybrid ARQ Indicator Channel
PL	Programmable Logic
PMCH	Physical Multicast Channel
PMI	Precoding Matrix Indicator
PRACH	Physical Random-Access Channel
PS	Processing System
PSS	Primary Synchronization Signal
PUCCH	Physical Uplink Control Channel
PUSCH	Physical Uplink Shared Channel
QCI	Quality Channel Indicator
QoE	Quality of Experience
QoS	Quality of Service
RAN	Radio Access Network
RB	Resource Block
RE	Resource Element
RF	Radiofrequency
RI	Rank Indicator
RN	Relay Node
RS	Reference Signal

SC-FDMA	Single Carrier Frequency Division Multiple Access
S-GW	Serving Gateway
SINR	Signal to Interference plus Noise Ratio
SR	Software Register
SSS	Secondary Synchronization Signal
STR	Simultaneous Transmit and Receive
SU-MIMO	Single User MIMO
TDD	Time Division Duplexing
TTI	Transmission Time Interval
TTR	Time-division Transmit and Receive
UE	User Equipment
UL	Uplink
UMTS	Universal Mobile Telecommunications System
UTRAN	Universal Terrestrial Radio Access Network
VoLTE	Voice Over LTE
VPL	Vehicle Propagation Loss
X2-GW	X2 Gateway
XGE	10 Gigabit Ethernet
ZF	Zero Forcing

List of Symbols

α	Attenuation Factor
Δf_{RB}	Resource Block Bandwidth
Δt_c	Timing Gap between Captures
ρ_{IN}	Signal to Interference plus Noise Ratio
$a_{k-CRS,l-CRS}^{(p)}$	Value of cell-specific reference signal mapped on resource element $(k-CRS, l-CRS)$ for antenna port p.
$c(n)$	Pseudo-random sequence
$c_{0,1}(n)$	M-sequences derived from the Sector Identity
C_c	Spectral Efficiency
$d(n)$	62-length sequence for SSS generation
$d_u(n)$	62-length sequence for PSS generation
f_{CLK}	System's clock frequency
f_s	Sampling Frequency
F_{index}	Fairness Index
l	OFDM symbol number within a slot
L	Cyclic Prefix Number of Samples
k^*	Allocated Secondary Node
k_B	Boltzmann Constant
$m_{0,1}$	Indices derived from the Physical Layer Cell Identity
$n(k)$	Counter Value at Capture k
n_s	Slot Number

N	FFT Size
$N_{ID}^{(1)}$	Physical Layer Cell Identity Group
$N_{ID}^{(2)}$	Sector Identity
N_{ID}^{CELL}	Physical Cell Identity
N_{RB}^{DL}	Number of Downlink Resource Blocks
$N_{RB}^{\max,DL}$	Maximum Number of Resource blocks per Bandwidth
$N_{RF,RB}$	Noise Power per Resource Block
$N_{\sec nodes}$	Number of secondary nodes
N_{sc}^{DL}	Number of Downlink Subcarriers
p_{DATA}	Pattern Data
$P_{r,RB}^{ID}$	Received Power per Resource Block for Physical Cell Identity
$r(n)$	Received OFDM stream
$r_{l,ns}(m)$	Value of Reference Signal in symbol l and slot n_s
$r_{k-CRS,l-CRS}^{(p)}$	Received demodulated value of cell-specific reference signal mapped on Resource Element $(k-CRS, l-CRS)$ for antenna port p
R_{b,RB_i}	Throughput per Resource Block
$R_{b,s}^{act}$	Expected Scheme Actual Throughput per slot
$R_{b,s}^{act-opt}$	Proposed Scheme Actual Optimal Throughput per slot
$R_{b,s}^{\exp}$	Expected Scheme Throughput per slot
$R_{b,s}^{G}$	Throughput Gain per slot
$R_{b,s}^{opt}$	Proposed Scheme Optimal Throughput per slot
$R_{k,n}(t)$	Requested Data Rate of each UE/secondary node k in PRB n for slot t
$s_{0,1}^{(m_0,m_1)}(n)$	M-sequences

$S(\rho_{IN})$	Shannon Bound
t_c	Window size for Proportional Fair Scheduling Algorithm
T	Temperature
$T_{k,n}(t)$	Average Throughput of each UE/secondary node k in PRB n for slot t within a past window t_c length
$z_{0,1}^{(m_0,m_1)}(n)$	M-sequences

List of Software

BEEcube Platform studio	Hardware/Software co-development tool for MATLAB
Google Maps	Geographical plotting tool
MATLAB	Numerical computing environment
Microsoft Excel 2016	Spreadsheet Editor
Microsoft Word 2016	Word processor
Paint.NET	Image Editor

Chapter 1

Introduction

This chapter provides the framework of this thesis, regarding its importance in the current mobile communications networks, presenting the motivation and scope of the work to be developed. The thesis' structure is then detailed, summarizing the aspects that are dealt with.

1.1 Overview and Motivation

The industry of telecommunications changed when mobile communications were introduced. The possibility to contact anyone, anywhere in the world at any time was a concept rapidly embraced globally. This was the first service offered by 1st generation (1G) mobile communication systems. Being an analog cellular system, it was not robust against interference, which was amplified with the lack of standardization of the different countries. In the digital era, Global System for Mobile Communications, GSM, also known as a 2nd generation (2G), appeared as a circuit-switch solution for full duplex voice communications. Years after the first deployments were finished, the General Packet Radio Service (GPRS) and Enhanced Data rates for GSM Evolution (EDGE) offered the first data services in a mobile communication system by using packet switch. Universal Mobile Telecommunications System (UMTS), belongs to the 3rd generation (3G) of mobile communications as a somehow improved version of GSM, offering higher data rates and an improved air interface.

LTE's core network is an evolution of the GSM/GPRS core network employed by the previous generations systems. This evolution is known as System Architecture Evolution (SAE), where the Radio Access Network (RAN) and the Core Network (CN) from the legacy systems were revisited, resulting in the Evolved Packet System (EPS).

ITU's requirements for the 4th Generation (4G) were:

- Increased peak data rate, Downlink (DL) 3 Gbit/s, Uplink (UL) 1.5 Gbit/s;
- Higher spectral efficiency, from a maximum of 16 bit/s/Hz in Release 8 to 30 bit/s/Hz in Release 10;
- Increased number of simultaneously active subscribers;
- Improved performance at cell edges.

As of 3GPP's Release 10, LTE became known as LTE-Advanced (LTE-A), although they are the same technology. 3GPP determined that the ITU Requirements for 4G would be met with the introduction of LTE-A's new features [3GPP16b]. LTE-A shares the same network architecture of LTE, however, the support of relay nodes (RNs) and heterogeneous networks became one of the main technologies under consideration for further 3GPP Releases.

From Cisco's forecast, represented in Figure 1.1, LTE already supports a major part of the global mobile data traffic, being foreseen for 2017 a 72% traffic share, greatly exceeding 3G's share of 27% and the almost non-existing share of 2G.

LTE- A, with its elevated capacity and reduced latency, enables a whole range of real-time multimedia services, such as high-quality video conferencing, multi-user online gaming over IP, high definition video-audio streaming (Mobile Live TV) and other interactive applications [Mart13] increasing mobile data traffic. This growth can also be related with the current trend of Internet of Things (IoT). The growth of Machine-to-machine (M2M) or Device-to-device (D2D) communications will use a huge number of

devices, the rate of adoption of these devices using LTE being constantly increasing [3GPP16c].

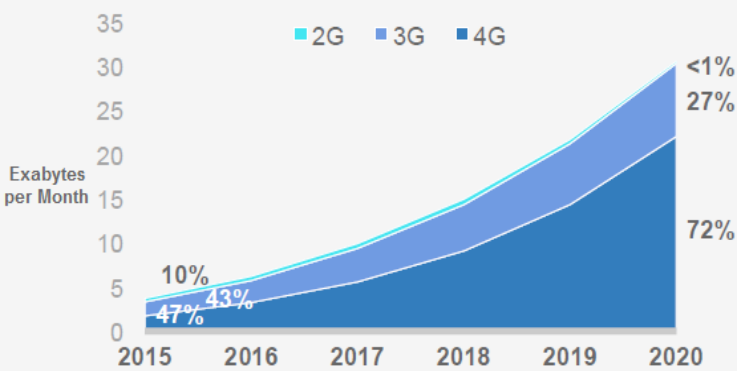

Figure 1.1 – Mobile data traffic forecast for each generation system from 2015 to 2020 (adapted from [Cisc16]).

The evidence of mobile data traffic growth increases the demand for a higher capacity, while the increase of the number of devices creates the need for a higher coverage, Figure 1.2. To handle this growth for future generation wireless networks, several techniques are under study not only to increase the maximum throughput in dense traffic areas, but to also to enhance coverage in sparse areas, such as rural ones.

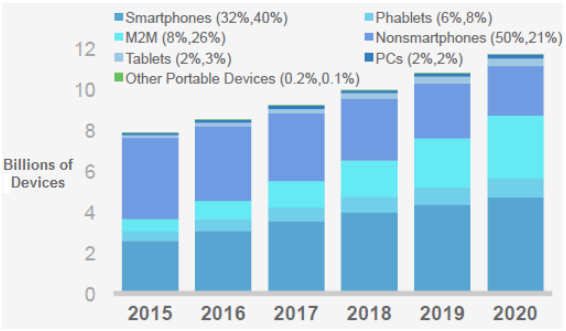

(a) Connected devices growth (53% CAGR).

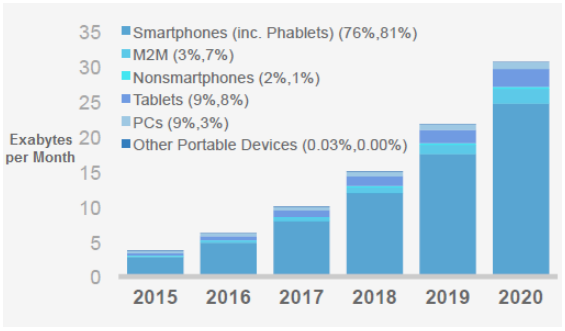

(b) Mobile traffic per device growth (8% CAGR).

Figure 1.2 – Forecast of connected devices and mobile traffic per device growth from 2015 to 2020 (adapted from [Cisc16]).

In this thesis, one studies the link between the primary and secondary nodes in a Two-Tier Cellular Networks. Two-Tier Cellular Networks, by introducing a second tier of base stations, offer advantages in terms of capacity, coverage and a smarter resource allocation scheme to serve users more effectively.

The link between the tiers in a Two-Tier Cellular Network is critical in terms of system optimization, because it allows for the use of multiple antennas between the two nodes. To ensure the connectivity for devices, smart access points and user equipment within both cellular network can be simplified by using such wireless backhaul. Additionally, the potential costs for the operators can be minimized, as a wired backhaul is no longer needed between the multiple terminals, which requires a great investment by operators [RaSo16].

By considering that peaks of traffic form in clusters of users, one can benefit from the hierarchization of

a cellular network. By having dedicated nodes serving clusters of users, for example in public transportation and shopping centers, one can guarantee the Quality of Service required in such conditions. Given that the backhaul link is often not adequate to appropriately carry out the necessary network's load balancing, Massive MIMO can be a profitable and efficient solution for this backhaul.

LTE-A's support for Two-Tier Cellular Networks and higher order Multiple Input Multiple Output (MIMO) systems can be explored to overcome the traffic growth, although they still present some drawbacks in terms of complexity, interference and mobility issues. In a Two-Tier Cellular Network, the communication from a base station, also called a primary node, to end-user equipment occurs through an intermediary station that one refers to as a secondary node.

The scope of this thesis focuses on techniques to optimize this link in terms of secondary node multiple antenna configuration. The work being developed aims to the implementation of a multiple antenna receiver using a BEEcube prototyping platform, MegaBEE as a secondary node of a Two-Tier Cellular Network. The secondary node main functions in this analysis are the same as a regular UE, however possessing a set of characteristics in terms of processing power and space conditions that enables the use of multiple antennas.

The link under optimization is the one between the primary and secondary nodes. The proposed scheme optimization of throughput/capacity performs Link Adaptation/Adaptive Modulation and Coding (AMC) considering multiple Modulation Coding Schemes (MCS) for individual PRBs within a slot. The MCS applied for the multiple users in the network was a topic of discussion in the first standards of LTE [NFMN06], by either assigning the same MCS for all the RBs allocated to a secondary node, or independent MCS for the assigned RBs. The usage of independent MCS for assigned RBs was dropped as the small throughput improvement was not worth the additional overhead the network would have to endure, in the absence of transmission power control.

The proposed scheme aims to take advantage of the overall properties of a secondary node when compared to a regular UE. The secondary node model employed in this analysis is static, thus the channel impulse response is expected to be steady without drastic changes along time. By employing multiple antennas at the secondary node, one can achieve higher modulation coding schemes, improving system capacity. By having these properties, and by assuming that a secondary node possesses a greater computational power than a regular UE, the procedure of AMC using independent MCS in assigned RBs can be considered as a valid option to improve the link between the primary and secondary nodes.

To reduce the signaling overhead created by adopting multiple modulation coding schemes per resource block, the proposed scheme determines an SINR threshold according to the measured CQIs of the first demodulated slot of an LTE frame, applying the same MCSs for the following slots. Sudden changes in the channel behavior will result in the update of the MCS to be adapted for the following slots proceeding the fluctuation.

When considering a Two-Tier Cellular Network, the number of secondary nodes can be assumed to be lower than regular UEs on a regular standard network. This assumption greatly reduces the scheduling

complexity for the eNB when performing a scheduling procedure to secondary nodes within the cell. Scheduling algorithms aim to implement the resource allocation between the several UEs/secondary nodes within the network and can be built to optimize several parameters. The most common performance parameters optimized using a scheduling algorithm are in terms of scheduler complexity, overall cell capacity/throughput and allocation fairness between users.

The main output of this work is a great throughput improvement when considering the proposed scheme, however, it is too dependent on radio channel steady conditions. As the proposed scheme updates the MCS during variations of the reported CQI, the effect of channel fluctuations dictates the scheme's performance due to the added signaling.

1.2 Report Structure

This report is composed of 5 chapters, including the present one and four annexes.

Chapter 2 presents an overview of the theoretical aspects related to this thesis. At the beginning of this chapter, the general aspects of LTE-Advanced are detailed, regarding network architecture and radio interface. Then, an overview of the multiple antennas enhancement techniques is presented, such as MIMO and beamforming. Two-Tier Cellular networks drawbacks and improvements follow, a review of the state of the art related to this thesis being done at the end of this chapter.

Chapter 3 covers the model development for the optimization of the link between the primary and secondary nodes. A brief overview of the model structure is presented, followed by the secondary node development, explaining the fundamental operations performed at the secondary node in terms of data acquisition, channel characterization, and intermediate measurements necessary to the calculation of the performance parameters. Performance parameters are then determined in terms of the proposed and expected schemes throughputs. Two additional performance parameters are considered, pertaining to the comparison between the two schemes. The first parameter refers the throughput gain one obtains considering the proposed scheme compared to the expected one with only one antenna, ending with an evaluation of throughput gain considering receiver diversity with up to eight antennas. The second parameter aims to evaluate the fairness in the scheduling algorithms, when one allocates resources on the resource block level and on the sub-band level. With the performance parameters correctly defined, the model implementation ensues both in hardware and software for the secondary node and only in software for the primary one. After model implementation, the functionality assessment is performed in all the modules composing the model.

Chapter 4 presents the thesis results and its analysis, for the described scenarios. An in-depth study is performed in the reference scenario, regarding the optimization of the link between the primary and secondary node using multiple antennas. In a first phase, one evaluates the performance of the two throughput schemes when considering the received power per resource block as being calculated by the average of the reference signals within the resource block. It follows by a similar study, but with the

received power calculation being based on the individual reference signals within the resource block. As expected, since the former phase has a better performance than the first one, one considers multiple antennas to further enhance the performance for individual reference signals. Additionally, in this first scenario, the scheduling algorithms are put into test and their performance is evaluated comparing again the proposed expected schemes. A different scenario is evaluated, and the impact of the performance parameters is studied based on this change, but only in terms of the two throughput schemes as the scheduling algorithms is expected not to change drastically in the new scenario.

The main conclusions of the thesis are presented in Chapter 5, regarding the obtained results in Chapter 4 and the overall summary of the document. Improvement suggestions pertaining to data acquisition methods and hardware calibration are also presented at the end of this chapter, concluding with future work aimed to examine other aspects relevant to the topics in this thesis.

Annex A presents additional data acquisition methods not used in the final application and its assessment by simulations is done in Annex B. The cells information is presented in Annex C, in the form of screen captures using the embedded test field menu in an iOS cell phone. To conclude, in Annex D the obtained absolute results for the throughput schemes are presented for the two evaluated scenarios.

Chapter 2

Fundamental Concepts and State of the Art

This chapter examines the basic aspects of LTE-A, mainly focusing on enhanced multiple antenna transmission techniques, employed in its radio interface. An overview on Two-Tier Cellular Networks is then presented, discussing the different types of architectures and a performance analysis. The end of this chapter is dedicated to an analysis of the state of the art.

2.1 LTE-Advanced

2.1.1 Network architecture

This subsection addresses LTE's network architecture based on [3GPP16a], [3GPP16d], [DaPS14], [Cox12] and [OSRF09].

There are 4 main components in LTE's network architecture, namely Services, the EPS composed of the Evolved Universal Terrestrial Radio Access Network (E-UTRAN) and the Evolved Packet Core (EPC), and finally the User Equipment (UE) as represented in Figure 2.1.

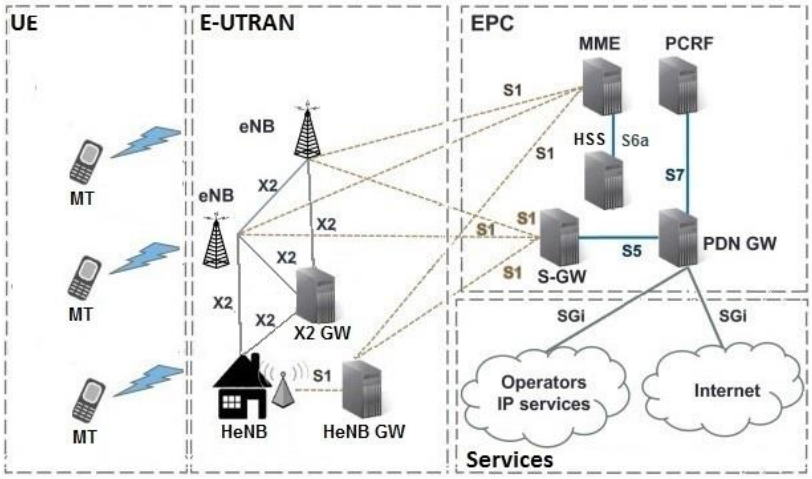

Figure 2.1 – LTE-A System Architecture (adapted from [TrSS12]).

In terms of functionality, the 4 main components have different roles in the network architecture. Regarding the Services component, which connects to the EPS, it allows the access to the IP multimedia subsystem (IMS), which provides services like Voice Over LTE (VoLTE) offered by operators. It also allows access to the Internet, thus opening a huge range of services.

The EPC component communicates with packet data networks in the outside world such as the internet, private corporate networks or the IMS. It is also the connection point with legacy systems, such as GSM and UMTS. The main element nodes of EPC, Figure 2.1, are the Packet Data Network Gateway (PDN GW), the Serving Gateway (S-GW) and the Mobility Management Entity (MME).

Through the SGi interface, the EPC contacts with the "outside world", with the PDN-GW acting as a point of contact, exchanging data with one or more external devices or packet data networks. The interface S7 enables the connection between the PDN GW and Policy and Charging Rules Function (PCRF). Throughout a Policy and Charging Enforcement Function (PCEF), part of the PDN GW, it is authorized the policy and charging treatment that a service data flow will receive.

The S-GW acts as a router, forwarding data between base stations, also known as evolved Node-B

(eNB) via the S1 interface, and the PDN GW via the S5 interface. The S-GW acts as a mobility anchor, namely when a Mobile Terminal (MT) changes the eNB from which it is currently connected.

Mobility control, security issues and legacy systems compatibility is handled by the MME using signaling messages exchanged externally, such as the UE and eNB, and internally in the EPC. Through the S6a interface, the MME connects with the Home Subscriber Server (HSS) a database that concatenates the functions of the Home Location Register (HLR) and the Authentication Centre (AuC) present in GSM and UMTS. The HSS is responsible for the storing and updating the database containing all user subscription information, while also generating security information from user identity keys.

Contrary to the previous system implementation of the radio access network (UTRAN for UMTS), in LTE this is handled by the E-UTRAN, which has as its sole component the eNBs. The two main functions of E-UTRAN are first sending and receiving messages of the MTs, in DL and UL, respectively using LTE's air interface, and second low-level control of the MT, such as handover commands, through signaling messages. Each eNB is connected to the EPC by the S1 interface and can be connected between each other via the X2 interface for signaling and packet forwarding purposes (this interface is optional as S1 can handle all these functions). Each MT can only be connected to one eNB, eliminating the soft handover state experienced in UMTS.

In a heterogeneous network, the E-UTRAN architecture may deploy a Home eNB gateway (HeNB-GW) to connect Home enBs (HeNBs), such as femto-cells, to the EPC via the S1 interface. In this case the HeNB-GW appears to the MME as a eNB whereas for the HeNB the HeNB-GW appears as a MME. The HeNBs and eNBs can also be linked between each other via the X2 interface, being that both nodes can connect to the X2 Gateway (X2-GW).

2.1.2 Radio interface

In this subsection, LTE's radio interface is detailed, concluding with an overview on the new features launched with LTE-A. It is based on the works of [Cox12], [DaPS14], [GRMM10] and [Mart13].

Like GSM and UMTS, bidirectional transmission of information in LTE and LTE-A between the eNB and MT can be achieved using both time division duplexing (TDD) and frequency division duplexing (FDD). As of 3GPP's Release 12, there are 31 operating bands for LTE with only 11 for TDD, however not all bands are used by the operators in each country, as they are auctioned by the communications regulator from the respective region/country.

Unlike GSM and UMTS, LTE uses Orthogonal Frequency Division Multiplexing (OFDM) as a base for its multiple access techniques for both DL and UL. This technique enables the transmission of information by dividing it into several parallel sub-streams, sending each sub-stream on a different frequency known as sub-carrier.

In DL, the technique used to handle multiple access is Orthogonal Frequency Division Multiple Access (OFDMA), which is a suitable solution to handle high data rates, possessing low sensitivity to interference and fast fading, and a reduced control information overhead. The main difference between OFDM and OFDMA is how the subcarriers are assigned to each user. While OFDM only allocates

subcarriers to each user in the time domain, OFDMA can allocate a subcarrier in both time and frequency domain.

In LTE, the physical resource that is allocated to a user is known as a Resource Block (RB). A RB is composed in frequency by 12 sub-carriers, spaced by 15 kHz, and in time by 1 slot with the duration of 0.5 ms as represented in Figure 2.2. Underlying an RB is the basic unit of resource allocation, the Resource Element (RE), comprising 1 OFDM Symbol for 1 sub-carrier. For each symbol transmitted, it is appended a Cyclic Prefix (CP) to mitigate intersymbol interference. The cyclic prefix is generated by copying the ending part of a OFDM symbol, being then appended to its beginning.

A 10 ms LTE FDD frame is composed of ten subframes of equal length, each subframe containing two 0.5 ms slots with six or seven OFDM symbols depending on the length of the cyclic prefix. An LTE TDD frame is also composed of ten subframes, however, because the bandwidth is share between UL and DL, there is an allocation of subframes to UL and DL. For this reason, there are 7 different patterns of UL and DL subframe allocation for a TDD frame. Each frame also contains special subframes, containing a portion of DL transmission at the start of the subframe (the Downlink Pilot Time Slot, DwPTS), a portion of unused symbols in the middle of the subframe (the Guard Period) and a portion of UL transmission at the end of the subframe (the Uplink Pilot Time Slot, UpPTS).

By increasing the bandwidth, one can increase the number of resource blocks that can be assigned to each user. On the other hand, depending on the modulation scheme, the number of transmitted symbols increases, which results on a higher bit-rate available for each user. The modulation schemes used in LTE/LTE-A are QPSK, 16QAM and 64QAM. In 3GPP's Release 12 there is support for 256QAM in DL.

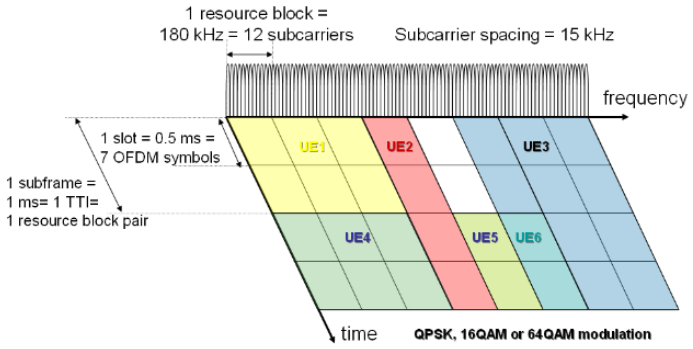

Figure 2.2 – Resource block allocation in OFDMA (extracted from [GeRK12]).

One of the disadvantages of OFDMA is the increase of the Peak-to-Average Power Ratio (PAPR) as the number of sub-carriers increases. The increase of PAPR requires a higher complexity to the amplifier used in the transmission of the signal, something that is unpractical in mobile devices due to their reduced battery life. Taking this issue into account, in UL the multiple access technique is not OFDMA, being Single Carrier Frequency Division Multiple Access (SC-FDMA) the technique employed.

Contrary to OFDMA, which works with separated transmitted subcarriers, SC-FDMA works with jointly transmitted subcarriers. This means that each symbol in SC-FDMA is not assigned to a subcarrier like OFDMA. By using multiple sub-carriers, a linear combination of modulated data symbols, is transmitted at the same time instant, represented in Figure 2.3 for a QPSK modulation scheme.

From Figure 2.3, one can conclude that the two multiple access techniques can transmit the same amount of data symbols while using the same bandwidth and at the same time period. The reason SC-FDMA is not used in DL is mainly because of the performance when dealing with multiple users and its resistance to fading when compared to SC-FDMA, handling with higher data rates. In terms of power consumption, in DL the elevated PAPR is not an issue, because an eNB is not power limited and can handle the transmitter complexity needed to cope with this issue. In UL, due to the power constraints it simply cannot handle the elevated values of PAPR.

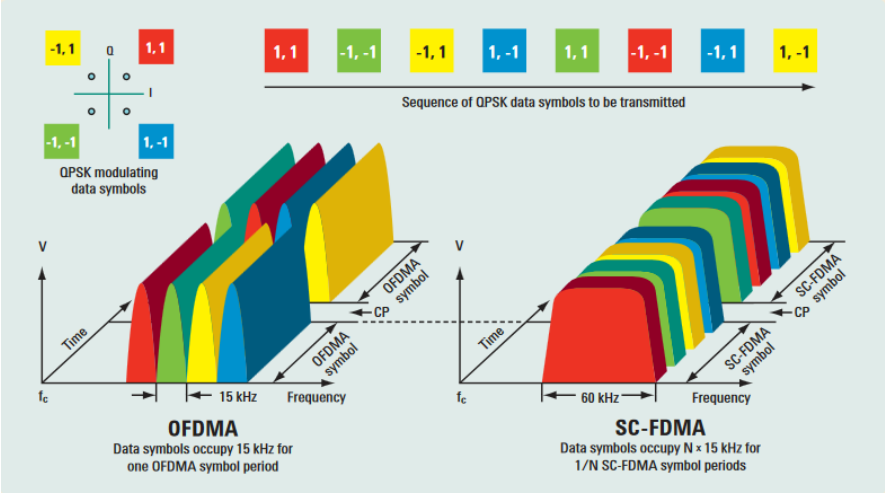

Figure 2.3 – Transmission of QPSK data symbols using OFDMA and SC-FDMA (extracted from [Rumn08]).

An LTE radio frame is composed of 10 sub-frames, also known as Transmission Time Intervals (TTIs), where each sub-frame has a duration of 2 slots, totaling 10 ms for the frame duration. Each radio frame contains reference signals, control information and data transmission used to deploy physical and control channels. The main physical channels for both UL and DL communications are represented in Table 2.1 and Table 2.2.

Other than the network architecture support for RNs and heterogeneous networks, LTE-A introduced new improvements in the radio interface. The major improvements were the increase of bandwidth (which leads to a higher capacity), coverage, quality of service, network utilization and interference management using Carrier Aggregation (CA), Coordinated Multipoint (CoMP) and multiple antennas enhancement techniques.

Table 2.1 – LTE Uplink Physical Channels (adapted from [GRMMT10]).

	Channel	Purpose
UL	Physical Uplink Shared Channel (PUSCH)	Carry user data (UL)
	Physical Uplink Control Channel (PUCCH)	Carry ACK/NACK associated with DL, scheduling request, and feedback of DL channel quality and precoding vector
	Physical Random Access Channel (PRACH)	Carry random access transmission

Table 2.2 – LTE Downlink Physical Channels (adapted from [GRMMT10]).

	Channel	Purpose
DL	Physical Downlink Shared Channel (PDSCH)	Carry user data (DL)
	Physical Broadcast Channel (PBCH)	Carry broadcast information
	Physical Multicast Channel (PMCH)	Carry multicast services
	Physical Control Format Indicator Channel (PCFICH)	Indicate the size of the control region in number of OFDM symbols
	Physical Hybrid ARQ Indicator Channel (PHICH)	UL Acknowledgement (ACK)/Non-Acknowledgement (NACK) information
	Physical Downlink Control Channel (PDCCH)	Carry DL scheduling assignments and UL scheduling grants

The principle of CA is to aggregate carriers from LTE's TDD and FDD bands, increasing the overall bandwidth and thus increasing the available capacity for each user. Each carrier is known as component carrier (CC), being possible to aggregate up to five of them. The available bandwidths in LTE are represented in Table 2.3 according with number of sub-carriers (N_{sub}) and number of RBs (N_{RB}).

Table 2.3 – Bandwidths, Number of Subcarriers and Resource Blocks in LTE (adapted from [Corr16]).

Bandwidth [MHz]	1.4	3	5	10	15	20
N_{sc}^{DL}	72	180	300	600	900	1200
N_{RB}^{DL}	6	15	25	50	75	100

Each individual component carrier can have different bandwidths, however by aggregating five carriers with 20 MHz bandwidth, a maximum bandwidth of 100 MHz is obtained. There are two scenarios of CA, intra- and inter-bands, each one of them being capable of using up to five carriers. In intra-band aggregation, CCs can either be aggregated in a contiguous or non-contiguous way if there is a gap between the CCs. The last scenario is inter-band when the CCs belong to different bands. The main objective of CoMP is to improve network performance at cell edges by having coordinated transmitters, in the case of LTE-A eNBs, transmitting data to the same sector. This technique is to be used in cell edges due to the difficulty of maintaining a constant stream of data due to poor coverage. This improvement on network performance falls into two categories:

- **Joint Transmission:** two eNBs transmit to one UE in the same radio sub-frame;
- **Dynamic Point Selection:** two eNBs are ready to transmit, however only one eNB can transmit an entire radio sub-frame.

The challenge of CoMP is to have a very low level of the latency that is created due to the communication of the eNBs and consequent processing that needs to be undertaken.

2.2 Multiple Antenna Enhancement Techniques

From the main multiple antennas enhancement techniques, the one that is dealt with in more detail in this section is spatial multiplexing, the base of Multiple Input Multiple Output (MIMO) wireless systems, and beamforming. The works of [GSSS03], [Cox12] and [DaPS14] were the base for the overview of MIMO and spatial multiplexing while [LETM14], [LLSA14] and [RPLL13] provide the framework for Massive MIMO. The spatial multiplexing fundamental concept is to transmit several data streams through different multiple antennas separating them in the receiver by the means of signal processing, as represented in Figure 2.4. This technique increases data rate proportionally to the minimum number of antennas used in the transmission or in the reception. The ability of turning multipath propagation as an advantage to the communication system is one of the main advantages of this technique.

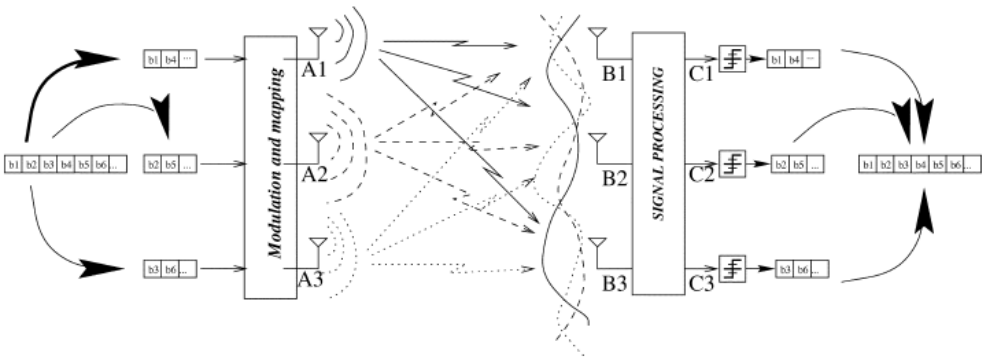

Figure 2.4 – Spatial multiplexing with three transmission and three reception antennas (adapted from [GSSS03]).

From a high rate bit stream, three separate bit streams with a third of the bit-rate are modulated and mapped to be transmitted at the same time from the three antennas. The signals that are sent from the three antennas are respectively A1, A2 and A3. As they are launched on the wireless channel, they naturally mix together causing interference. Due to the characteristics of the surrounding environment, the signals are attenuated suffering the effect of random noise as well. What the receiving antennas receive is respectively B1, B2 and B3. Proceeding the next stage after reception, the sequences B1, B2 and B3 must be processed to obtain C1, C2 and C3, and then de-mapped and demodulated to finally obtain the three separate bit streams that were transmitted.

The signal processing unit can work with feedback from the transmitter (closed loop spatial multiplexing), or without it (open loop spatial multiplexing). In an open loop situation after receiving B1, B2 and B3, the receiver's goal is to identify the mixing channel matrix elements using reference symbols (pilots) sent from the transmitter. By sending the pilots to the receiver one at a time, it allows the calculation of each of the mixing matrix elements. When all the matrix elements are identified, the receiver can now estimate

the individual bit streams, a process that works the same way as finding three unknowns from a linear system of three equations.

Open loop spatial multiplexing has some flaws, as situations can occur when the matrix mixing elements are such that cancel out the symbol estimation of the receiver. To resolve this issue, closed loop spatial multiplexing is used, where the receiver after estimating the mixing channel matrix elements generates a Rank Indication (RI), which indicates the number of bit streams that it can successfully receive, and a Precoding Matrix Indicator (PMI), feeding both back to the transmitter. Collectively, the PMI and RI, together with the Channel Quality Indicator (CQI), which describes the Signal to Interference plus Noise Ratio (SINR) in terms of frequency, form the Channel State Information (CSI). The PMI controls a precoding step in the transmitter to ensure that the signals reach the receiver without cancellation. Finally, at the receiver, there is an additional post-coding step that reverses the effect of precoding, including the soft decision estimation step from earlier, thus allowing to estimate the individual bit streams. This technique is also known as Single User MIMO (SU-MIMO), because each eNB transmits several data streams using multiple antennas directed to one single user. Multiple User MIMO (MU-MIMO) allies spatial multiplexing with an additional complexity on the receiver's side, to suppress interference, for transmitting to multiple users using the same time-frequency resource, improving the overall capacity of a given cell. It is however not a scalable technique as it was originally envisioned, because for it to operate properly, it requires roughly the same number of transmitting and receiving antennas while using FDD, which requires additional costs to the network's radio interface.

In LTE-A, it is currently available an 8x8 MIMO scheme, however the trend is to increase the number of antennas, usually referred as Massive MIMO. While MU-MIMO originally envisioned FDD as its duplexing technique, canonical Massive MIMO uses TDD. The technology offers huge advantages in terms of energy and spectral efficiency and a drastic increase on the system's capacity. It also allows for the use of low-cost hardware at both the base station and the mobile terminal side.

The fact that data in MIMO is transmitted over a matrix instead of a vector (such as Single Input Single Output systems) unveils some properties regarding the asymptotics of random matrix theory. By increasing the number of antennas in a MIMO system, the mixing channel matrix elements starts to approach a deterministic function instead of a random one. On the other hand, as the order of the matrix increases, some matrix operations can be done rather quickly by using series expansion techniques, as high order matrixes tend to be well conditioned. These properties allow the use of simple beamforming strategies to pre-code the vast amounts of data in real time such as Maximal Ratio Combining (MRC), Zero Forcing (ZF) and Minimum Mean Square Error (MMSE). Based on the asymptotic arguments regarding random matrix theory, it is demonstrated that the small-scale fading (slow fading), thermal and other uncorrelated noise in the system are averaged out.

Although the benefits of Massive MIMO seem evident, there is still huge drawbacks to be worked on. The main limitations for the full deployment of this system are in terms of interference management, hardware implementation and impairments, computational complexity, realization of distributed processing algorithms, and synchronization of the antenna units. Other applications for Massive MIMO can be as wireless backhaul for Two-Tier Cellular Networks.

Other multiple antenna enhancement technique under study is beamforming, which, by controlling the phase and amplitude of each base station antenna, creates a constructive interference directed towards mobile terminals, thus increasing the base station range. This process can be done electronically by sending the signal from each transmitter with different delays, creating the beam steering without rotating or moving antenna elements. The amplitude of the lobe can be controlled as well and so, one can effectively manage the direction of the main lobe and nulls according to the environment.

Unlike other multiple antenna enhancement techniques where high correlation is an issue, creating the need to separate each antenna element, such as transmit diversity and spatial multiplexing, beamforming has a better performance when signals are highly correlated. In LTE-A, with OFDMA, it is also possible to implement artificial beams, pointing at different directions by using different sub-carriers.

As the number of antennas increases, to fully exploit the advantages of beamforming, the implementation tends to be unfeasible, both in terms of equipment, complexity, power consumption and associated costs. Fully digital beamforming has the disadvantage of requiring the same number of digital transceivers for each antenna element. To overcome this issue, a hybrid solution where each transceiver connects with the multiple active antennas, and the signal phase on each antenna is controlled by analog phase shifters. This technique allows the beamforming partition between the digital and radiofrequency (RF) domains, achieving a flexibility and cost tradeoffs balance, while still fielding a system that meets the required performance parameters.

2.3 Two-Tier Cellular Networks

2.3.1 General Aspects

Standard cellular networks are composed of several base stations that communicate with several mobile terminals, in each cell. Each base station possesses the same characteristics regarding transmission power levels, access techniques, antenna radiation patterns, sensitivity, among other terms to serve end terminals in the same way at each cell. One of the major drawbacks in this deployment occurs at cell edges, where the signal power is already too attenuated due to the elevated distance from cell center, creating problems in both coverage and capacity.

To prevent this issue, a hierarchy-based cellular network is proposed where low power nodes, also known as small cells and relay nodes, are distributed throughout the conventional macro-cellular network. Small cells are deployed in strategic zones, namely areas with low coverage or on the contrary, areas with high coverage but with elevated traffic. The name given to this type of hierarchy-based architecture is Two-Tier Cellular Networks, where the macro-cells tier is referred to as primary node and small cells or relay node tier as secondary one. In a Two-Tier Cellular Network, small cells share the same frequency spectrum with the macro-cell ones, being that in OFDMA based systems like LTE, one can allocate orthogonal sub-carriers between the macro- and small cells.

Considering the coverage range of a cell, one can classify 4 types of cells, macro-, micro/metro-, pico- and femto-cells from the highest coverage radius to the lowest [3GPP16e]. In Table 2.4, a summary on the types of deployed cells is presented.

Table 2.4 – Cell types summary.

Type	Coverage radius [km]	Maximum transmit power [W]	Number of users served	Location
Macro-cell	1 – 35	20 – 40	2000+	Outdoor
Micro-cell/Metro-cell	0.1 – 1	2 – 10	100 to 2000	Indoor/Outdoor
Pico-cell	0.05 – 0.1	0.2 – 2	30 to 100	Indoor/Outdoor
Femto-cell	0.01 – 0.02	0.02 – 0.1	1 to 20	Indoor

Usually macro- and micro-cells cover urban and rural areas due to the elevated coverage radius. Pico-cells are deployed in enterprises networks, while femto-cells are to be deployed in subscribers' homes.

When deploying tiered networks, the type of coverage of a mobile terminal, as in if it is covered only by one tier or by the two tiers of cells, the traffic characteristics of each cell, spectrum usage, backhaul and cost and energy efficiency are taken under consideration. Other than these considerations, a tiered cellular network must also comply with interference and mobility issues. In Figure 2.5, several deployment scenarios of Two-Tier Cellular Networks are represented, where two different frequencies are used for the primary (F1, in blue) and secondary (F2, in orange) node cells.

From Figure 2.5, one can identify indoor deployment scenarios with the surrounding box over the small cell, while being overlaid by the macro-cell's coverage radius. Pictured in Figure 2.5 is also sparse and dense small cell areas in both indoor and outdoor situations. Dense small cells areas can be deployed in areas with elevated traffic such as dense urban areas or large shopping malls and stadiums.

Other than small cells, Two-Tier Cellular Networks also supports the usage of relay nodes. Unlike small cells, RNs aim only to extend the coverage range of a given area, not increasing the overall network's capacity [Pere13]. By retransmitting signals, RNs can provide coverage beyond the cell edge in areas with difficult access, such as hilly areas, or overcome shadow zones, such like subways or tunnels.

Relays can operate in two different modes: Time-division Transmit and Receive (TTR) and Simultaneous Transmit and Receive (STR), [ACGB13]. In TTR, the transmission from the base station to the relay occurs in a different time frame than the transmission between the relay node and the user. This allows the usage of the same radio resources for the base station's DL and UL. In STR, the base station transmits to the relay node and to the user at the same time using different frequencies, with the DL in RN working in a similar fashion. The advantage of being able to send and receive at the same time comes with the drawback of an increased interference, creating the need to use interference cancellation schemes. 3GPP defined three layers for the classification of RNs [IwTN10]:

- **Layer 1:** Known as a repeater it is the simplest of the relays. It only amplifies the signal from the base station to the mobile terminal. It has the drawback of noise amplification.
- **Layer 2:** By demodulating and decoding the signals received from the base station, sending them to the mobile terminal encoded and modulated, this type of relay can eliminate the received noise. The drawbacks of this type of relay is the overall delay and added complexity.
- **Layer 3:** Improvement on Layer 2, with the addition of user-data regeneration processing. Again, the major drawback of this layer is the created delay and the added complexity.

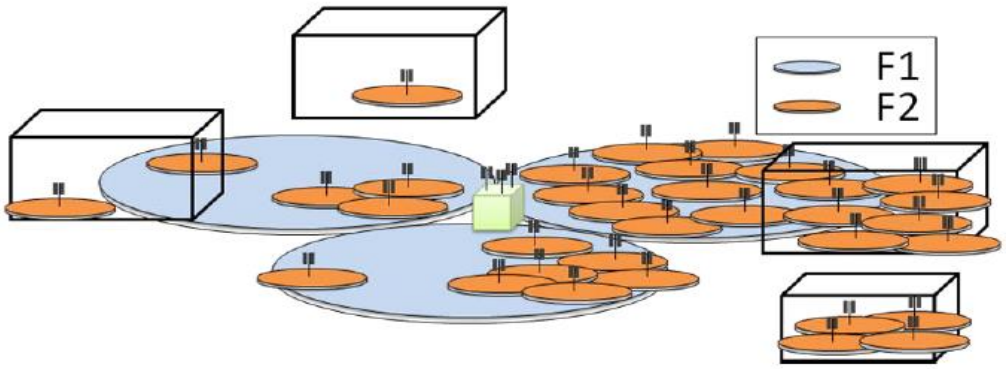

Figure 2.5 – Deployment Scenarios for Two-Tier Cellular Networks (extracted from [3GPP15a]).

2.3.2 Interference and Mobility

Two-Tier Cellular Networks provide a higher coverage and capacity to the surrounding users at the cost of an increased interference. In this type of networks, interference emerges not only from neighboring cells but also from the small cells overlaid in the macro-cell. Overall, one can define two types of interference with respect to the tiers the cells are deployed. The interference created among elements belonging to the same network tier is referred as co-tier interference. On the other hand, cross-tier interference, as the name suggests, is the interference created among network elements from different tiers. The created interference can severely limit the performance of a Two-Tier Cellular Network, thus the implementation of techniques for avoidance and mitigation of both types of interference are crucial for future deployments. Some techniques used for this effect are based on:

- **Cognitive Radio:** Technique used by the transceiver to detect the utilization of communication channels, allowing the usage of vacant ones and avoidance of occupied ones. Sensing and transmission, resource scheduling, and self-organized and self-optimized based on cognitive radio are some of the interference avoidance techniques.
- **Resource Allocation:** Management of the resources allocated for the primary node cells and secondary node cells to reduce cross- and co-tiers interference, while maximizing the throughput of each tier.
- **Power Control:** Transmit power control in the small cells tier both in UL, not to interfere with the macro-cell, and DL so that no interference is caused in macro- and small cells' users.
- **Q-learning:** Interference avoidance technique where small cells adapt their behavior, gradually learning by interacting with the surrounding environment, such as other interfering small cells.

- **Access Control:** Reducing the effects of interference by multiple access techniques.

The works of [SaHa16] presents in detail examples on each one of these techniques, doing a fair comparison among them.

The deployment growth of Two-Tier Cellular Networks not only leads to interference issues but also to mobility ones. Densification of small cell areas allied with the decrease of small cell sizes can lead to severe problems regarding Quality of Service (QoS). Mobility management emerges to solve the typical events that cause this break in QoS, such as handover failures, radio link failures and unnecessary handovers, also referred to as ping-pong events [SiBG15]. On the other hand, even if mobility is handled properly, by successfully completing a handover, there is an increasing load in the network due to how frequent handovers occur. In Figure 2.6, an example of the handover rate is presented for different velocities and between various cell types, over a network with 10 small cells per macro-cell randomly deployed with 50 m of the minimum inter site distance (ISD).

Depending on the velocity, there is a 120% to 140% increase of the handover rate from the macro to macro handover when compared to the macro to small cell handover. This leads to the increasing signaling load on the network.

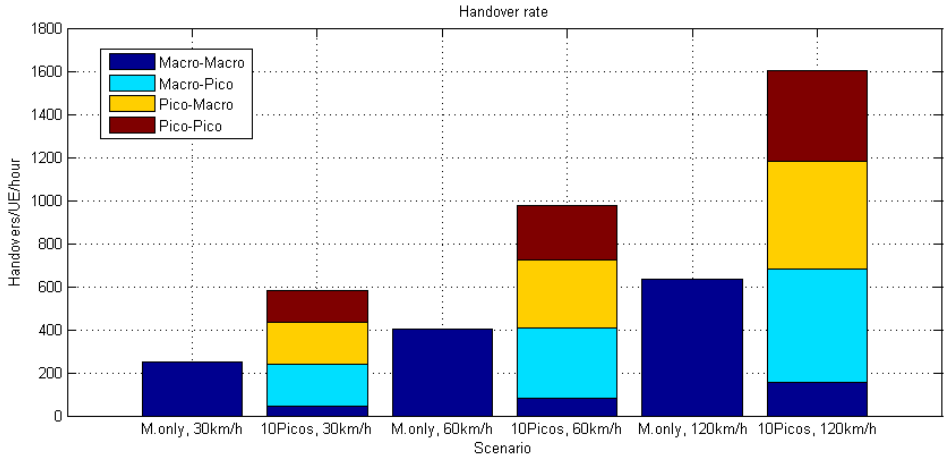

Figure 2.6 – Handover rate example for Two-Tier Cellular Networks (extracted from [3GPP13d]).

2.3.3 Backhaul

The densification of small cell areas introduces the need for a more efficient backhaul, such that network traffic can be dealt with in an appropriate way. The deployment of a backhaul network for Two-Tier Cellular Networks must overcome a set of challenges to provide a cost-effective solution while guaranteeing the QoS needed. The challenges reside mostly on the overall quality of the link, regarding coverage, capacity and synchronization, but also with the physical design and hardware architecture and at last the costs to assess the backhaul solution [JLSH15]. 3GPP's Release 13 considers an ideal backhaul as an optical fiber connection with high throughput (up to 10 Gbit/s) and reduced latency (less than 2.5 µs), and non-ideal such as DSL, cable, wireless and low throughput fiber accesses [3GPP15a], as represented in Table 2.5.

Table 2.5 – Small Cells backhaul categorization (adapted from [3GPP15a]).

Backhaul Type	Backhaul Technology Access	Latency [ms]	Throughput [Mbit/s]
Ideal	Optical Fiber	$< 2.5\times10^{-3}$	$> 10\times10^{3}$
Non-Ideal	Optical Fiber	10 – 30	$10 – 10\times10^{3}$
		5 – 10	100 – 1000
		2 – 5	$50 – 10\times10^{3}$
	DSL	15 – 60	10 – 100
	Cable	25 – 35	10 – 100
	Wireless	5 – 35	10 – 100

From Table 2.5, one can conclude that the optical fiber solution is the more reliable in terms of throughput (using PON over FTTH and FTTN infrastructures) while maintaining a reduced latency and a high range of deployment. However, to deploy such architectures, a huge investment from the operator is required, which can be also time consuming. Other wired solutions (e.g., DSL and cable), can be viewed as candidates for the backhaul architecture in terms of cost and easiness of deployment, but they present a high value of latency being also distance-limited. Wireless backhaul has the advantage of being more flexible regarding small cells locations at the cost of capacity unpredictability. Other disadvantages are the requirement of Line of Sight (LoS) in some frequency bands, e.g. microwave (6 to 56 GHz), V-band (57 to 66 GHz) and E-band (70 to 80 GHz), and the associated costs with licensing.

Other wireless backhaul solution for Two-Tier Cellular Networks is by making use of a Massive MIMO link between the primary and secondary nodes. By deploying a large number of antennas both in primary and secondary nodes, one can fully exploit the gains associated with Massive MIMO, whereas in a mobile terminal, given the space constraints, it is not possible to take advantage of the referred gains. This differs from one of the main trends currently under work in Massive MIMO, where the deployment focuses only on a great number of antennas located at the macro-cell node, to connect to the multiple mobile terminals in the cell.

2.4 Services and Applications

The main idea behind this framework is to improve the link performance between the primary and secondary nodes, given that the latter will be close to the mobile terminals. The deployment of multiple antennas at the transmitter and/or receiver improves the overall performance of a wireless system, in terms of spectral and energy efficiency [BoLe16]. Secondary nodes also present the advantage of being a well-behaved terminal, even when located in mobile infrastructures, for example, in public transportation. The reliability of the measurement results regarding the link between tiers in a Two-Tier Cellular Network, can be evaluated by considering traffic information and QoS of all services and applications provided by LTE-A.

There are 3 basic service components, audio, video, and data, and each component must comply with

the reference requirements in terms of delay and Bit Error Ratio (BER). The reference requirements vary per switching type employed by the network. For example, audio can be offered by both circuit switch, such as a phone call in GSM, and packet switch in VoLTE. For this service component, the reference requirements in circuit switch is in terms of BER and for packet switch is in terms of delay.

While services are mainly characterized by delay and BER, an application is usually characterized in terms of minimum bit rate, duration (e.g. phone call) in circuit switch, and data volume in packet switch. Applications can also be measured in a statistical way by the means of distributions for the duration of a phone call (Exponential Distribution) and the size of a file (Log-Normal Distribution), for example.

A service is composed of one or more service components, being grouped into classes according to their characteristics. In [3GPP15b], 4 main QoS classes are established for UMTS, also referred to as traffic classes: conversational, streaming, interactive, and background. Although there are no classes defined for LTE, the ones for UMTS can be used for 4G. The main distinguishing factor among the 4 classes is in terms of delay sensitivity, their fundamental characteristics being represented in Table 2.6, while Table 2.7 shows the ones for LTE.

Table 2.6 – QoS Classes (extracted from [Corr16]).

Service Class	Conversational	Streaming	Interactive	Background
Real Time	Yes	Yes	No	No
Symmetric	Yes	No	No	No
Switching	CS	CS	PS	PS
Guaranteed Rate	Yes	Yes	No	No
Delay	Minimum Fixed	Minimum Variable	Moderate Variable	High Variable
Buffer	No	Yes	Yes	Yes
Bursty	No	No	Yes	Yes
Example	Voice	Video Streaming	Web Browsing	E-mails

Table 2.7 – Standardized priority classes characteristics (extracted from [3GPP16f]).

QCI	**Resource Type**	**Priority Level**	**PDB (ms)**	**PER**	**Example Services**
1	GBR	2	100	10^{-2}	Conversational Voice
2		4	150	10^{-3}	Conversational Video (Live Streaming)
3		3	50	10^{-3}	Real Time Gaming, V2X messages
4		5	300	10^{-6}	Non-Conversational Video (Buffered Streaming)
65		0.7	75	10^{-2}	Mission Critical user plane Push to Talk voice
66		2	100	10^{-2}	Non-Mission-Critical user plane Push to Talk voice
75		2.5	50	10^{-2}	V2X messages
5	Non-GBR	1	100	10^{-6}	IMS Signaling
6		6	300	10^{-6}	Video (Buffered Streaming), TCP-based (e.g., www, e-mail, chat, ftp, p2p, progressive video, etc.)
7		7	100	10^{-3}	Voice, Video (Live Streaming), Interactive Gaming
8		8	300	10^{-6}	Video (Buffered Streaming), TCP-based (e.g., www, e-mail, chat, ftp, p2p, progressive video, etc.)
9		9			
69		0.5	60	10^{-6}	Mission Critical delay sensitive signaling
70		5.5	200	10^{-6}	Mission Critical Data
79		6.5	50	10^{-2}	V2X messages

LTE and LTE-A also define several priority classes for the different services, in terms of Guaranteed Bit Rate (GBR) being identified by a Quality Channel Indicator (QCI) index. The QCI identifies the attributes of Priority Level, Packet Delay Budget (PDB) and Packet Error Loss Ratio (PER). These priority classes are already standardized, which helps to ensure the overall QoS by the operator deploying the 4G network. In Table 2.7, one can see the standardized priority classes for LTE and LTE-A.

2.5 State of the Art

In this section, the state of the art regarding Massive MIMO deployments considering multiple antennas at both transmitter and receiver is presented. These types of links can be applied in a Two-Tier Cellular Network for backhaul and antenna offloading, to achieve a more balanced network.

The work of [HHBD13] proposes a TDD based network architecture where a Massive MIMO base station is overlaid with a dense tier of small cells. This TDD-based Two-Tier Cellular Network architecture incorporates the advantages of massive MIMO with the overall capacity and coverage enhancement and higher traffic support, characteristic of small cells. The TDD channel reciprocity not only enables the base station to accommodate a large number of antennas without prohibitive channel estimation overhead, but also allows to estimate the interfering subspace from its received UL signal.

This knowledge can be used to design DL precoders that reduce the interference to the small cell tier. The authors compare two duplexing schemes, TDD and Reverse-TDD, the former reversing the order of DL and UL periods in one of the tiers. Simulation results indicate that the proposed scheme can significantly minimize the aggregate cross-tier interference experienced by small cells at the price of a negligible macro-cell performance loss. Future work proposes an evaluation of the performance gains in a more realistic multi-cell setting where also the small cells are equipped with multiple antennas, employing a similar precoding scheme to cancel cross- and co-tier interferences and the inclusion of power control and interference reduction techniques for an increased performance.

In [BoLe16], an overview on the 5G integration of Massive MIMO and mmWave technologies is presented, concerning the overall benefits and challenges to overcome. Three case studies are elaborated regarding the implementation of a Two-Tier Cellular Network employing both technologies.

The first case study makes a comparison between digital beamforming and hybrid beamforming. The results obtained reveal that a hybrid beamforming achieves almost the same performance than a digital one, in terms of sum rate. This leads to reducing the number of RF chains, ADC and DAC needed when compared to the number of antennas used. The second case study investigates the usage of a mobile relay employing a large-scale antenna array.

The first scenario evaluated is without a mobile relay, using multiuser block diagonalization beamforming. The second scenario, the macro-cell employs singular value decomposition beamforming, with increasing number of antennas elements. The communication between UEs and the mobile relay is done with a mmWave frequency band link. The results obtained in terms of the total sum

rate for different SNRs and M antennas at the mobile relay, are presented in Figure 2.7, for the simulation parameters summarized in Table 2.8.

From Figure 2.7, one can see that the total sum rate in the scenario with the mobile relay is much higher than in the scenario without it. One can also see that by increasing the number of antennas at the mobile relay, the total sum-rate increases as well, proving the increased performance when considering a large-scale antenna system such as Massive MIMO.

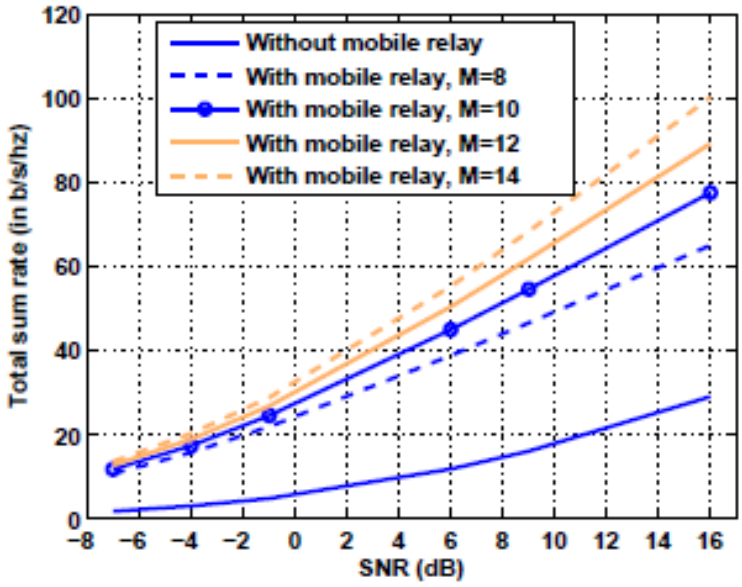

Figure 2.7 – Comparison of the sum rates achieved with and without mobile relay (extracted from [BoLe16]).

Table 2.8 – Simulation Parameters (extracted from [BoLe16]).

.

Distance between macro-cell and relay	1 km
Number of antennas at each UE	2
Macro BS transmitter power	5 W
Radius of the cell	1.6 km
Reference distance d_0	1.6 km
Path loss exponent	3.8
Mean path loss at d_0	134 dB
Channel bandwidth	5 MHz
Carrier frequency	1.8 GHz
Receiver noise figure	5 dB
Receiver vertical antenna gain	10.3 dBi
Receiver temperature	300 ^{o}K

Regarding the second case study outlined in [BoLe16], [KhJa15] analyze the coverage probability performance of a moving relay node in a Two-Tier Cellular Network. The authors consider three scenarios, evaluating the coverage probability performance parameters for a UE within a macro-cell and within a train depending on the scenario. The first scenario considers that there is no moving relay node present in the network, while the other two scenarios evaluate the performance within a train, where the

signal is received from the relay node, and outside the train within the macro-cell where the signal is received cooperatively from the BS and relay node. The results for the three scenarios in terms of SNR values are considered for different Vehicle Penetration Losses (VPL) in the first scenario, and for different signal-to-interference ratio values in the second and third scenarios.

The main conclusions one can see is that for the train user, the coverage probability assumes higher values when considering the existence of a mobile relay node, even with negative values of signal-to-interference ratio. This is mostly due to the mitigation of VPL in the second scenario. As for the third scenario, the results confirm that with cooperative communication, the overall network coverage probability is higher. One application for this scenario is for moving trains at the boundaries of a given cell, which can significantly improve the coverage probability for the UEs located in these areas.

The authors in [YKSM15] propose a novel moving cell to provide an adequate resource management and overcome the challenges emerged from group mobility, namely, where many UEs share the same moving platform such as public transportation. The proposed solution is thus an evolution of a mobile relay node deployed on the moving platform. Applying Massive MIMO for backhaul connection and LTE-A Rel.10 relay architecture for the baseline of the moving cell the performance of the backhaul capacity was studied in terms of horizontal and vertical distances from the base station. The deployment and results obtained for the backhaul capacity are presented in Figure 2.8, for the simulation parameters in The system's capacity was measured in terms of time, for a distance between ground antennas of 200 m, and between base stations of 1993 m. The acceleration/deceleration was of ±3km/h/s, for the sampling rate 512 ms considering 1 antenna per 1 train set. To analyze the control signal traffic, it was simulated for a cell radius of 1 km with 6 sectors, with 228 UEs and train's velocity of 228 km/h. The sampling interval was also of 512 ms, and the train had 18 doors per set.

It was shown that the system's capacity is significantly increased compared to the conventional macro-cell approach, even though it varies periodically. The total number of control signal overheads is also reduced in the moving cell, compared to the macro-cell, improving user Quality of Experience (QoE).

Table 2.9.

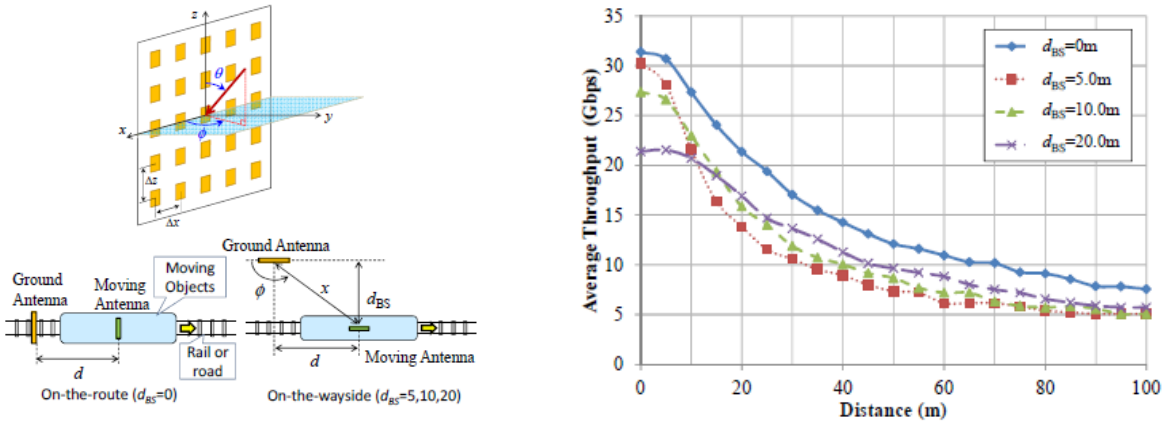

(a) Used antenna and deployment scenario.

(b) Link Throughput.

Figure 2.8 – Backhaul capacity scenario and results (extracted from [YKSM15]).

The system's capacity was measured in terms of time, for a distance between ground antennas of 200 m, and between base stations of 1993 m. The acceleration/deceleration was of ±3km/h/s, for the sampling rate 512 ms considering 1 antenna per 1 train set. To analyze the control signal traffic, it was simulated for a cell radius of 1 km with 6 sectors, with 228 UEs and train's velocity of 228 km/h. The sampling interval was also of 512 ms, and the train had 18 doors per set.

It was shown that the system's capacity is significantly increased compared to the conventional macro-cell approach, even though it varies periodically. The total number of control signal overheads is also reduced in the moving cell, compared to the macro-cell, improving user Quality of Experience (QoE).

Table 2.9 – Simulation Parameters (extracted from [YKSM15]).

Transmission Scheme	MIMO-OFDM specific mode
Carrier Frequency	20 GHz
Bandwidth	400 MHz
Antenna Elements	Tx: 256 Rx: 64
Number of Tx streams	8, 16
Modulation	QPSK, 16QAM, 64QAM
Power angle spectrum distribution	Azimuth: Gaussian; Zenith: Laplacian
Radiation/arrival angle	On the route: 90º; On the wayside: variable
Angular spread	Tx: 5º Rx: 20º
Fading channel	Nakagami-Rice with 10dB rice coefficient; 16 paths

Chapter 3

Framework Specification and Performance Models

In this chapter the framework and performance parameters for the model being implemented are specified. The chapter begins by providing an overview of the several modules to be implemented in the model, regarding secondary node configuration, signal processing and the proposed LTE-A application performance parameters. It ends with the algorithms applied in the implementation and its assessment.

3.1 Model Overview

The model can be defined in two layers, the secondary node layer and the primary one as presented in Figure 3.1. In the first mentioned layer, the secondary node has measurement related input parameters concerning the number of antennas and diversity type, its surrounding environment for its deployment site and its behavior according to mobility. From these input parameters, the secondary node collects LTE signals data from known base stations, performing its demodulation and determining the CQI index to report to the primary node based on the measured SINR. The reported CQI indices are from both the proposed scheme and the expected one, considering respectively an independent and common Resource Block Modulation Coding Scheme. From the several captures, the primary node layer will perform the action of link adaptation and scheduling which in turn will provide the performance parameters taken for analysis.

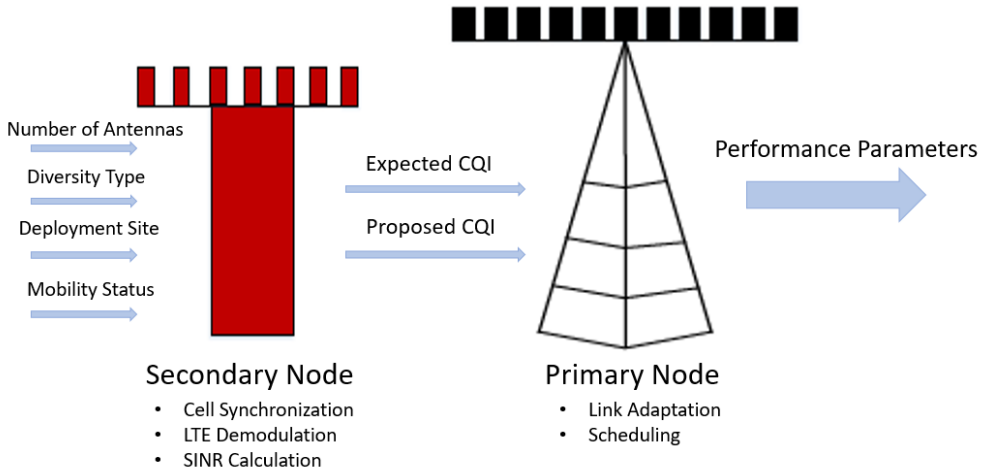

Figure 3.1 – Model Structure (adapted from [RaSo16]).

The other operation performed at the primary node is scheduling, where the performance of both schemes is compared, considering a scheduler based on the resource block and on the sub-band levels.

Scheduling is performed based on CQI reporting, where an eNB receives several indices from multiple users with different channel conditions. After the UE/secondary node complete CQI reporting, the eNB must perform scheduling for the different users during a TTI of 1 ms, or one subframe. The radio interface of LTE and LTE-A allows resource allocation to happen both in time and frequency, thus enabling to perform frequency selective scheduling by leveraging the channel's time and frequency selectivity to allocate valuable radio resources in an optimal manner [ALHD14].

The complexity of a scheduler considering RB-dependent adaptive modulation has proven to be too complex and adding a signaling overhead that would degrade the overall scheduler performance and QoS for the different users [NFMN06]. With the proposed scheme, the signaling overhead is expected to be reduced, since the channel conditions are expected not to suffer significant fluctuations along time.

The same MCS can be used during multiple slots, considering the first slot MCS, being that the CQI reporting could be triggered when a sudden change on channel conditions occur, following the scheduling algorithm. To prove the efficiency of the proposed scheme, three scheduling algorithms are considered, each aiming to optimize the different metrics explained above: Round Robin to optimize complexity and fairness, Best CQI to optimize the cell's capacity and Proportional Fair to optimize fairness among users.

3.2 Secondary Node Receiver Development

3.2.1 MegaBEE Overview and Configuration

The first module to be implemented in the secondary node is its data acquisition system. The equipment used to collect data is the FPGA-based Software Defined Radio platform MegaBEE [BEEc16a]. MegaBEE comprises two subsystem units for the left and right sides of this platform being that each subsystem unit is composed of one baseboard and two RF frontend boards. The baseboard has as its main component an all programmable System on Chip Zynq device (Z7100) from Xilinx containing a dual ARM Cortex-A9 processor as its processing system (PS) and as programmable logic (PL) a fabric which is equivalent to a Kintex-7 FPGA. The overall functional diagram can be seen in Figure 3.2.

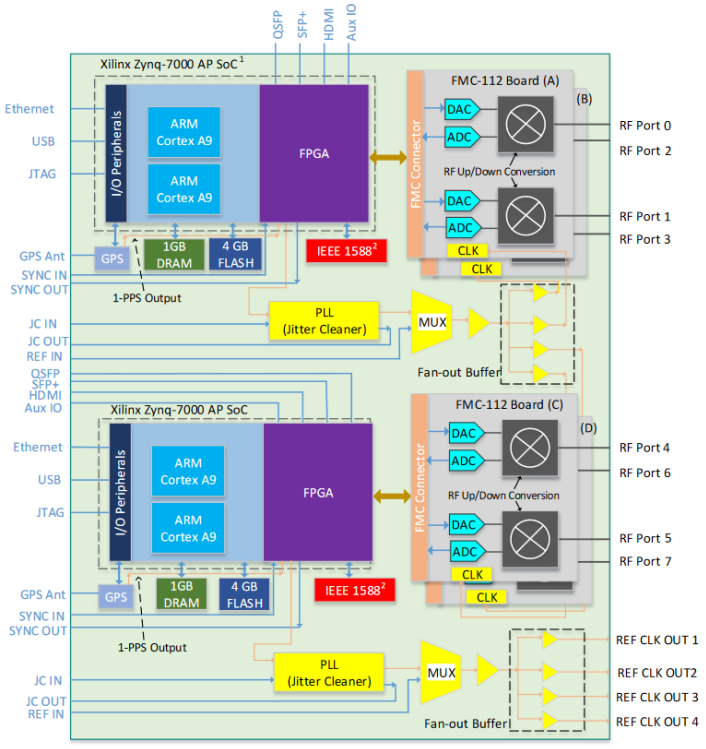

Figure 3.2 – Functional diagram of MegaBEE (extracted from [BEEc17a]).

Other peripherals can also be found on this platform, such as DDR3 DRAM, 10 Gbit (SFP+, QSFP and Ethernet) interfaces as well as an accelerometer, pressure sensor, GPS and a clock recovery circuit.

Regarding the RF frontend boards, the FMC-112 Board is used for the up- and down-conversions of the RF signals both in DL and UL. This conversion is undertaken by the Agile transceiver chip AD9361 [AD17], along with external power amplifiers and optimized filters for a set of LTE frequency bands. Each side of the MegaBEE contains two FMC-112 boards which in turn supports two RF ports. This means that one single MegaBEE platform can support up to 8 antennas in a synchronized fashion given that the FMC-112 board includes clock references and synchronization inputs/outputs that can be used to synchronize all the RF frontend boards in a single MegaBEE or even multiple stacked MegaBEE platforms that can be scaled up to 256x256 MIMO applications.

MegaBEE runs a streamlined Linux operating system, allowing a remote connection from another machine to configure the RF frontend board and loading the bit file for the FPGA, using the included firmware [BEEc16b] to control these components. There are three main parts for configuring the device, being that all can be done using a shell script. The first part for setting up the device consists of programming the FPGA, by loading the bit file generated using designed models, Figure 3.3, with software BEEcube Platform Studio (BPS) [BEEc17a]. This platform runs on top of the Mathworks Simulink framework, providing an automatic generation of all platform specific hardware interfaces and corresponding software drivers. This allows the developer to focus on the algorithms and functionalities of his application rather than knowing the specific hardware low level implementation details. When the design is completed, BPS generates a .fpga file which, in turn, will be programmed in the MegaBEE using the appropriate firmware command.

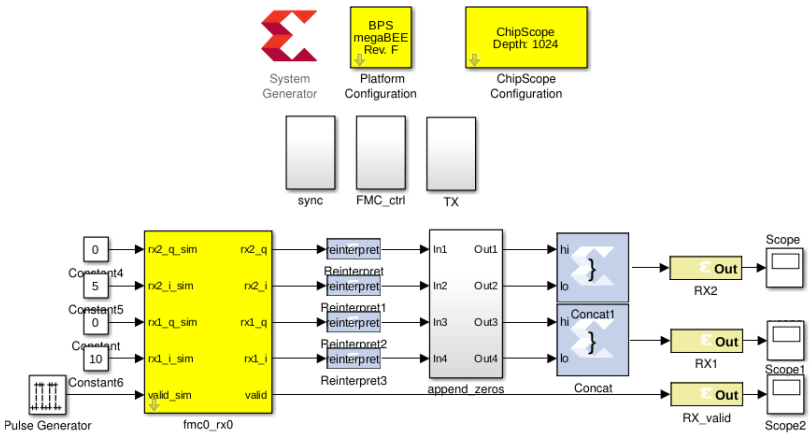

Figure 3.3 – Design Model Blocks.

From Figure 3.3, three different types of blocks can be identified. The blocks colored in blueish grey and golden correspond to the Vivado System Generator for DSP [Xili15], which can be used to perform several functions, from logical operations to digital filtering. The yellow colored blocks refer to the blocks provided by BEEcube, each one being an interface for the existing components that compose MegaBEE. Lastly, the white colored blocks are common Simulink blocks, which can either represent a subsystem, such as the “append_zeros” seen in Figure 3.3, or to generate waveforms for simulation.

Only BEEcube blocks and Vivado System Generator for DSP blocks are used for generating the bitfile used to program the FPGA, but for debugging and simulation one can use Simulink blocks attached to the Gateway golden blocks illustrated in Figure 3.3, where System Generator fixed-point data type is

converted to Simulink Double. When generating the bit-file to program the FPGA these blocks must be removed from the designed model. After the bit-file is programmed onto the FPGA, a ChipScope probes with a variable depth configured by the “ChipScope Configuration” block may be used to visualize any given outputs one wants to analyze, using Vivado Waveviewer Tool software with a JTAG connection between the MegaBEE and a host computer.

The main components used to control the FPGA model using firmware are Software Registers (SR) as seen in Figure 3.4 the blocks name “txnrx”, “enable”, “enagc”, “ctrl_w” and “ctrl_r”. An SR enables the access for writing and reading of a 32-bit register in both hardware and software allowing its usage for multiple functionalities such as switching, controlling internal circuits inside the FPGA design model and also for storing.

An example of this functionality can be seen in Figure 3.4 for the “FMC_ctrl” subsystem. This subsystem makes use of a FMC112 Control block which provides a direct interface to pins of the same name on the AD9361 RF Transceiver. The four aforementioned SRs control the inputs of this block, namely to setup the transmission and reception mode (“txnrx”), selecting the state machine state (“enable”) and automatic gain control (“enagc”) and finally as control inputs and outputs for the base-band processors.

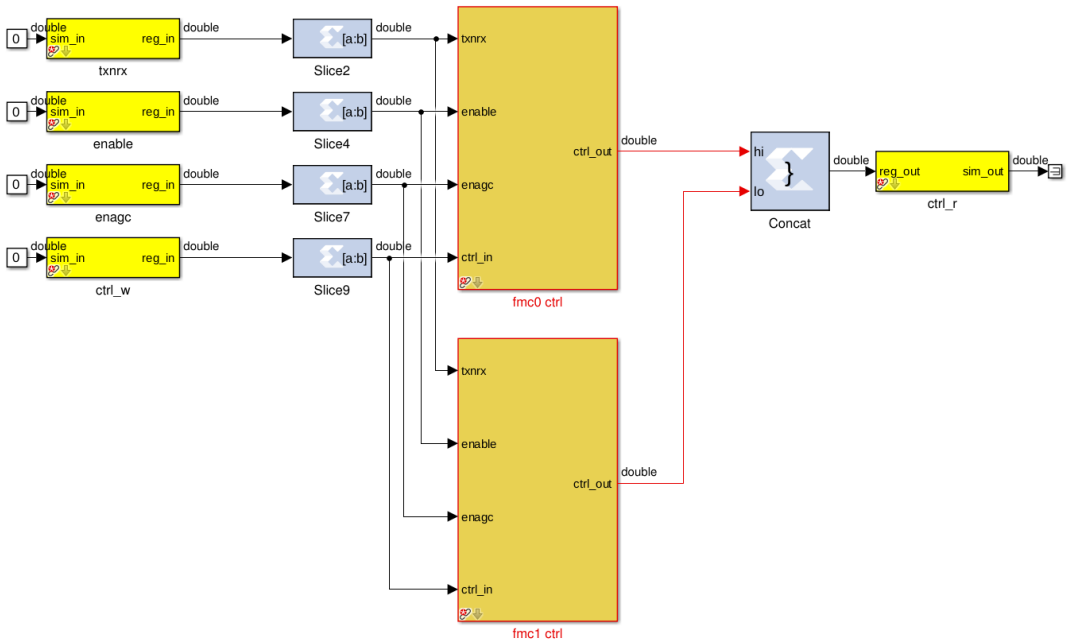

Figure 3.4 – "FMC_ctrl" subsystem.

The second part of the MegaBEE setup is to configure the reference clock source for the FMC112 RF boards. The MegaBEE FMC112 board already contains an output of a reference clock signal, ranging from 19.2 MHz to 40 MHz which can be directly connected to the reference clock input of the baseboard via a SMA cable. Other reference clocks are used for the jitter cleaning and synchronization between multiple subsystems.

After the FPGA is programmed, and the reference clock is set, the FMC112 board needs to be configured, regarding the parameters used for the transceivers. The configuration is done using a configuration file which sets the parameters such as the sampling frequency for the ADC and DAC

conversion, the TX/RX frequency and bandwidth and the TX attenuation. For the purposes of the application, received data from the RF frontend needs to be transferred to the host PC in a continuous way for further offline processing.

3.2.2 Data Acquisition Methods Description and Comparison

Three methods are used to transfer received data from the MegaBEE to a host computer. The methods are from now referred as Block RAM (BRAM) Method, Direct Memory Access (DMA) Method and 10 GbE (XGE) Method with each method name referring to a main BPS block.

The BRAM method, Figure 3.5, consists of storing the RF signals from each port to a set of Shared Block RAMs. Each BPS BRAM block can store a maximum of 2^{15} samples, being an implementation of 32 Xilinx Shared BRAMs. Due to the hardware constraints, there is a limited number of BRAM blocks from BPS that can be used, decreasing the total number of samples that can be obtained using this method. The process would be triggered by writing a Software Register, which in turn would reset a master counter of 32 bits which would fill each address of the BRAMs with a snapshot of the captured RF received data.

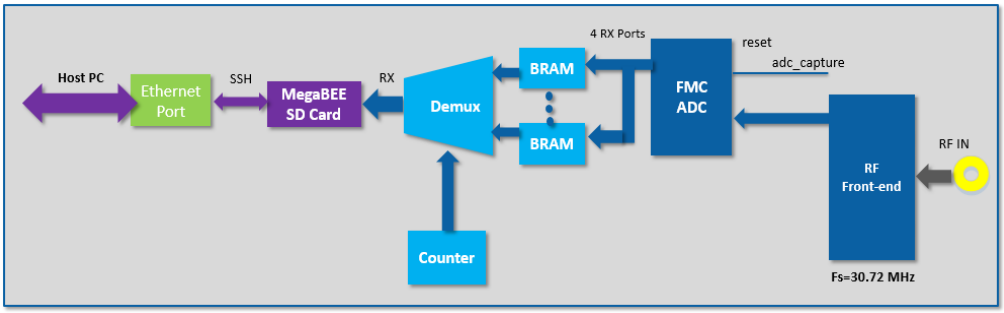

Figure 3.5 – BRAM Functional Diagram (adapted from [NI17b]).

One can then store the captured data from the multiple BRAMs considering individual files for the different BRAMs with a 32-bit unsigned binary format.

The DMA method, Figure 3.6, makes use of a Direct Memory Access to transfer large amounts of data from the programmable logic to the processing system of the chipset. The major benefit of this solution is that it frees both the PS and PL resources to do other type of functions during the transfer of big arrays of data, making it extremely fast, in an automatically synchronized way. A DMA transfer is based on two asynchronous First-In First-Out (FIFO) buffers, one for the PS and the other for the PL. The data is then stored in the DDR3 DRAM, which can be accessed by software in the PS and hardware in PL. Control of this transfer is triggered by software, by writing a software register, being that each transfer contains an unsigned 64-bit word that contains data from one RF board.

Following the AXI-4Stream protocol [ARM10], a DMA transfer occurs when the transferred data and the FIFO is ready to be written, by asserting two hardware flags, TREADY and TVALID, at the same time, given that the boundary of the transferred data needs to be known in order to indicate the last beat of the transfer to the PS, by asserting an additional hardware flag, TLAST.

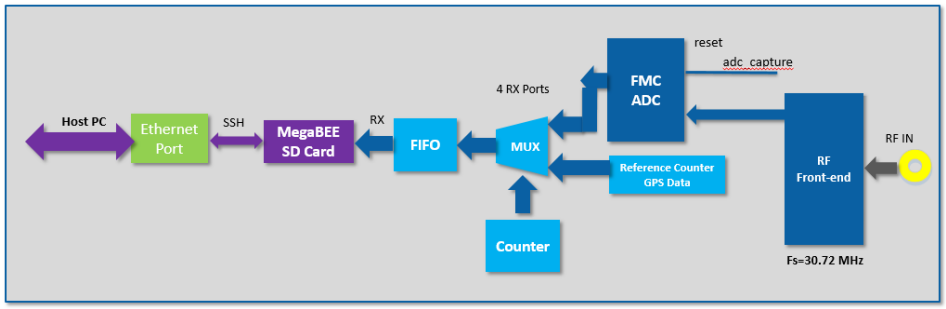

Figure 3.6 – DMA Functional Diagram (adapted from [NI17b]).

When the FPGA is programmed, a C program can be used to read the contents of a device file that will contain the written elements of the FIFO, and print it in another text file for further analysis. The format for the data stored in the text file is 64 bit unsigned binary, being that the first two 64-bit words pertain to a reference counter and GPS coordinates obtained by a serial connection using the GPS module installed in the MegaBEE. The overall format for the stored data can be seen in Figure 3.7.

64 bits

Reference Counter			
Latitude Int.	Latitude Frac.	Longitude Int.	Longitude Frac.
RX1 Q	RX1 I	RX0 Q	RX0 I
RX3 Q	RX3 I	RX2 Q	RX2 I
RX1 Q	RX1 I	RX0 Q	RX0 I
RX3 Q	RX3 I	RX2 Q	RX2 I
RX1 Q	RX1 I	RX0 Q	RX0 I
RX3 Q	RX3 I	RX2 Q	RX2 I
⋮	⋮	⋮	⋮

Figure 3.7 – DMA Method received data format.

The DMA method can only transfer 64-bit words at a time, which creates the need for a multiplexing engine to receive data from the RF ports, GPS coordinates and the reference counter.

The last used method to acquire data in a continuous way consists of transmitting a stream of RF data from all the ports over a 10 GbE (XGE) connection between a host processor and the SFP+ outputs in the MegaBEE [NI17a]. From the MegaBEE side, the stream of data consists of a UDP packetization of two RF ports from the FMC-112 board with a variable payload length.

As the UDP packets only allowed the storing of two RF ports per side of the MegaBEE, an extra connection had to be established to take advantage of all the RF ports available per side of the MegaBEE. As seen in the functional diagram presented in Figure 3.8, the block colored in purple refers to the 10 GbE block, an interface between the 10 GbE physical ports and BPS whose input is the packetized RF data achieved with a BPS UDP TX Streaming block.

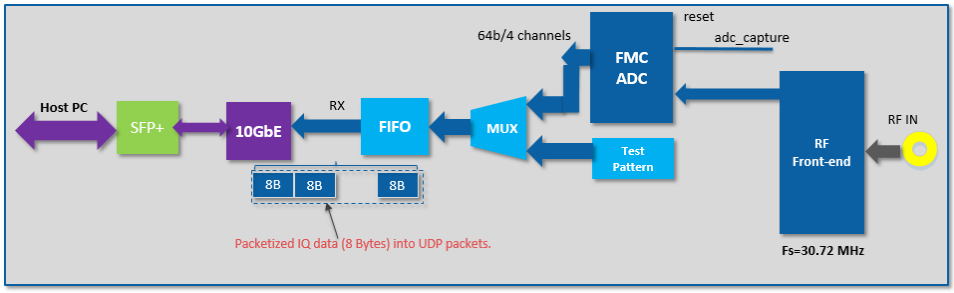

Figure 3.8 – XGE Functional diagram (adapted from [NI17b]).

The received RF data from the FMC112 board is transferred to a UDP TX block, following a protocol based on the protocol employed by the DMA FIFO method, AXI4-Stream [ARM10], during a sampling clock period (8 Bytes per sample). During each sample period, the MegaBEE can stream the IQ data on 2 RF ports to the host or up to 4 RF ports when considering multiple SFP+ usage. As the number of XGE connections increase, the CPU usage on the host side increases as well, creating the need for reducing the number of established connections.

On the host side, the IQ samples are extracted from the received UDP packets over a UDP socket binding to the interface's address of its XGE network card and to the port used to establish the socket connection. A software register "adc_capture" is used as a switch to trigger the streaming procedure, being that the streamed data is going to be collected and stored via 8 parallel socket connections to acquire the RF data from the 16 available ports.

The payload size of UDP streaming is configurable, thus when this value is set to a larger size a high throughput can be achieved. The generated UDP packets are then streamed over the 10 GbE connection with the format presented in Figure 3.9.

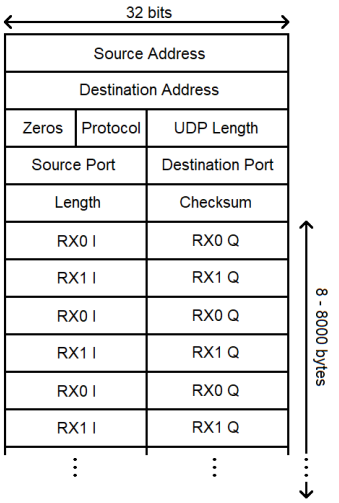

Figure 3.9 – UDP Packet Format.

To facilitate the processing analysis, the data is stored in different files, containing information of 20 ms LTE signals, allowing the capture of a maximum of two complete LTE frames, comprising a total of 614400 samples per capture. The main difference between the XGE method and the BRAM and DMA methods in what concerns multiple captures is the lack of gaps between captures, thus creating a

continuous stream of captured data where one can decide the number of samples to capture according to the application. For testing purposes such as the reading process after the data is stored, continuous data transmission and packet loss control, a test pattern data that mimics the output of the two RF ports is implemented.

As UDP is a connectionless protocol, there is no flow control which leads to possible packet losses, meaning that the main disadvantage of this method in what concerns continuous acquisition of data. The packet losses bottleneck is dependent on the host performance to handle all the connections it has established. To control when the packet losses occur a frame header, Figure 3.10, is appended to the payload data, where one of its contents is a counter that is used to track the gaps between received packets when there is packet loss. Packet retransmission however is a difficult task to implement for the type of stream it is being dealt with. As BPS has only available blocks for UDP based XGE connections, it was not possible to implement a TCP based connection for flow control. The contents of the frame header are controlled by two Software Registers in terms of length and its pattern while the frame length is configured by another Software Register being within 640 to 8000 bytes. The frame header contains as its elements a given pattern to detect the beginning of a UDP packet (BEE4BEE4 in Figure 3.10) and a counter to detect gaps between packets thus indicating whether there were any lost packets or not.

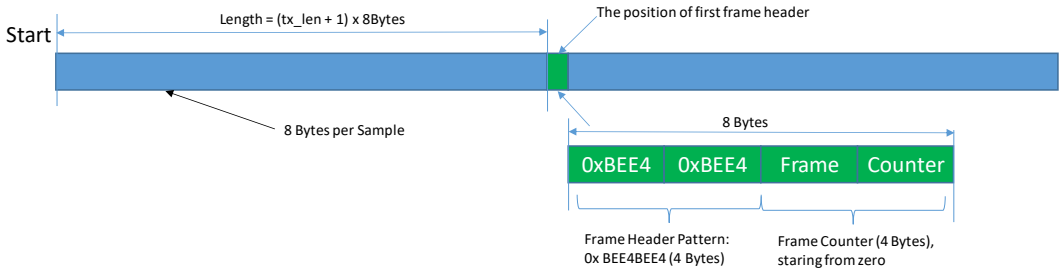

Figure 3.10 – Frame Structure (extracted from [BEEc17b]).

The metrics used to compare each method are the following:

- Number of antennas: For all the considered methods, the maximum number of 8 antennas per MegaBEE, 4 for each side can be used. However, for the non-continuous capture methods such as the BRAM and DMA method, the number of captured samples can be limited;
- Number of captured samples: The performance of this metric is dependent on the number of antennas used when considering non-continuous capture methods.
- Delay between captures: To mimic a continuous acquisition, this delay should be close to zero, however by making use of a reference counter, the delay between captures can be obtained;
- Existence of gaps within the capture: Dropped samples during the acquisition procedure can lose necessary information for the analysis of the captured signal.

For a sampling frequency of 30.72 Msamples/s, the metrics impact can be seen in Table 3.1. The first method, BRAM, has a severe limitation in terms of number of samples for each capture when considering the full usage of all the possible antennas. This method does not allow the capture of a complete LTE frame in a single capture, and the delay in the order of seconds between captures led to this solution to be discarded.

The second solution based on DMA, has a better performance than the BRAM method, allowing one to capture about one and a half LTE frame per capture. The bottleneck of this solution is thus the delay between captures which is in the order of milliseconds, being an improvement of the previous method, although for data storing it still has a delay of seconds.

The final method, based on the UDP streaming over a 10 GbE connection, has as its main advantages the possibility of a continuous acquisition of data and unlimited number of samples. However, the bottleneck of this solution, created by the dropped UDP packets severely limits the processing of the captured data. As the dropped packets are dependent on the host processor performance, the rate randomly varies and thus this solution was not considered as it needs improvements to optimize the packet loss rate.

Table 3.1 – Capture methods metrics performance.

Method	BRAM	DMA	XGE
Number of antennas	4	4	4
Number of captured samples	~100 000	~500 000	Unlimited
Delay between captures	Order of seconds	Order of milliseconds	Continuous
Gaps within the capture	Non-existent/Not identified	Non-existent/Not identified	Dependent on host performance

3.2.3 LTE Downlink Channel Characterization

After collecting data, the secondary node performs the channel characterization of the received LTE signals. LTE Downlink transmission as referred earlier in this document employs Orthogonal Frequency-Division Multiplexing. This transmission scheme allows a resource allocation both in time and frequency to multiple users, allowing a distributed resource scheduling. A OFDM modulator allows for a low-complexity implementation computation-wise by Fast Fourier Transform (FFT) processing [DaPS14], instead of applying a bank of modulators/correlators. A time-discrete signal model for OFDM transmission assumes as the sampling frequency f_s a multiple value *N* of the subcarrier spacing Δf of 15 kHz. A transmitter model procedure is thus as follows, the modulated symbols are converted from serial to parallel being applied an Inverse Discrete Fourier Transform (IDFT) followed by the appendage of the cyclic prefix and a parallel to serial conversion before being converted from analog to digital.

On the receiver side, the inverse operations executed in the transmitter are performed in order to retrieve the transmitted OFDM symbols. As a Resource Block comprises 7 OFDM symbols and 12 Subcarriers, for the bandwidths considered in the LTE standard one can define all the parameters for modulation and demodulation in terms of the sampling frequency and FFT/IFFT size of a LTE radio channel in Table 3.2 (not considering carrier aggregation).

Table 3.2 – LTE parameters.

Channel bandwidth [MHz]	1.4	3	5	10	15	20
N_{RB}^{DL}	6	15	25	50	75	100
N_{sc}^{DL}	72	180	300	600	900	1200
IFFT/FFT size	128	256	512	1024	1536	2048
f_s **[Msamples/s]**	1.92	3.84	7.68	15.36	23.04	30.72
Samples per slot	960	1920	3840	7680	11520	15360

The received discrete-time signal over a multipath propagation channel [MEJX09] can be modelled as a simple OFDM stream affected by Additive White Gaussian Noise (AWGN), however the channel is not only affected by channel impulse response and noise but also from the offset between the carrier frequency set by the local oscillators at the transmitter and receiver. This offset can be estimated and corrected by taking advantage of the redundant properties of a cyclic prefix appended at the beginning of every LTE subframe within a frame.

The procedure prior to the demodulation of a LTE signal aims to the estimation of the carrier frequency offset value and also to obtain synchronization by acquiring the information on the connected cell regarding its cell identifier, cyclic prefix length and duplexing mode in order to determine the offset between the beginning of the captured data and the start of a LTE frame. After this procedure is finished the full demodulation can be performed by retrieving the number of cell-specific reference signal ports and bandwidth in terms of number of resource blocks.

For LTE, two signals are defined for synchronization, the Primary Synchronization Signal (PSS) and Secondary Synchronization Signal (SSS). These signals belong to a series of resource elements mapped onto the physical layer but containing no information from higher layers, thus defining the synchronization signals and reference signals. The two signals PSS and SSS enable subframe synchronization and frame synchronization respectively and also to obtain the physical cell identity, N_{ID}^{CELL}, as defined as:

$$N_{ID}^{CELL} = 3N_{ID}^{(1)} + N_{ID}^{(2)}. \tag{3.1}$$

where:

- $N_{ID}^{(1)}$: physical layer cell identity group (ranging from 0 to 167) obtained by demodulating the SSS;
- $N_{ID}^{(2)}$: sector identity within the group (ranging from 0 to 2) obtained by demodulating the PSS.

There are thus 504 unique physical cell identities. Before the synchronization procedure, there is an additional step to acquire time and frequency synchronization, namely the timing for the beginning of a OFDM symbol, and the Carrier Frequency Offset (CFO).

In [MEJX09], a Maximum Likelihood estimation of the symbol timing and fractional frequency offset is performed exploring the redundant properties of the cyclic prefix obtaining a rough slot and symbol synchronization. After obtaining slot synchronization, one can remove all the cyclic prefixes from the received LTE frame and perform the next step of synchronization by detecting the PSS with a cross-correlation between the received signal and a generated reference sequence.

The PSS is generated based on a Zadoff-Chu sequence. A Zadoff-Chu sequence is known as a constant amplitude zero autocorrelation (CAZAC) waveform and it is used for synchronization due to their high auto-correlation property. From [3GPP17a], the PSS is 62-lenght sequence generated with a root index *u* according to:

$$d_u(n) = \begin{cases} e^{-j\frac{\pi un(n+1)}{63}}, & n = 0,1,...,30 \\ e^{-j\frac{\pi un(n+1)(n+2)}{63}}, & n = 31,32,...,61 \end{cases} \tag{3.2}$$

The PSS is mapped onto the 31 subcarriers on each side of the DC subcarrier, using six resource blocks with five reserved subcarriers each side. For a FDD frame, the PSS is mapped in the last OFDM symbol of the first slot in the first and fifth subframe, while in a TDD frame it is mapped in the third OFDM symbol in the first and sixth subframes. Three sequences are generated with different indexes *u*, each being associated with a given sector ID, $N_{ID}^{(2)}$ as defined in Table 3.3:

Table 3.3 – Root indexes for PSS (extracted from [3GPP17a]).

$N_{ID}^{(2)}$	**Root index *u***
0	25
1	29
2	34

The PSS is used to obtain subframe synchronization, as the sequence mapped into the different subframes is the same, thus not enabling to differentiate between the two subframes. A cross-correlation between the received signal and the three sequences is performed to determine which sector ID the cell belongs to. Given the good auto-correlation properties, one expects a greater magnitude at the output of the cross-correlator for the correct sequence being correlated. As referred, the PSS only gives subframe synchronization because it is mapped equally in the two subframes for both TDD and FDD duplexing modes. To obtain frame synchronization and the physical cell identity the next step is to demodulate the SSS.

Similar to the PSS, the SSS is a 62-length sequence but generated by an interleaved concatenation of two 31-length binary sequences, with the concatenated sequence being scrambled with a scrambling sequence given by the PSS. The generation of this sequence differs for the two subframes it is mapped to, the same as the PSS, however one symbol earlier for both TDD and FDD. By knowing the location of the mapping of this sequence in the two subframes it is possible to obtain frame synchronization.

The sequence is generated for the odd and even elements according to:

$$d(2n) = \begin{cases} s_0^{(m_0)}(n)c_0(n), \text{ in subframes } 0,1,2,3,4 \\ s_1^{(m_1)}(n)c_0(n), \text{ in subframes } 5,6,7,8,9 \end{cases} \quad (3.3)$$

$$d(2n+1) = \begin{cases} s_1^{(m_1)}(n)c_1(n)z_1^{(m_0)}(n), \text{ in subframes } 0,1,2,3,4 \\ s_0^{(m_0)}(n)c_1(n)z_1^{(m_1)}(n), \text{ in subframes } 5,6,7,8,9 \end{cases} \quad (3.4)$$

where:

- $0 \leq n \leq 30$
- m_0, m_1 : Indices derived from the physical layer cell identity $N_{ID}^{(1)}$;
- $s_0^{(m_0)}(n), s_1^{(m_1)}(n), z_0^{(m_0)}(n), z_1^{(m_1)}(n)$: m-sequences obtained from different indices m_0, m_1 by cyclic shifts of two primitive polynomials;
- $c_0(n), c_1(n)$: m-sequences depending of the sector identity group $N_{ID}^{(2)}$.

Refer to [3GPP17a] for the detailed generation of the SSS sequences. Similar to the PSS demodulation, the received signal cross-correlated with the total 168 sequences and evaluating the one that produces the maximum magnitude at the cross-correlator output. After successfully demodulating the PSS and SSS, one has complete frame synchronization and by knowing the grid structure employed in the OFDM system used in LTE, it is now possible to demodulate other types of signals in other radio channels.

The demodulation procedure can now be performed after obtaining frame synchronization and correcting the frequency offset experienced at the receiver with one FFT operation per received OFDM symbol to recover the received subcarrier values. The generated grid is a matrix of subcarriers per OFDM symbols, allowing an easy indexing mechanism to access the values of given resource elements such as cell-specific reference signals used for channel estimation, and received power calculation.

3.2.4 CQI Reporting and SINR Mapping

The link quality experienced by the secondary node, alike a regular UE, in a LTE cellular network is constantly changing along time due to the effects of noise, fading, interference created by other eNBs in surrounding networks, and the quality of the receiver. The transmitted signal by the eNB has to perform a link adaptation according to the channel quality for a given user, in order to match its requirements while providing certain levels of Quality of Service.

From the reference signals transmitted in DL, the secondary node determines three values used for channel estimation, namely the Channel Quality Indicator, Rank Indicator and Precoding Matrix Indicator. The procedure of link adaptation is based on the CQI value and is undertaken by Adaptive Modulation and Coding where the Modulation Coding Scheme is changed according to the link quality experienced at the UE. AMC works by measuring and feeding back the channel SINR to the transmitter, which then chooses a suitable MCS from a "code set" to maximize throughput at that SINR. In practice, the SINR value is not sent by the secondary node to the eNB, but the CQI parameter that corresponds to a range of SINR values. The CQI parameter is determined by the UE and can be directly mapped

according to certain ranges of experienced Signal-to-Noise-plus-Interference Ratio for a Block Error Rate (BLER) of 10%.

The mapping of the CQI indices in terms of MCS, coding rate and spectral efficiency C_c can be observed in Table 7.2.3-2 from [3GPP17b]. The mapping in terms of SINR value is given according to the tabulated spectral efficiency values in [3GPP17b], for a modulation coding scheme up to 256-QAM as LTE-A already has support for this modulation order, being based on a truncated Shannon limit formula found in [3GPP17c] as:

$$C_{c[\text{bit/s/Hz}]} = \begin{cases} 0 & , \text{ for } \rho_{IN[\text{dB}]} < \rho_{IN,\min[\text{dB}]} \\ \alpha S(\rho_{IN[\text{dB}]}), & \text{for } \rho_{IN,\min[\text{dB}]} \le \rho_{IN[\text{dB}]} \le \rho_{IN,\max[\text{dB}]} \\ C_{c,\max[\text{bit/s/Hz}]} & , \text{ for } \rho_{IN[\text{dB}]} > \rho_{IN,\max[\text{dB}]} \end{cases} \quad (3.5)$$

where:

- ρ_{IN} : Signal-to-Noise-plus-Interference Ratio;
- $S(\rho_{IN}) = \log_2(1+\rho_{IN})$;
- $\alpha = 0.75$.

The minimum and maximum values of SINR can be calculated by knowing the respective spectral efficiency for the highest and lowest CQI index. By replacing the tabulated spectral efficiency values from [3GPP17b] in (3.5), a range of SINR is obtained for each CQI index, allowing the mapping of each index in terms of the SINR value measured at the UE. This mapping can be found in Table 3.4, also showing which modulation coding scheme and coding rate is employed by CQI index and SINR range.

Table 3.4 - CQI and SINR mapping for AMC, adapted from [3GPP17b].

CQI Index	Modulation	code rate x 1024	$C_{c[\text{bit/s/Hz}]}$	$\rho_{IN[\text{dB}]}$
0	out of range			]-∞, -8.3586]
1	QPSK	78	0.1523	]-8.3586, -3.9686]
2	QPSK	193	0.3770	]-3.9686, 0.7592]
3	QPSK	449	0.8770	]0.7592, 4.3868]
4	16-QAM	378	1.4766	]4.3868, 6.5703]
5	16-QAM	490	1.9141	]6.5703, 8.8101]
6	16-QAM	616	2.4063	]8.8101, 10.2108]
7	64-QAM	466	2.7305	]10.2108, 12.6763]
8	64-QAM	567	3.3223	]12.6763, 15.0230]
9	64-QAM	666	3.9023	]15.0230, 17.4934]
10	64-QAM	772	4.5234	]17.4934, 19.8238]
11	64-QAM	873	5.1152	]19.8238, 21.5456]
12	256-QAM	711	5.5547	]21.5456, 24.1691]
13	256-QAM	797	6.2266	]24.1691, 26.8472]
14	256-QAM	885	6.9141	]26.8472, 28.7622]
15	256-QAM	948	7.4063	]28.7622, +∞[

Channel state can be reported periodically (2 –160 ms) using PUCCH or aperiodically (when requested by eNB) using PUSCH. To reduce the signaling overhead, the reporting is based on a wideband average feedback, an average of the best sub-bands where a single CQI is reported, or by using delta compression a CQI value for multiple each sub-band.

3.3 Performance Parameters

3.3.1 Proposed Scheme Throughput

The measured SINR at the receiver is calculated based on Cell-Specific Reference signals transmitted power in DL from the connected cell and surrounding interfering cells. Cell-Specific Reference Signals position depends on the number of antennas used at the transmitter and the cell-ID determined during the synchronization procedure. Although it does not transmit any specific information, it can deliver a reference point to the DL power transmitted by the eNB. The sequence format is defined in clause 6.10.1.1 in [3GPP17a] according to:

$$r_{l,ns}(m) = \frac{1}{\sqrt{2}}\left[1-2c(2m)\right] + j\frac{1}{\sqrt{2}}\left[1-2c(2m+1)\right] \quad (3.6)$$

where:

- n_s : Slot number;
- l : OFDM symbol number within the slot;
- $m = 0,1,...,2N_{RB}^{\max,DL} - 1$;
- $N_{RB}^{\max,DL}$: Maximum number of resource blocks for the measured bandwidth;
- $c(n)$: Pseudo-random sequence defined in clause 7.2 in [3GPP17a] for an initialization sequence dependent on the connected cell-id;

To apply different modulation coding schemes, the SINR value must be calculated for each resource block within a given period of time. After LTE demodulation, one has already obtained a resource grid in terms of OFDM symbols and sub-carriers for all received resource elements. The mapping of cell-specific reference signals in this grid can be used to determine the received power per resource block according to the number of antennas used on the transmitter. The received power per resource block for a given cell-ID can be calculated as the average squared magnitude of cell-specific reference signals contained in the resource block:

$$P_{r,RB_{[W]}}^{ID} = \left|\overline{r_{k,l}^{(p)} a_{k,l}^{*(p)}}\right|^2 \quad (3.7)$$

where:

- $r_{k-CRS,l-CRS}^{(p)}$: Received demodulated value of cell-specific reference signal mapped on resource element $(k-CRS, l-CRS)$ for antenna port p;
- $a_{k-CRS,l-CRS}^{(p)}$: Value of cell-specific reference signal mapped on resource element $(k-CRS, l-CRS)$ for antenna port p.

When performing the average for all the demodulated reference signals, fluctuations can occur within the individual RBs along a slot. To reduce the fluctuations that can be experienced along the different RBs along the slot, an alternative method is proposed where a single reference signal is considered to measure the received power. The secondary node can then determine the set of reference signals that originate a more constant received power and from then perform the SINR calculation. To differentiate the individual reference signals, one assigns different numbers for this type of signals within the resource block as presented in Figure 3.11.

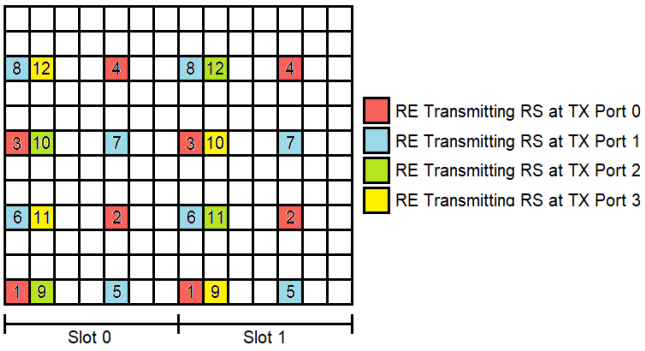

Figure 3.11 – Reference Signals Numbering.

In terms of SINR, one has to determine the received power from the interfering cells. The received power from each interfering cell is obtained in a similar manner as the connected cell, since its cell-id would change thus changing how cell-specific reference signals are generated and mapped to the LTE resource grid. The noise power level is assumed to be generated from thermal noise as the system can be considered interference-limited. By determining the received power per resource block from the connected cell and interfering cells, and calculating the noise power level considering MegaBEE receiving front-end noise factor N_f, the SINR value, $\rho_{IN,RB}$, is given by:

$$\rho_{IN,RB_{i[\mathrm{dB}]}} = 10\log_{10}\left(\frac{P_{r,RB_{[\mathrm{W}]}}^{ID_c}}{\sum_{i\neq c} P_{r,RB_{[\mathrm{W}]}}^{ID_i} + N_{RF,RB_{[\mathrm{W}]}}}\right) \tag{3.8}$$

where:

- $P_{r,RB_{[\mathrm{W}]}}^{ID_c}$: Received power per resource block of connected cell;
- $P_{r,RB_{[\mathrm{W}]}}^{IDi}$: Received power per resource block of interfering cell;
- $N_{RF,RB_{[\mathrm{W}]}} = k_{B_{[\mathrm{J/^oK}]}} T_{[^o\mathrm{K}]} \Delta f_{RB_{[\mathrm{Hz}]}} N_f$, $k_{B_{[\mathrm{J/^oK}]}} = 1.38\times10^{-23}\ \mathrm{J/^oK}$, $T_{[^o\mathrm{K}]} = 290\ ^o\mathrm{K}$,

$$\Delta f_{RB_{[\mathrm{Hz}]}} = 12 \times 15\,\mathrm{kHz} = 180000\,\mathrm{Hz}\,.$$

For the measured SINR value, the spectral efficiency can be directly determined by mapping the obtained value to the SINR range in Table 3.4, thus selecting which CQI index the UE/secondary node sends to the eNB and which modulation coding scheme is used for transmission. From Table 3.4, as the spectral efficiency is known, the throughput per resource block is simply given by the product of this value with the bandwidth a resource block occupies which is 12 sub-carriers spaced 15 kHz apart totaling a 180 kHz bandwidth.

The total throughput for a given slot can then be calculated as the sum of the individual throughputs of the total resource blocks for the whole bandwidth. This throughput can be considered optimal as all the resource blocks have an associated modulation coding scheme, being given by:

$$R_{b,s[\mathrm{bit/s}]}^{opt} = \sum_{i=1}^{N_{RB}^{DL}} R_{b,RB_i[\mathrm{bit/s}]} = \sum_{i=1}^{N_{RB}^{DL}} C_{c,RB_i[\mathrm{bit/s/Hz}]} \Delta_{f,RB[\mathrm{Hz}]} \tag{3.9}$$

where:

- R_{b,RB_i} : Individual throughput per resource block;
- C_{c,RB_i} : Individual spectral efficiency per resource block after MCS selection.

To reduce the signaling overhead created by adopting multiple modulation coding schemes per resource block, the proposed scheme determines a SINR threshold according to the measured CQIs of the first demodulated slot of a LTE frame, applying the same MCs for the following slots. Sudden changes in the channel behavior will result in the update of the MCS to be adapted for the following slots proceeding the fluctuation. The actual optimal individual throughputs as follows:

$$R_{b,RB_i[\mathrm{bit/s}]}^{act-opt} = \begin{cases} R_{b,RB_i[\mathrm{bit/s}]}, \text{ for } \rho_{IN,RB_i[\mathrm{dB}]} \geq \rho_{IN[\mathrm{dB}]}^{s_1} \\ 0 \quad\quad , \text{ for } \rho_{IN,RBi[\mathrm{dB}]} < \rho_{IN[\mathrm{dB}]}^{s_1} \end{cases} \tag{3.10}$$

The actual optimal throughput per slot would then be given by:

$$R_{b,s[\mathrm{bit/s}]}^{act-opt} = \sum_{i=1}^{N_{RB}^{DL}} R_{b,RB_i[\mathrm{bit/s}]}^{act-opt} \tag{3.11}$$

3.3.2 Expected Scheme Throughput

As referred in Chapter 3.2.4, the Modulation Coding Scheme is based on the wideband SINR resulting from the average or sub-band average measured received power, thus a single throughput or sub-band throughput is achieved for the assigned resource blocks. The average SINR can be formulated as:

$$\overline{\rho_{IN_{[\mathrm{dB}]}}} = 10\log_{10}\left(\frac{\overline{\mathrm{P}_{r,RB_{[\mathrm{W}]}}^{ID_c}}}{\sum_{i \neq c} \overline{\mathrm{P}_{r,RB_{[\mathrm{W}]}}^{ID_i}} + N_{RF,WB_{[\mathrm{W}]}}}\right) \tag{3.12}$$

The difference between (3.12) and (3.8) is not only in terms of the average received power per resource block being used as inputs, but also how the noise power level is determined as the whole bandwidth is now considered instead of bandwidth of a single resource block. The expected throughput per slot is given by:

$$R^{\exp}_{b,s[\text{bit/s}]} = \overline{C_{c,s}}_{[\text{bit/s/Hz}]} \Delta_{f,s[\text{Hz}]} \tag{3.13}$$

where:

- $\overline{C_{c,s}}$: Average spectral efficiency measured in a slot;
- $\Delta_{f,s}$: Transmitted DL signal bandwidth.

The actual throughput measured at the UE/secondary node differs from both optimal and average throughputs previously detailed. For the average throughput, a single Modulation Coding Scheme is selected based on the average SINR (3.12), creating a threshold for the actual throughput. The SINR values measured for individual resource blocks can be below the threshold imposed by the average SINR which means the actual throughput is lower than the expected average one. Considering the threshold effect on the calculated individual throughputs, the actual individual throughput is determined as follows:

$$R^{act}_{b,RB_i[\text{bit/s}]} = \begin{cases} R^{avg}_{b,RB[\text{bit/s}]}, \text{ for } \rho_{IN,RB_i[\text{dB}]} \geq \overline{\rho_{IN}}_{[\text{dB}]} \\ 0 \quad\quad , \text{for } \rho_{IN,RBi[\text{dB}]} < \overline{\rho_{IN}}_{[\text{dB}]} \end{cases} \tag{3.14}$$

Where $R^{avg}_{b,RB}$ is calculated for the average spectral efficiency $\overline{C_{c,s}}$ measured in a slot for a resource block bandwidth $\Delta_{f,RB}$.

The same procedure in (3.11) is applied to determine the actual throughput per slot as:

$$R^{act}_{b,s[\text{bit/s}]} = \sum_{i=1}^{N^{DL}_{RB}} R^{act}_{b,RB_i[\text{bit/s}]} \tag{3.15}$$

3.3.3 Throughput Gain

To observe the performance improvement of the proposed scheme in regard to the expected scheme, the throughput gain is calculated from the difference between the actual optimal throughput from (3.10) and actual throughput from (3.15) as:

$$G_{b,s[\%]} = \frac{(R^{act-opt}_{b,s[\text{bit/s}]} - R^{act}_{b,s[\text{bit/s}]})}{R^{act}_{b,s[\text{bit/s}]}} \times 100 \tag{3.16}$$

Each measured throughput can be enhanced by applying multiple antennas techniques. The MegaBEE equipment to be used in this thesis supports 8 antennas, being that there is two MegaBEEs available to perform the measurements. The total number of 16 antennas are considered for two multiple antenna

techniques, combining diversity and MIMO. For the experiments, two arrays of 8 antennas with each elementw spaced half of a wavelength apart in the configuration presented in Figure 3.12.

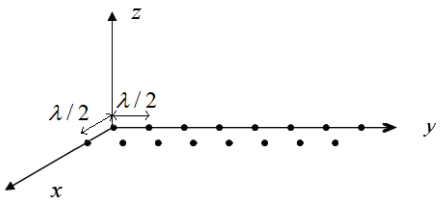

Figure 3.12 – Antenna array configuration.

Several arrays can be formed from this configuration to apply the referred multiple antennas techniques. The combining diversity algorithm considered can be implemented with, as the combined signal grid of RBs and slots is formed by choosing the maximum SINR measured at each antenna. The SINR grid in a RB *n* in slot *t* when considering this diversity combining algorithm can thus be defined as:

$$\rho_{IN,n,t\ [\mathrm{dB}]}^{div} = \max \rho_{IN,n,t\ [\mathrm{dB}]}^{(p)} \tag{3.17}$$

where:

- $\rho_{IN,n,t}^{(p)}$: Measured SINR in RB *n* in slot *t* for antenna port *p.*

The calculation of the expected throughput and optimal throughput and corresponding actual throughputs would then take into account the SINR grid created from the combining diversity to determine the CQI index to report to the eNB. The diversity gain in terms of throughput is thus given by the difference of the throughputs measured for the studied schemes, expected and proposed, considering combining diversity as:

$$G_{b,s[\%]}^{div} = \frac{(R_{b,s[\mathrm{bit/s}]}^{act-opt_{div}} - R_{b,s[\mathrm{bit/s}]}^{act_{div}})}{R_{b,s[\mathrm{bit/s}]}^{act_{div}}} \times 100 \tag{3.18}$$

The spacing of each antenna element allows to consider each received signal as independent between each other, thus enabling the use of MIMO and beamforming as long as all the elements are synchronized. The use of MIMO is dependent on the number of antennas employed at the transmitter, as the current LTE-A standards only support up to 8x8 antennas [3GPP16b], while the considered receiver employs 16 antennas as mentioned before. MIMO can thus be applied to the order of antennas employed at the transmitter side, being that the received signal for the individual antennas or antenna array can be summed to replicate the effects of using this technique. The diversity combining algorithm can be used to enable multiple antennas to act as one and measure the throughputs obtained for each considered set. The number of sets considered to apply MIMO will be also dependent on the number of antennas at the transmitter. The diversity gain for MIMO will be the difference between the actual optimal throughput and the actual throughput obtained with MIMO as:

$$G_{b,s[\%]}^{MIMO} = \frac{(R_{b,s[\mathrm{bit/s}]}^{act-opt_{MIMO}} - R_{b,s[\mathrm{bit/s}]}^{act_{MIMO}})}{R_{b,s[\mathrm{bit/s}]}^{act_{MIMO}}} \times 100 \tag{3.19}$$

3.3.4 Fairness Index

The fairness index for the different scheduling algorithms is obtained according to Jain's Fairness Index, being calculated for each LTE slot. The fairness index is thus given by:

$$F_{index} = \frac{\left(\sum_{i=1}^{N_{\text{sec}\,nodes}} R_{b_i[\text{bit/s}]} \right)^2}{N_{\text{sec}\,nodes} \sum_{i=1}^{N_{\text{sec}\,nodes}} R_{b_i[\text{bit/s}]}^{\ 2}} \tag{3.20}$$

where:

- R_{b_i} : Throughput of secondary node *i*;
- $N_{\text{sec}\,nodes}$: Number of secondary nodes to be scheduled.

The fairness index will vary (in the worst condition) inversely proportional to the number of secondary nodes being equal to 1 (best condition).

3.4 Model Implementation

3.4.1 Model Workflow

The model to be implemented is divided in four modules referring to operations performed at the primary and secondary nodes. The workflow for the model implementation and subsequent integration is described in Figure 3.13. The first module of the model is the receiver configuration. The three methods for data acquisition were implemented in Simulink by creating a model with blocks corresponding to hardware interfaces with the BPS distribution and Vivado System Generator for DSP libraries. When the design is completed and properly simulated to work as expected, a .slx file is generated which in turn will be used to generate the bitstream with a .fpga extension to program the FPGA in the MegaBEE. The configuration of the MegaBEE follows, with the selection of the several parameters to be used during the captures, namely carrier frequency, sampling frequency, filter bank and bandwidth.

This configuration is done in a remotely controlled terminal shell in the MegaBEE using firmware to configure the parameters set in file with a .conf extension. When all the parameters are set, the data acquisition can be initialized by controlling the design programmed in the FPGA via Software Registers. The data collected is stored in files with a .txt format, files' content varying from method to method.

The second module refers to signal processing with the acquired data, namely in terms of cell synchronization, carrier frequency offset correction, performing after demodulation this processing phase. This analysis is done in MATLAB using LTE's System Toolbox [Math17] based on the example for Cell Search, MIB and SIB1 Recovery [BaFr15]. This step will provide a synchronized demodulated grid in terms of OFDM symbols and subcarriers and the cell-id from which capture was synchronized to.

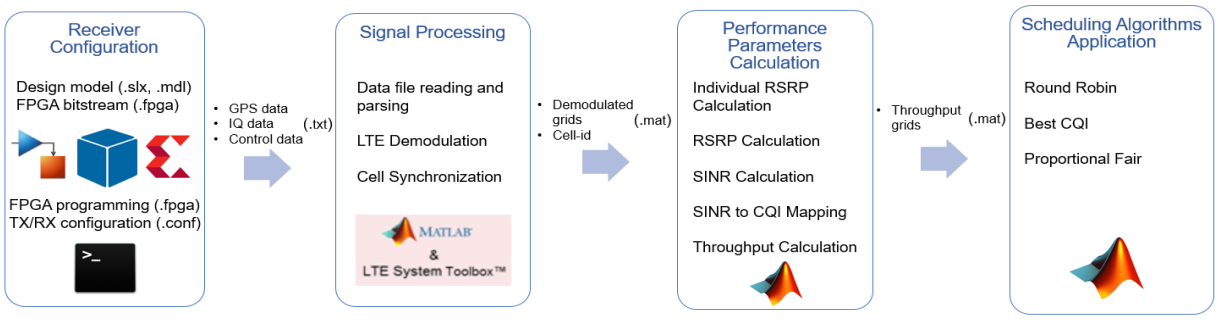

Figure 3.13 – Model Workflow.

The demodulated grid and cell-ids will be used in the third module to perform the calculation of the performance parameters, namely the calculation of the average wideband received power and a similar measurement for individual resource blocks. During this third step, the SINR value will be calculated for the individual PRBs and the average SINR in all bandwidth. From this two SINR values, one then performs the mapping from SINR to CQI index and thus determine the throughput values for the proposed scheme using individual PRBs SINR and the expected throughput based on the average SINR in all bandwidth. The throughputs obtained in the third module will be used to apply three scheduling algorithms in the fourth module, finalizing with a comparison between each scheduling algorithm.

3.4.2 DMA Method

The data acquisition methods for the secondary node referred in Chapter 3.1, are all programmed in MATLAB's Simulink environment with blocks from Simulink, BPS and, Vivado System Generator for DSP libraries. The implemented models for the three data acquisition methods resulted from an adaptation of the already existing designs provided with BPS installation. In Annex A, the implementation of the BRAM and XGE Method is presented.

The block diagram for the implementation of the DMA Method is represented in Figure 3.14, where a subsystem named "RX" controls its inputs and outputs for data acquisition purposes. The DMA FIFO block provided by BPS has four ports to control the transfer flow and one for the data to be transferred. Since transfers can occur from the PL to the PS and vice-versa, the DMA FIFO block has a total of ten I/O ports, using five of them for each transfer direction.

As the goal this method is to generate a RF receiver, only five ports are considered, being that the ports for the transmitting side are connected either to Simulink "Terminator" blocks or to constant signals. For both directions, the PS is always the master of the DMA FIFO interface. The aforementioned five ports for the RX side, control whether the data is valid in terms of size and content, when the FIFO is ready to be written, and to assert the boundary of the full data to be transferred.

The assignment of the control flags for the transfer is achieved by using a Software Register labelled "adc_capture" as seen in Figure 3.15 (a). Since the software register has a data bit-width of 32 bits, the least significant bit is sliced to reproduce an impulse function after "the rising edge" subsystem.

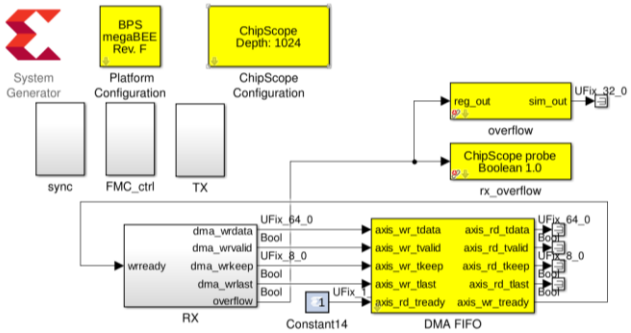

Figure 3.14 – BPS high-level model for the DMA Method.

The generated impulse is then used in the “enable” subsystem in Figure 3.15 (b) that sets the number of 64-bit words to be transferred in each capture. After trial and error, the maximum number of samples that can be acquired in a single capture for one port was concluded to be 507 903 samples, totaling 1 015 806 bytes. When using four ports the total number of captured samples is 2 031 612 samples.

To synchronize multiple MegaBEE platforms and each side of the MegaBEE, the “adc_capture” signal is used as a synchronization signal for other boards by making use of General Purposes Input/Output (GPIO) blocks. GPIO blocks, create an interface between the additional inputs and outputs of the MegaBEE, allowing to send signals to each side of the MegaBEE or other stacked platforms, using a physical connection.

The trigger signal “adc_capture” after being sliced of its least significant bit is thus sent to other boards by connecting to GPIO “sync_out” block, which in turn will be physically connected to the Sync In input. Using the “sync_in” GPIO block, one can access the Sync In input and mimic the behavior of the “adc_capture” by using a simple OR logical gate. The four sides of the two MegaBEE are then controlled by a single side to trigger the capture process, achieving synchronization between the captured signal in the 16 antennas.

The trigger signal and the number of samples to be transferred are used as input for the subsystem “wr_gen”, for a counter and two comparators, as seen in Figure 3.15 (c). Every time the Software Register “adc_capture” changes its value from 0 to 1 during one cycle, it is used to reset the counter block. This counter is only enabled when its output is smaller than the value of number of samples to be transferred, and when the flag TREADY is assigned. To achieve this, the Relational block is used, not only to enable the counter but also to assign the TVALID flag and thus enabling a DMA transfer to occur.

When the output of the counter is equal to the value written in the Software Register, the TLAST flag is assigned indicating the last beat of the transfer. The data to be transferred is blind to this process, meaning that while this procedure occurs, the receiver is constantly streaming IQ samples every four clock cycles, being stored only the ones that are provided when the flags TREADY and TVALID are assigned at the same time. As the TREADY flag is generated in hardware to indicate when the PS is ready to receive more data, the TVALID flag cannot be always assigned as the hardware may not be capable to be constantly receiving new data.

To overcome this limitation, the TVALID flag is assigned periodically with a square wave shape, being assigned twice every clock cycle. As RF data is generated every four clock cycles, the first TVALID

assignment allows the transfer from the bottom FMC-112 board, comprising ports 0 and 1 of a MegaBEE side, while the second assignment allows the transfer from the top board, thus ports 2 and 3. To detect data transfer overflow, a flag “overflow” is generated whenever the TREADY flags is not assigned and TVALID flag is. For the TKEEP flag, it remains constant with the value 255, since all the transmitted data is processed as part of the data stream to be transferred.

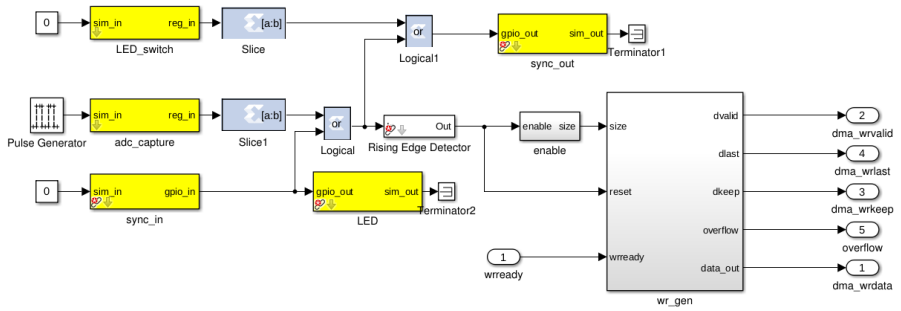

(a) “RX” Simulink Subsystem.

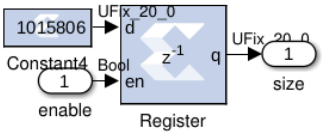

(b) “enable” Simulink Subsystem.

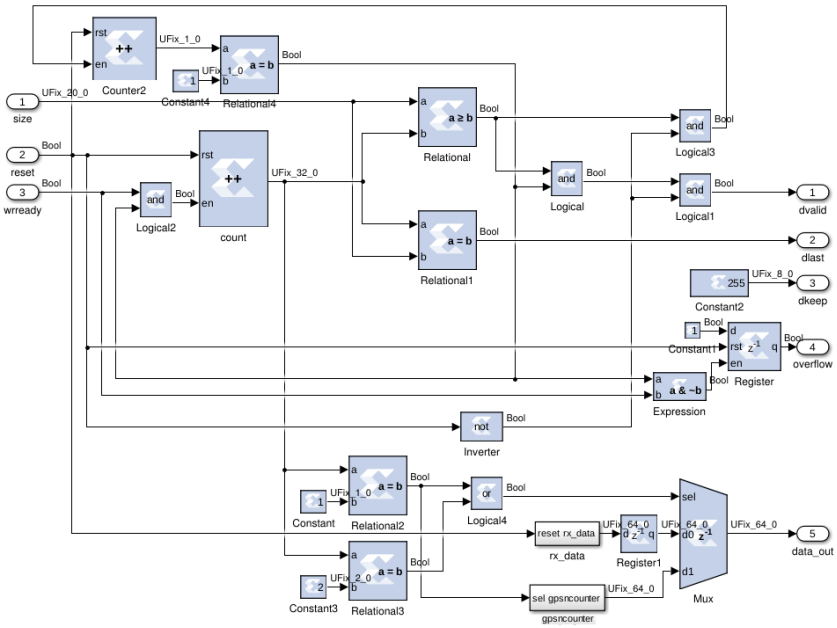

(c) “wr_gen” Simulink Subsystem.

Figure 3.15 – Mechanism for DMA method.

The multiplexing engine makes use of the counter “count” in Figure 3.15 (c) to control which 64-bit word is transferred. The first counting cycle is used to transfer the reference counter data, while the second counting cycle stores GPS data. For the proceeding counting cycles, RF data from the 4 ports are transferred, being that the data for each board is also multiplexed by using a 1-bit counter that will either select received data from the bottom FMC-112 board or the top board as seen in Figure 3.16 (a). From Figure 3.16 (b), one can see that the reference counter is just a free running 32-bit counter, while the

GPS data is generated by writing the contents of the serial connection onto four Software registers which in turn will store the integer and fractional part of both latitude and longitude.

Nonetheless, the Software Register trigger needs to be written twice for each transfer, which means that there will be gaps between the captured data. To overcome this issue, the mechanism for writing and reading the FIFO must be optimized in order to avoid any buffer overflow and underflow.

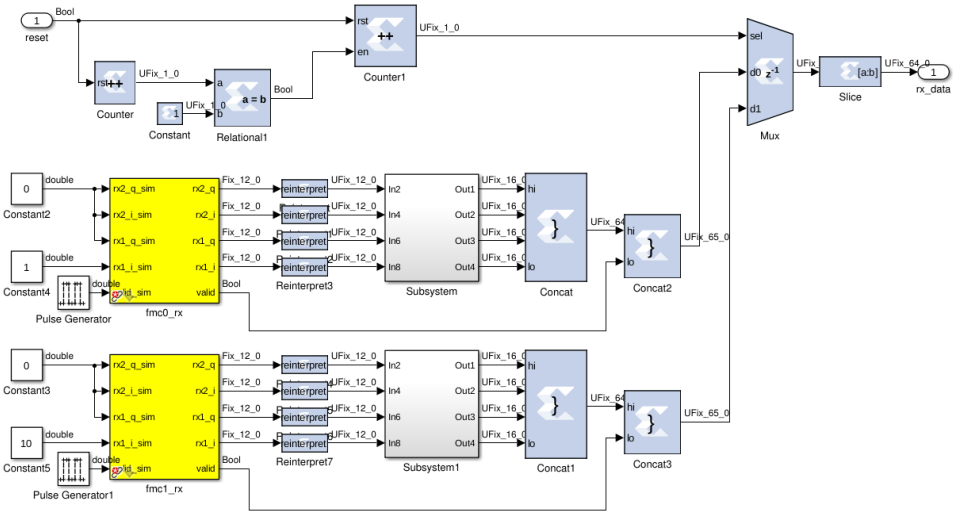

(a) "rx_data" Subsystem – RF data multiplexing.

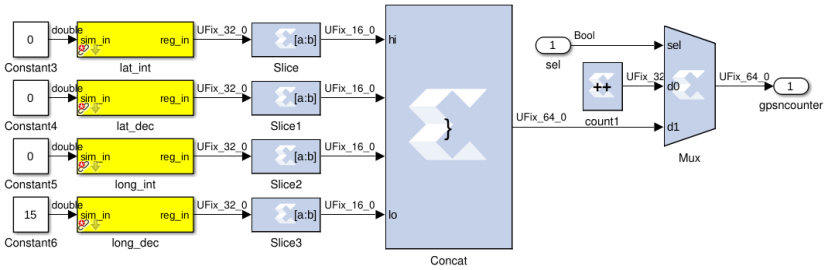

(b) "gpsncounter" Subsystem – GPS and Counter multiplexing.

Figure 3.16 – Data to be transferred using DMA Method.

Because there is a mismatch in data sizes for transfers from the PL to the PS on the driver associated with the DMA FIFO the continuous acquisition was discarded, as the PS host would hang when the requested read size was smaller than the size written on the FIFO. When reading the exact same size that was written, this issue would not happen, thus enabling the capture of about half million IQ samples from two RF ports of the MegaBEE. The reference counter can then be used to determine the timing gap, Δt_c, between captures as:

$$\Delta t_c = \frac{n(k+1) - n(k)}{f_{CLK}} \tag{3.21}$$

where:

- f_{CLK} : System's clock rate, four times the sampling frequency f_S ;

- $n(k)$: Counter value at capture k .

3.4.3 Scheduling Algorithms Implementation

The scheduling algorithms used in the analysis were all implemented in MATLAB. The first considered algorithm is Round Robin, a scheduling algorithm of low complexity that handles resource allocation by the means of rounds or turns. This meaning that each user has a resource allocated to him/her the next resource being allocated to the following users, this procedure continuing until there are no more resources to allocate or users to schedule. For the proposed scheme, the algorithm implementation is presented in Figure 3.17, for the allocation of user k_i considering N users, 20 slots and 100 Physical Resource Blocks (PRB) to allocate within a slot. By having low complexity, this algorithm is easily implemented by a scheduler, assuring the fairness among different users in terms of allocation, but not considering channel state conditions to optimize individual experienced or overall cell throughput.

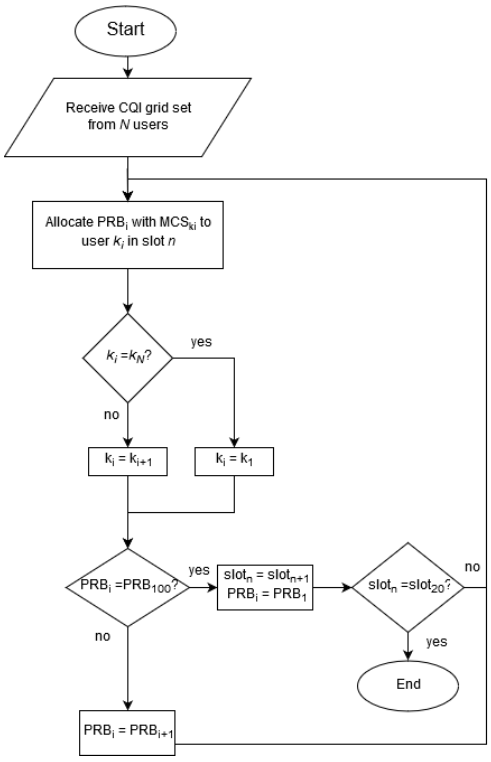

Figure 3.17 – Round Robin Algorithm Implementation.

To optimize cell capacity, the best CQI algorithm is implemented, which consists of the selection of the Best CQI measured by the different users. The CQI value sent by the multiple users is used by the eNB to perform the scheduling, allocating a given resource to the user experiencing the best channel conditions. This algorithm completely disregards fairness among users to optimize cell throughput, creating the chance of users that are not allocated merely due to their worst channel conditions. Cell-edge users are often the users that suffer most with this scheduling algorithm, while users closer to the eNB have the best performance. The algorithm for the proposed scheme is shown in Figure 3.18, for the same conditions as the Round Robin scheduling algorithm.

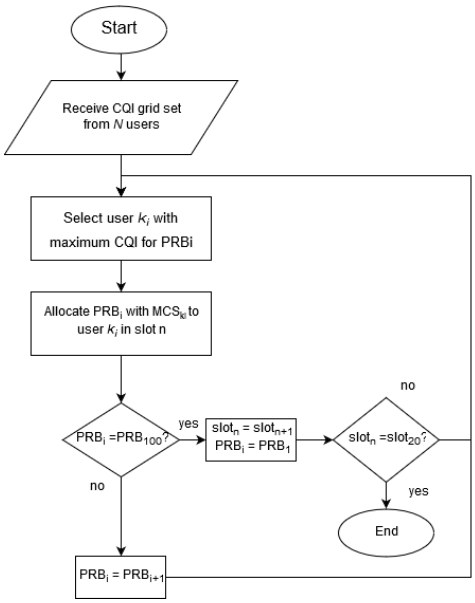

Figure 3.18 – Best CQI Algorithm Implementation.

The third algorithm consists of a middle ground between the Round Robin and the Best CQI algorithm, being known as Proportional Fair scheduling, providing a balance between fairness and the overall system throughput. The Proportional Fair algorithm achieves this balance by considering the instantaneous channel conditions and previous channel conditions, performing a moving average with a length of t_c. The allocated user k^* is thus the one which current and past channel conditions optimize the following condition [BaKo13]:

$$k^* = \arg\max_{k=k_1,\ldots,k_N} \frac{R_{k,n}(t)}{T_{k,n}(t)} \tag{3.22}$$

where:

- $R_{k,n}(t)$: Requested data rate of each UE/secondary node k in PRB n for slot t;
- $T_{k,n}(t)$: average throughput of each UE/secondary node k in PRB n for slot t within a past window t_c length.

The eNB can update the average throughput $T_{k,n}(t)$ value in a recursive way as follows:

$$T_{k,n}(t+1) = \begin{cases} \left(1-\frac{1}{t_c}\right)T_{k,n}(t) + \frac{1}{t_c}R_{k,n}(t), & k^* = k \\ \left(1-\frac{1}{t_c}\right)T_{k,n}(t), & k^* \neq k \end{cases} \tag{3.23}$$

This algorithm is presented in Figure 3.19 for the same conditions as the previous ones. Fairness is guaranteed in this algorithm in the long term, however no guarantees are given in terms of the delay to perform the scheduling caused by the added complexity to implement the algorithm. Each algorithm is

flexible to work with different types of CQI reporting. For sub-band reporting, each algorithm allocates a sub-band with a given number of RBs to the secondary node that follows each algorithm conditions.

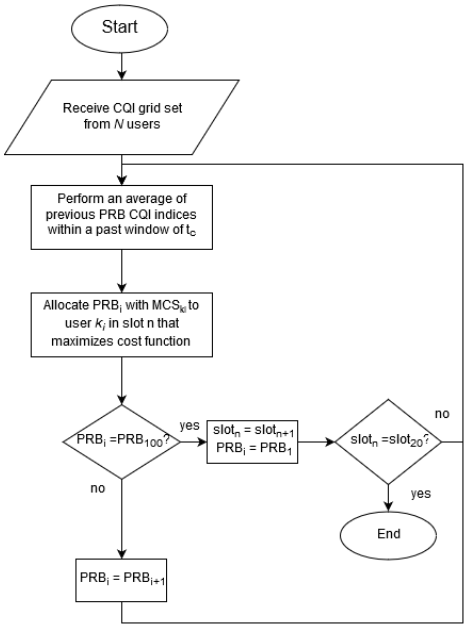

Figure 3.19 – Proportional Fair Algorithm Implementation.

3.5 Model Assessment

Several tests were performed on the four modules that compose the final model, being done in a sequential way, meaning that only when a module was completely tested and assessed its functionality, the following module was tested. As the third module refers only to the calculation of the performance parameters for the proposed scheme, its functionality is assured by the assessment of the previous two modules of data acquisition and data processing.

For the first module regarding the data acquisition methods in the MegaBEE, simulations were performed for the several subsystems for each method. The simulations results are fully presented and explained in Annex B. The overall assessment of the different methods leads to the choice of the DMA Method for data acquisition. Although the simulations in all three methods behave as expected, the BRAM and XGE Methods in practice do not offer the flexibility of the DMA Method, being from the capture delay and reduced number of captured samples in the former and package loss rate in the latter.

The second module was tested by performing the demodulation and cell synchronization on the generated .txt files with the received data. To assess the functionality of this module, the obtained information from demodulation procedure was compared against the one obtained using Iphone's embedded Test Field Mode [MNGu14]. The initial measurement was done in the crossroad between Russel & Huron Streets in University of Toronto, where the MegaBEE was on top of a stationary vehicle. Prior to data acquisition, the information on Iphone's Test Field Mode was stored, Figure 3.20.

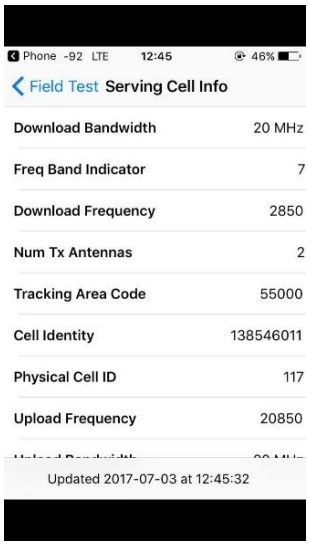

Figure 3.20 – Iphone Test Field Measurement.

The serving cell info being displayed in Figure 3.20, shows a Physical Cell ID valued 117, two transmitting antennas and LTE's frequency band 7 with a bandwidth of 20 MHz. The Download Frequency value corresponds to the EUTRA Absolute radio-frequency channel number (ARFCN), indicating that the DL carrier frequency is 2.630 GHz. Knowing these parameters, the transceiver in the MegaBEE was configured accordingly in terms of the receiving carrier frequency, sampling frequency, bandwidth and filter bank. A capture was performed, and the contents of the generated data file were read and parsed providing data for the location where capture was performed and four IQ signals for the four ports in a MegaBEE side. The channel frequency response for Port 0 can be seen in Figure 3.21, where the magnitude is normalized to the measured maximum value.

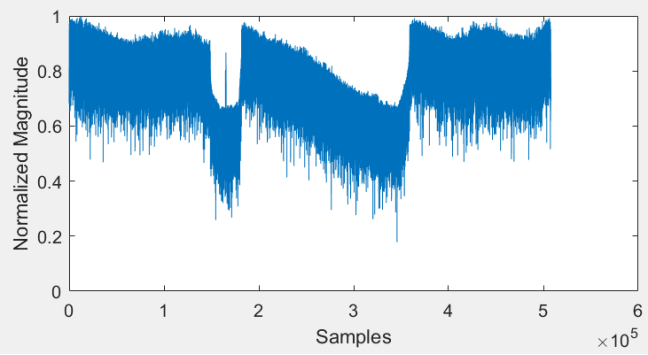

Figure 3.21 – Channel Frequency Response for Port 0.

The obtained results after demodulation procedure are shown in Figure 3.22, where a structure variable comprises all the information obtained in this module for the different ports. After the demodulation procedure, one can see that for each port the obtained data is the same, which means that there is full synchronization between the four considered ports. The obtained information also matches the one seen in Iphone's Test Field Mode in Figure 3.20 regarding the Physical Cell-ID, number of transmitting antennas given by the number of detected Cell Reference Ports value of 2, a bandwidth of 20 MHz shown by the detected number of RBs of 100 and lastly the duplexing and cyclic prefix length being FDD and Normal respectively.

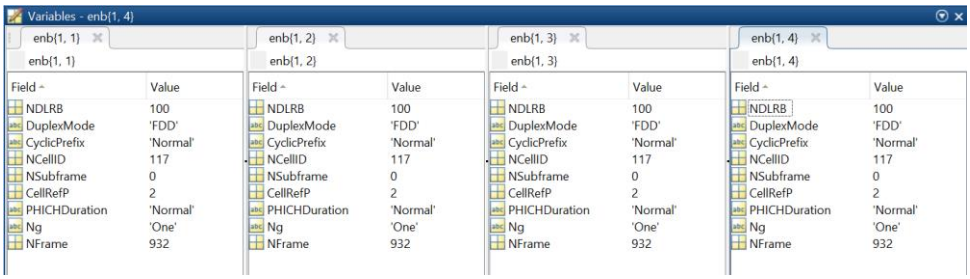

Figure 3.22 – Demodulation procedure.

Since there was still no information regarding the interfering cells at this point, the assessment of the third module was done in terms of the evaluation of the received power for individual PRBs and average power for an entire slot. The performed tests can be found in Table 3.5.

Table 3.5 – Assessment tests for the third module.

Test	Description
1	Check if the demodulated grid possesses a number of slots greater or equal than 20 to comprise an entire LTE frame.
2	Check if the demodulated grid possesses the same number of demodulated slots in all ports.
3	Check if frame number obtained in the demodulation procedure is consistent within the ports, to assess the synchronization between ports.
4	Validation of the location of the cell-specific reference signals according to the cell-id and subframe number.
5	Assure that the location and value of cell-specific reference signals is updated along the frame to properly calculate the individual RB received power.
6	Assure data structures for storing the performance parameters can handle multiple cells and multiple ports for further SINR value calculation.
7	Check for fluctuations caused by the average of the received power in cell-specific reference signals, and if it is attenuated when considering individual cell-specific reference signals.

The assessment of the fourth and final module was done using a simple test. Two secondary nodes were scheduled using the full totality of resource blocks to allocate, given that the first secondary node had bad channel conditions and second secondary node had good ones. One assumed that the first secondary node was located on a cell edge and its CQI reported range from index 0 to index 7, while the second secondary node was located on the cell center reporting CQI indices from the range of 8 to 15. To replicate these effects two CQI grids in terms of slots and RBs, were created for the two secondary nodes. The grids were populated by using MATLAB's function *randi* to choose a random number from two vectors containing the CQI indices for the two secondary nodes. The simulated results are presented in Figure 3.23.

The Best CQI scheduling algorithm obtained behavior is that the secondary node with the best channel conditions will always be allocated to maximize the total cell throughput, at the cost of over allocating resources to the secondary node with the best channel conditions. For the Round-Robin Algorithm it the second secondary node has a higher throughput than the first secondary node and a reduced throughput compared to the proportional fair algorithm and Best CQI algorithm. The proportional fair algorithm behavior reflects a higher throughput to the user with the best channel conditions, however the total cell throughput is higher than the Round Robin algorithm as well as the secondary with worst channel conditions.

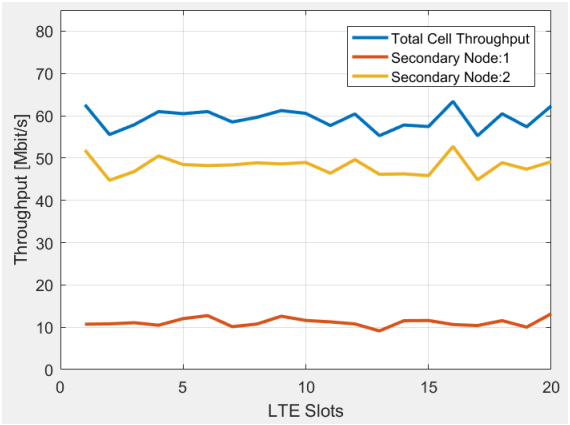

(a) Round Robin Algorithm.

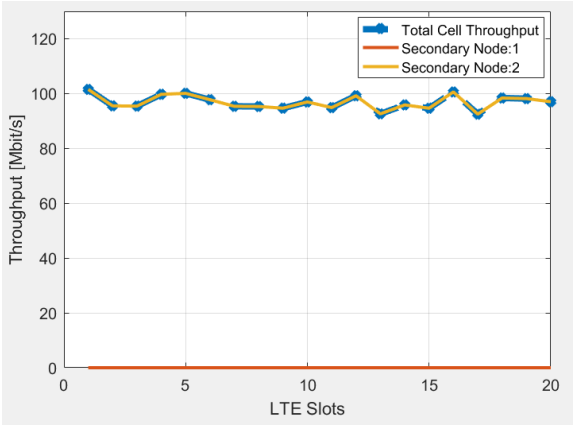

(b) Best CQI Algorithm.

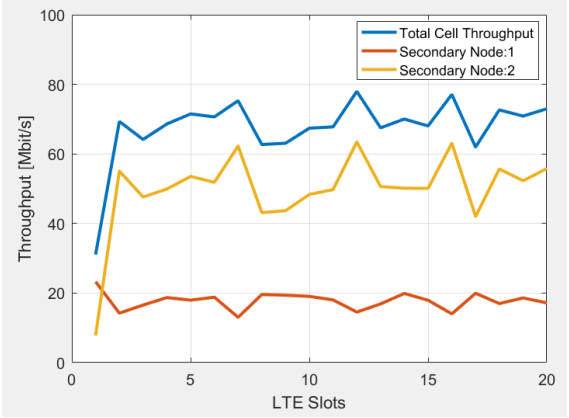

(c) Proportional Fair Algorithm.

Figure 3.23 – Scheduling Algorithms performance for simulated data.

Chapter 4

Measurements and Results Analysis

This chapter presents the scenarios taken for the evaluation of the proposed and expected throughput schemes, the obtained results and its analysis. In the first section the two scenarios under study are described, a sparse and dense deployment with the reference scenario being the former. An evaluation of the throughput schemes and scheduling algorithms is done for the reference scenario considering multiple antennas. For the dense scenario, only the evaluation of the throughput schemes is performed.

4.1 Scenarios Description

The scenario under evaluation takes place in the city of Toronto, a vast urban environment being the fourth biggest city in North America with a population of 2 731 571 inhabitants [SC17a]. In particular, the scenario location takes place in the University of Toronto St George Campus and its surroundings, within the 20th and 27th Ward of the East York district. For the updated census, [SC17b] and [SC17c], on the referred Wards, the total population is 155 270 inhabitants, however for the location in case of the University of Toronto the total number of students of 60 595 [UTor17] in St. George Campus is a better indicator of the order of inhabitants in this location. The number of inhabitants in this region provides a general idea of the type of cellular deployment in question as a typical urban environment. To obtain a better sense on how the cellular network is deployed, an initial run in terms of cell synchronization was performed using the DMA method for data acquisition.

The cell synchronization procedure enables to perform an estimation of the coverage area of the cells in the measured environment by providing an indicator of which cell the secondary node is synchronized to. Recordings of the Iphone's Test Field Menu were done in parallel to obtain the Tracking Area Code, Cell Identity and Physical Cell-id of each cell. These parameters were then used to gather an estimation of the location of the base stations using an online application for cell location, LocationAPI [LAPI17]. The recordings are presented in Annex C. The obtained results are presented in Figure 4.1, where each small marker corresponds to a DMA capture and a big marker the estimated location of the eNB.

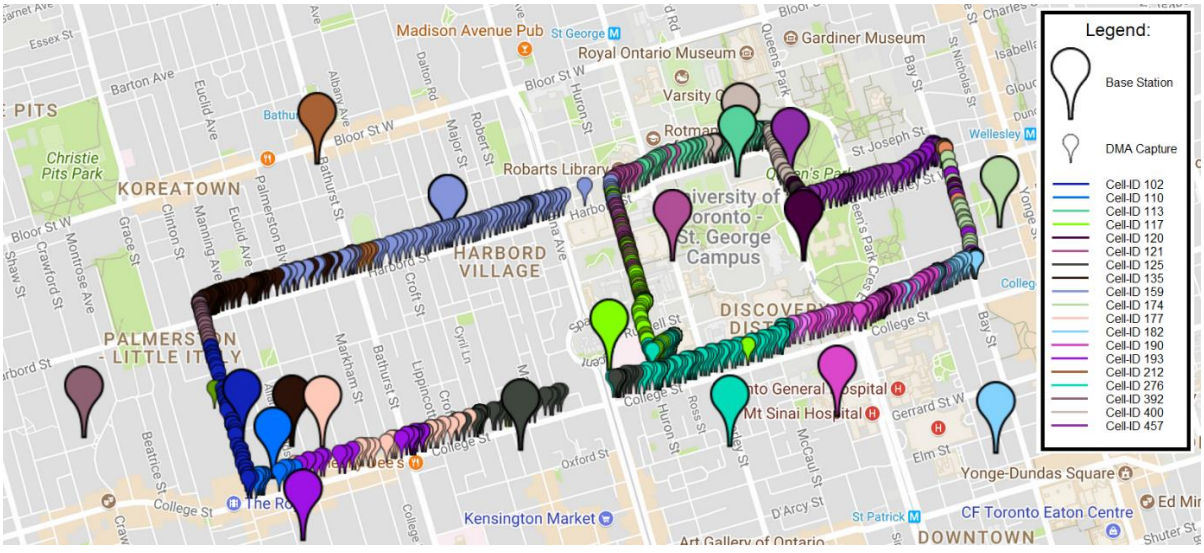

Figure 4.1 – University of Toronto Synchronization Mapping.

Distinct colors in the markers represent different cell-ids, DMA captures being synchronized to a given base station when their markers share the same color. Several scenarios can be built around the synchronization mapping, the type of deployment that is being dealt around this location being also evidenced.

The assumption taken to define the type of deployment in the measurements location refers to the eNBs density, given that for the synchronization mapping in question, one can define two different deployments, sparse and dense. As shown in Table 2.4, the type of cell deployed in this environment can be interpreted as a micro/metro-cell according to the boundaries of the synchronized DMA captures. A metric is defined to assess if a DMA capture is within a sparse or dense deployment. The rule of thumb used to differ the two types of deployments is based on the number of cells within a radius of 500 m of a DMA capture. The radius was chosen as it is the average coverage radius considered for micro/metro-cells in Table 2.4. In Figure 4.2, one can see the two types of deployment in green and red.

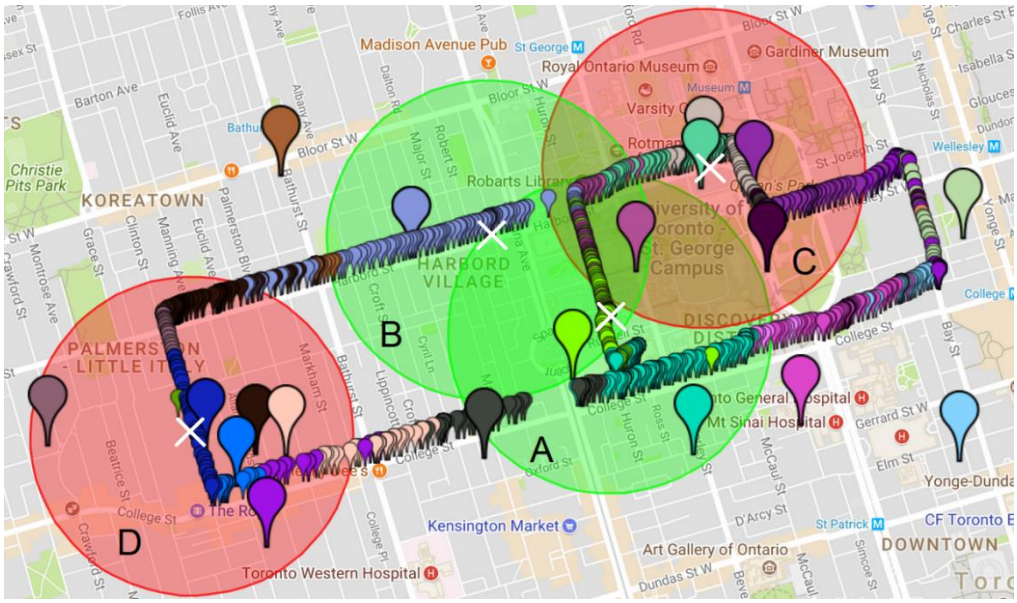

Figure 4.2 – Sparse and Dense Deployments.

As presented in Figure 4.2, in green, the sparse deployments A and B have up to 3 cells within a radius of 500 m. In red, the dense deployments C and D have more than 3 cells within the same radius. In the dense deployments, as the radius decreases the number of cells within the circle remain the same meaning that the cell density is far greater than the sparse deployment one. The center of each circle is marked with a white cross, being located on the same location of a capture used for the analysis. As the proposed scheme is expected to have a better performance considering a static secondary node, a reference scenario is built from the synchronization mapping. The reference scenario under analysis will thus be the one referring to a sparse cellular deployment considering a static secondary node.

The location used as a reference scenario was the crossroads between Russel and Huron Streets in University of Toronto. In a similar fashion, another scenario can be built based on the reference one just by changing its characteristic referring to the deployment site. The characteristic under changes in this scenario pertains to a static secondary node within a dense deployment zone, being just a switch of the deployment site. The deployment for this scenario was on the crossroads between Hoskin Avenue and Tower Road in University of Toronto in dense deployment C.

The measured radio channel belongs to LTE band 7, with a central carrier of 2.630 GHz, a bandwidth of 20 MHz, and two transmitter antennas. The receiver configuration is presented in Figure 4.3 within a

plywood case being at the top of the vehicle. The receiver consists of two MegaBEEs comprising sixteen antennas for the RF frontend and four antennas to acquire GPS coordinates.

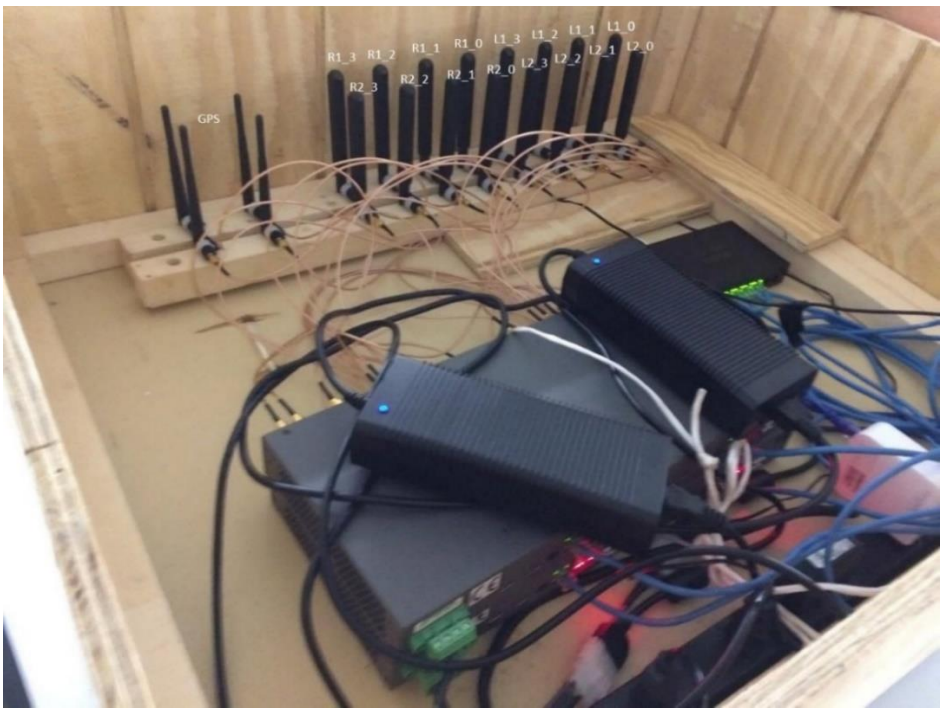

Figure 4.3 – Equipment Setup.

The label on the RF frontend antennas follows the nomenclature in Table 4.1:

Table 4.1 – Antenna Ports Nomenclature.

	Port 0	**Port 1**	**Port 2**	**Port 3**
MegaBEE 1 Left Side	L1_0	L1_1	L1_2	L1_3
MegaBEE 1 Right Side	R1_0	R1_1	R1_2	R1_3
MegaBEE 2 Left Side	L2_0	L2_1	L2_2	L2_3
MegaBEE 2 Right Side	R2_0	R2_1	R2_2	R2_3

For all considered scenarios, the parameters that do not undergo any change refer to the receiver and transmitter configurations. The SMA cables used to connect the antennas to the MegaBEE inputs are 60.96 m long and a plywood case was used to store all the equipment on the top of a vehicle. All the parameters taken for the measurements are summarized in Table 4.2.

The two antennas at the transmitter indicates that there 8 reference signals to perform the received power calculation for both individual resource blocks and wideband, given that each antenna port at the transmitter transmits 4 reference signals per resource block.

Prior to measurements, a calibration of the MegaBEE was undertaken in terms of the offset between its receiver local oscillator and measured carrier frequency. Using the signal generator HPE4432B a sinusoidal wave with a carrier frequency of 2.630 GHz was fed to one of the RF ports inputs of the

MegaBEE. Using the DMA method to transfer the received data, the central frequency of the captured wave was determined by performing a simple FFT operation. The received signal frequency value was equal to the offset of the signal generator and MegaBEE local oscillator. By tuning the voltage level fed to auxiliary DAC (AUXDAC2) of the MegaBEE, one could minimize the obtained frequency offset.

Table 4.2 – Measurements Constant Parameters.

Parameter	Value	Reference
Number of Antennas at Transmitter	2	-
Number of Antennas at Receiver	16	-
Receiver Height	1.44 m	[Toyo17]
Capture length	10-15 ms	-
Frequency band	LTE band 7	-
Signal Bandwidth	20 MHz	-
Receiver Noise Factor	7 dB	[BEEc16c]
Antennas Gain	2.04 dBi	[Taog17]
SMA Cables Attenuation	1.16 dB	[Past13]
SMA Connector Attenuation	-	[Digi17a]
Plywood Case Attenuation	-0.0801 dB	[Wils02]

The AUXDAC2 voltage level was thus used to tune the reference crystal on the FMC112 used as the local oscillator, using firmware commands that changed the voltage levels 1 mV for each DMA capture. The voltage level was tuned in the range of [1000, 1500] mV, thus 500 DMA captures were performed, given that for each capture the frequency value of the received signal was determined. The frequency offset value in terms of the voltage level of the AUXDAC2 can be observed in Figure 4.4. The minimum frequency offset value was obtained for an AUXDAC voltage level of approximately 1320 mV, for an accuracy of 60 Hz at a sampling frequency of 30.72 Msamples/s for capture length of 15 ms.

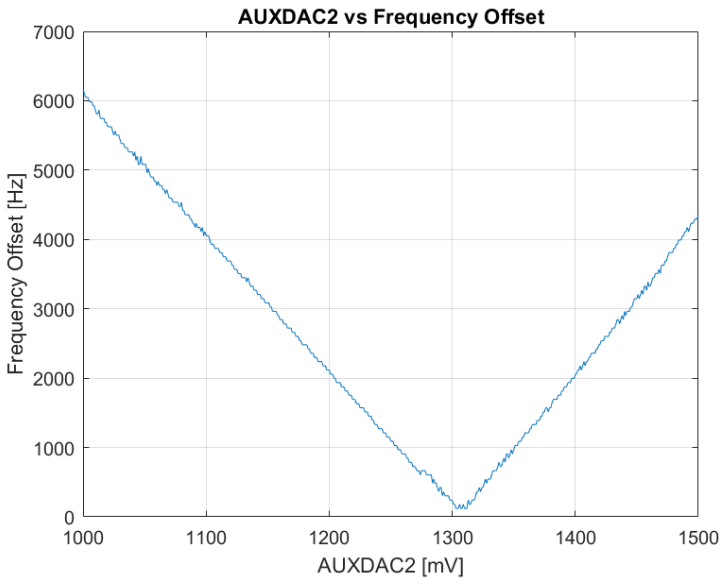

Figure 4.4 – Local Oscillator Calibration.

4.2 Sparse Deployment Scenario

4.2.1 Proposed Allocation Scheme Performance

The results obtained for the sparse deployment scenario refer to the 30 captures performed at the crossroad of Russel and Huron streets. The capture site can be seen in Figure 4.5, along with the closest cells within a radius of 500 m. In terms of synchronization, all the 30 captures are synchronized to the eNB with the physical cell-ID 117 (green).

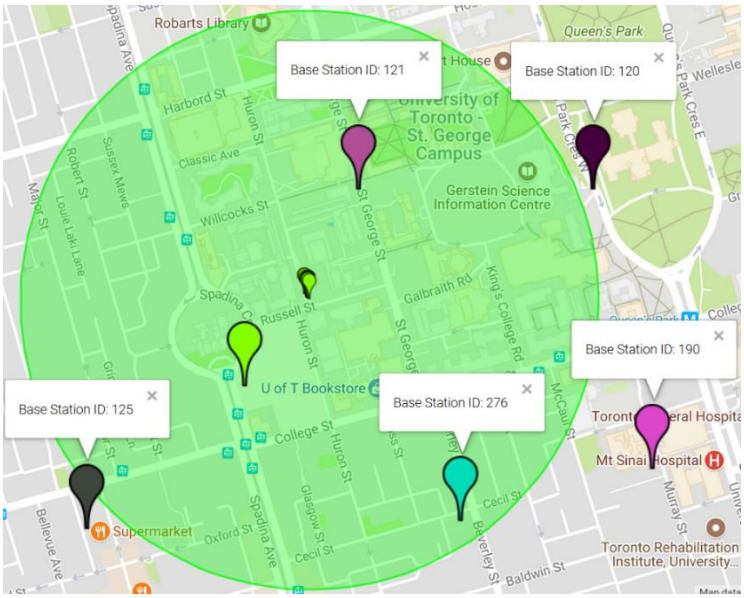

Figure 4.5 – Reference Scenario Capture Site.

For the SINR calculation, only two eNBs are considered as interferers for being the closest cells to the capture site, with the cell-IDs, 121 and 276. As the reference scenario defined a radius of 500 m for the sparse deployment scenario, the possible interference created by the cells not contained in this radius is not taken into consideration in this analysis. The eNBs with cell-IDs 125, 120 and 190, given that they are not within a radius of 500 m from the capture site are thus not considered as interfering cells. Since the analysis deals with real network measurements, possible variations on the expected results can occur with the possibility of being aggravated by the imperfections of the measuring equipment.

For this reason, from the 30 capture files, a filtering was undertaken to gather the possible candidate files conveying the pretended results. The filtering alone is an indicator of the overall behavior of when considering a sparse deployment scenario, since it is expected that in this scenario a higher percentage of captures with constant radio channel conditions when compared to a dense deployed scenario.

The filtering of the different files aims to categorize the different behavior obtained when the model is applied to each capture. The categories are thus the following:

- **Category 1:** Constant Expected Throughput;
- **Category 2:** Optimal Throughput is greater than Expected Throughput;
- **Category 3:** Actual Optimal Throughput is greater than Actual Throughput.

The first category to analyze is whether the expected throughput remains constant along the evaluated LTE slots. By having a constant throughput, the reported CQI based on the average wideband SINR remains the same without suffering fluctuations, thus indicating steady channel conditions. The second analyzed category referred to assessing if the calculated optimal throughput based on individual MCS per resource block was greater than the expected throughput. The third and final category resulted from the filtering pertained to evaluate if the actual optimal throughput derived from the optimal throughput using the proposed scheme of adopting the MCS of the first demodulated LTE slot was greater than the actual throughput based on the expected throughput. The behavior of interest is for a file to belong in all three categories.

The first phase of the analysis went through all the capture files to determine the performance parameters and assess their behavior, focusing on the calculation of the performance parameters with received power being calculated as the average of the reference signals within each resource block. This analysis was undertaken for just the antenna port labelled L1_0. The nomenclature chosen for the different capture files refers to the date and time when the capture was executed, enabling to have a sense of continuity between the different files although there is still a gap between them. The name of the files thus assumes the structure MM_DD_hh_mm_ss.txt. The captures were performed on June 28th between 02:07:22 PM to 02:07:55 PM, which means that the only parameter that changed the name of the different files referred to the seconds value. One can thus differentiate the files according to the second it was taken the capture.

From the 30 captured files, 26 belong to Category 1 (86.7%), 1 to Category 2 (3%), and 9 to Category 3 (30%). The majority of the captured files are within Category 1 and Category 3, which overall indicates a small variation on the radio channel behavior and a potential performance gain for the proposed scheme. Eight files are within Categories 1 and 3, indicating that although there is a throughput gain for the proposed scheme over the actual measured throughput, by performing the average to calculate the received power per resource block, the full potential of using individual MCS is not yet achieved. The absolute results are shown in Annex D with a summary of this analysis being presented in Table 4.3.

Table 4.3 – Sparse Deployment Average Reference Signals Throughput Schemes Performance.

	File 38				File 40			
	μ	**σ**	**MAX**	**MIN**	**μ**	**σ**	**MAX**	**MIN**
$R_{b,s}^{opt}$ **[Mbit/s]**	5.86	0.14	6.10	5.41	5.81	0.16	6.26	5.37
$R_{b,s}^{\exp}$ **[Mbit/s]**	6.79	0	6.79	6.79	6.79	0	6.79	6.79
$R_{b,s}^{act}$ **[Mbit/s]**	5.23	0.24	5.63	4.48	5.15	0.26	5.90	4.41
$R_{b,s}^{act-opt}$ **[Mbit/s]**	5.53	0.20	5.90	4.88	5.42	0.27	6.26	4.77

An analysis of the overall performance of the actual optimal curve can be performed, to evaluate the throughput gain one obtains when considering multiple MCS per resource block compared to the actual throughput. The throughput gain of the actual optimal scheme in regard to the actual scheme can be seen in Figure 4.6 for each LTE slot.

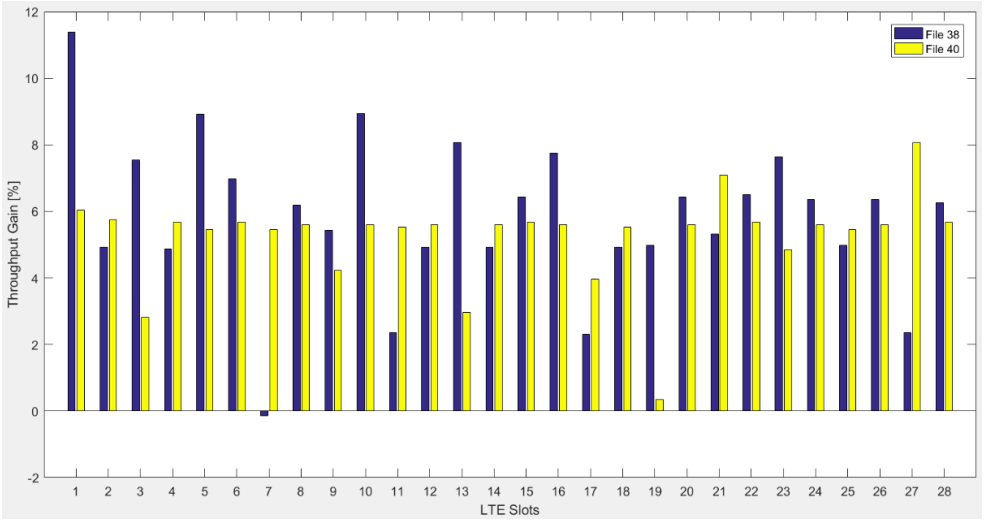

Figure 4.6 – Sparse Deployment Throughput Gain for Average Reference Signals.

The maximum throughput gain is observed on the 1st slot for File 38, with a value of approximately 0.60 Mbit/s representing an improvement of 11.4% over the actual throughput scheme. For File 40 the maximum throughput gain is 0.36 Mbit/s also for the 1st demodulated slot, being an improvement of 6.04%. The average throughput for the two files is 0.30 Mbit/s. The summary of throughput gain is presented in Table 4.4.

The observed throughput gain considering the average of the reference signals within each resource block indicates a good performance for the proposed scheme throughput in a sparse deployment scenario. The majority of files in Category 1 prove the steady channel conditions by having a constant expected throughput along the demodulated LTE slots.

The optimal throughput being lower than the expected throughput could be the result of performing the average of all the reference signals to calculate the received power per resource block.

Table 4.4 – Sparse Deployment Throughput Gain Results for Average Reference Signals.

	File 38				**File 40**			
	μ	**σ**	**MAX**	**MIN**	**μ**	**σ**	**MAX**	**MIN**
$R_{b,s}^{G}$ **[%]**	5.85	2.33	11.39	-0.14	5.24	1.39	8.08	0.34

The alternative method that was undertook to measure the received power per resource block resorted to individual reference signals within the resource block. By performing the average on all the reference signals, possible fluctuations on a single reference signal can originate the fluctuations on the measured optimal throughput causing the additional schemes to be affected as well. The received power per resource block is thus calculated based on the individual reference signals. The percentage of files that follow each category for a given reference signal are presented in Table 4.5. For the 30 capture files, the overall behavior of the throughput schemes improved, when considering this alternative method. There was a general increase of the percentage of files belonging to the three categories, when considering individual reference for the received power per resource block calculation.

Table 4.5 – Sparse Deployment Files Categorization for Individual Reference Signals.

Cell-Specific Reference Signal	Category 1	Category 2	Category 3
RS_1	53.3%	60.0%	50.0%
RS_2	53.3%	60.0%	53.3%
RS_3	63.3%	60.0%	56.7%
RS_4	63.3%	60.0%	56.7%
RS_5	30.0%	50.0%	56.7%
RS_6	43.3%	53.3%	63.3%
RS_7	66.7%	46.7%	53.3%
RS_8	60.0%	43.3%	56.7%

The percentage decrease of files belonging to Category 1 proves that there are fluctuations happening within the individual reference signals which, in turn, will affect the optimal throughput with individual MCS per resource block. For the remaining throughput schemes, a snow-ball effect is bound to happen given that both the proposed scheme actual optimal throughput and expected throughput are dependent to the optimal throughput, given that the actual throughput is obtained from the expected throughput.

The increase of files within Category 2 is also an indicator that for individual reference signals, the optimal throughput being lower than the expected throughput was the result of the fluctuations within the reference signals created by the different channel response on each reference signal. From the 30 captured files, 13 are inserted into the three categories for at least two reference signals. The files and reference signals are presented in Table 4.6.

Table 4.6 – Files in three categories for sparse deployment scenario.

File	Number of slots	Reference Signal
06_28_02_07_22.txt	20	RS_3, RS_4, RS_7, RS_8
06_28_02_07_23.txt	32	RS_1, RS_2, RS_3, RS_4, RS_7, RS_8
06_28_02_07_24.txt	18	RS_1, RS_2, RS_3, RS_4, RS_7, RS_8
06_28_02_07_25.txt	18	RS_1, RS_2, RS_3, RS_4
06_28_02_07_27.txt	26	RS_5, RS_6, RS_7, RS_8
06_28_02_07_29.txt	16	RS_1, RS_2, RS_3, RS_4
06_28_02_07_34.txt	26	RS_1, RS_2
06_28_02_07_37.txt	20	RS_5, RS_6, RS_7, RS_8
06_28_02_07_38.txt	28	RS_1, RS_2, RS_3, RS_4, RS_7
06_28_02_07_40.txt	28	RS_5, RS_6, RS_7, RS_8
06_28_02_07_43.txt	18	RS_5, RS_6, RS_7
06_28_02_07_51.txt	26	RS_3, RS_4, RS_7, RS_8
06_28_02_07_54.txt	18	RS_1, RS_2, RS_3, RS_4, RS_7, RS_8

The maximum number of reference signals that are constant throughout the captured LTE slots is 6, indicating that just by two reference signals not being entirely constant can affect the received power when performing the average of the reference signals.

For the files with less than 20 demodulated slots, the synchronization procedure was only able to find the correlation maximum between the received signal and the synchronization signals, PSS and SSS, at about half of the collected samples. This leads to obtaining frame synchronization only for a reduced number of slots, nonetheless, for the files with reduced number of slots there is still a constant behavior in terms of the throughput schemes. The file with the most demodulated slots occurred at the 23rd second of the measuring interval, with 32 demodulated slots. For this file, an in-depth study was performed to conclude which reference signal had the best performance.

For the file referring to the 23rd second capture, being the one with most demodulated slots and consistent behavior for six reference signals. For the fifth and sixth reference signals, given the variation of the expected throughput, not behaving in a constant way during the entire demodulated slots, its results were thus not considered to analyze the performance of the proposed scheme. The variation of the expected throughput simply means that the optimal throughput has suffered a drastic decrease, reducing the average SINR measured for a slot to decrease leading to the secondary node reporting a lower CQI index. Given that the analysis is being done by only evaluating the evolution of the throughput curves, disregarding the reporting timing, the occurrence of a variation merely indicates that there would be an additional signaling overhead to perform link adaptation.

For the six reference signals considered approvable for the analysis of the proposed scheme throughput, a summary is presented in Table 4.7 given that the absolute results along slots is located in Annex D.

Table 4.7 – Sparse Deployment Individual Reference Signals Results.

	RS_7				**RS_8**			
	μ	**σ**	**MAX**	**MIN**	**μ**	**σ**	**MAX**	**MIN**
$R_{b,s}^{opt}$ **[Mbit/s]**	7.76	0.42	8.74	7.00	7.74	0.43	8.74	7.00
$R_{b,s}^{\exp}$ **[Mbit/s]**	6.79	0	6.79	6.79	6.79	0	6.79	6.79
$R_{b,s}^{act}$ **[Mbit/s]**	5.09	0.35	5.63	4.21	5.09	0.34	5.63	4.21
$R_{b,s}^{act-opt}$ **[Mbit/s]**	5.61	0.67	8.27	4.64	5.59	0.66	8.23	4.60

The results for the throughput gain from the actual optimal throughput to the actual throughput are presented in Figure 4.7. One can see that for the first four reference signals, the throughput gain oscillates between being a negative and a positive gain.

For the first slot, the actual optimal throughput takes the value of the optimal throughput as it is from the first demodulated slot that the MCS are chosen for the preceding slots, thus the greater throughput gain observed in this slot. The throughput gain behavior for the first reference signals alternates between being negative and positive.

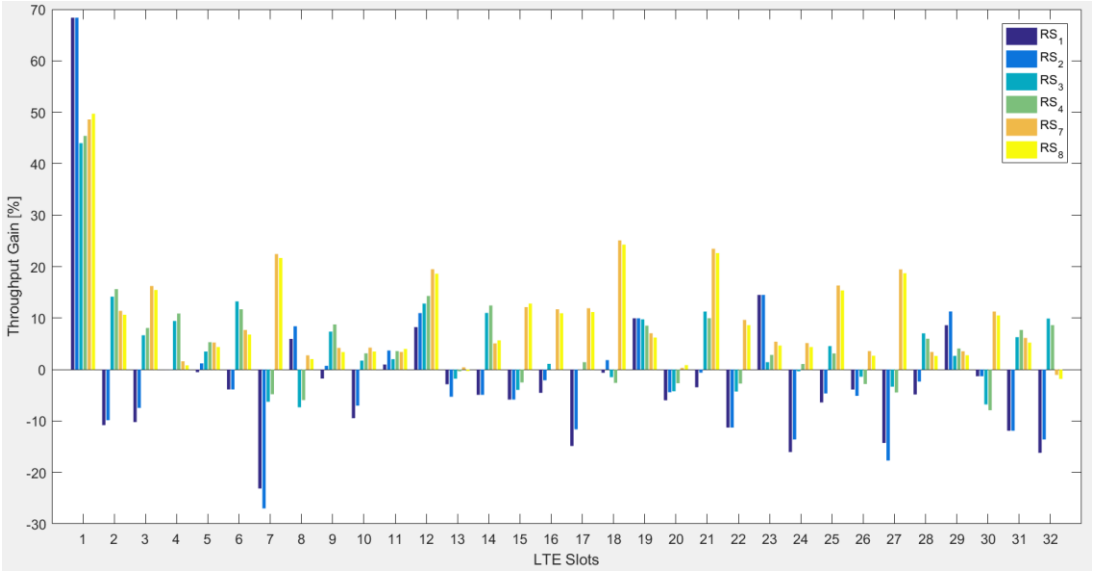

Figure 4.7 – Sparse Deployment Throughput gain per slot for individual Reference Signals.

For the first two reference signals the additional overhead does compensate the adoption of the proposed scheme as it even conveys a loss on the throughput which is achieved. Focusing on the third, fourth, seventh and eighth reference signal the proposed scheme assumes a far more consistent behavior, with the actual optimal throughput being greater than the actual throughput on most LTE slots. The throughput gain summary for each reference signal is presented in Table 4.8.

Table 4.8 – Sparse Deployment Individual Reference Signal Proposed Scheme Performance.

		RS_1	**RS_2**	**RS_3**	**RS_4**	**RS_7**	**RS_8**
$R_{b,s}^{G}$ **[%]**	**μ**	-2.26	-1.27	4.33	4.87	10.23	9.66
	σ	15.33	15.52	9.59	9.69	10.02	10.18
	MAX	68.37	68.37	43.99	45.40	48.61	49.71
	MIN	-23.11	-26.99	-7.33	-7.92	-1.05	-1.83

To improve the performance of the proposed scheme, while still considering the individual reference signals for received power calculation, is the use of antenna diversity. Two antenna arrays are thus considered:

- **Array 1:** Ports L1_0, L1_1, L1_2, L1_3, R1_0, R1_1, R1_2 and R1_3;
- **Array 2:** Ports L2_0, L2_1, L2_2, L2_3, R2_0, R2_1, R2_2 and R2_3.

The throughput gain is evaluated for the two arrays, when the diversity combining and MIMO techniques are performed. Regarding MIMO, as the capacity is limited by the number of antennas at the transmitter, the sets of 8 antennas of the last two arrays are used to mimic two antennas at the receiver side, thus achieving 2x2 MIMO. A key parameter usage of multiple antenna enhancement techniques, other than the spacing between the antennas, is the synchronization between the multiple elements. The synchronization is assured with the implemented mechanism in the DMA Method during the data acquisition, triggering the data acquisition for all the sides of the MegaBEE at the same time. Although

the mechanism was implemented and tested via simulations to assess its functionality, the files collected for the sparse deployment scenario only had one fully synchronized capture for the 16 antenna ports.

The mentioned file corresponds to the 23rd second of the measuring interval, providing the need of an evaluation of the proposed scheme performance considering the two multiple antenna enhancement techniques under study. By using multiple antennas, there is also the risk that the channel conditions in each element is exceedingly distinct. Given that the combining diversity chooses the RBs with the highest SINR in each slot, if a single antenna measures a highest SINR than the rest of the array, then the signal being outputted at the diversity combiner will consist of the single antenna.

This performance also applies to fluctuations in the expected throughput being measured for the different antennas and, in particular, for the different reference signals being used to calculate the received power per resource block. For the referred capture file, the reference signals that match the three categories used to evaluate the proposed scheme are the first three reference signals. For the remaining reference signals, the introduced fluctuations by the different channel conditions on the multiple antennas on the expected throughput cancels out the possible improvement done by the proposed scheme.

In regard to Array 1 the evolution of the throughput gain can be observed in Figure 4.8 for each considered reference signal. The third reference signal conveyed the best performance in terms of the proposed scheme, as the actual optimal throughput is always superior than the actual throughput. For the obtained throughput gain, one can see the general performance improvement for the diversity combining.

In Figure 4.9, the focus changes to Array 2, where the performance is similar to the one observed in the Array 1. The performance of the proposed scheme is consistent, being fairly identical to the one observed in Array 1, also experiencing a negative throughput gain in some of the demodulated LTE slots. Evaluating the arrays individually, one sees that for Array 1 the throughput gain is higher for the considered reference signals when compared to the results in Array 2. In both arrays, the reference signal RS_3 is the only one experiencing only positive gains.

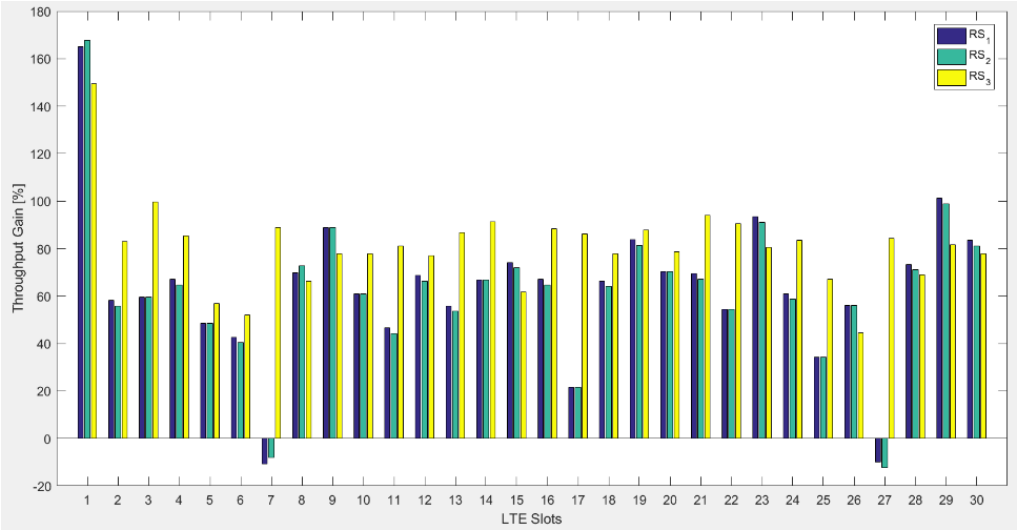

Figure 4.8 – Sparse Deployment Throughput Gain per Reference Signal for Array 1.

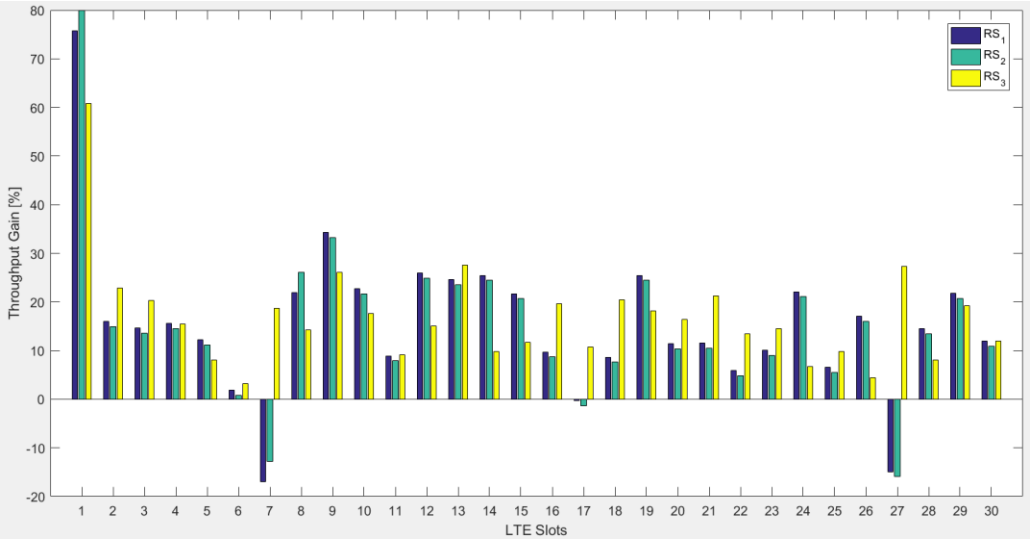

Figure 4.9 – Sparse Deployment Throughput Gain per Reference Signal for Array 2.

In terms of the MIMO results, from Figure 4.10 one observes that the throughput gain is not as high relative to Array 1. This is explained by the fact that the by the optimal throughput being the result of the sum rate of the two arrays with MIMO, the expected throughput will increase as well as the actual throughput. As the channel conditions for the evaluated reference signals are resembling in all antenna ports, the obtained results match the expected in a typical 2x2 MIMO configuration, with an increase of the capacity by the order of the minimum number of antennas employed at the receiver or transmitter.

Considering diversity, the throughput curves absolute values are presented in Annex D. In terms of the throughput gain for each array, the maximum value is obtained for the first slot, when the actual throughput is equal to the optimal throughput. Due to the optimal throughput employing individual MCS for each resource block, it is highly greater than the actual throughput explaining the high percentage gain which is observed. The summary of the average, standard deviation, maximum and minimum throughput gain are presented in Table 4.9, for the two considered arrays and MIMO.

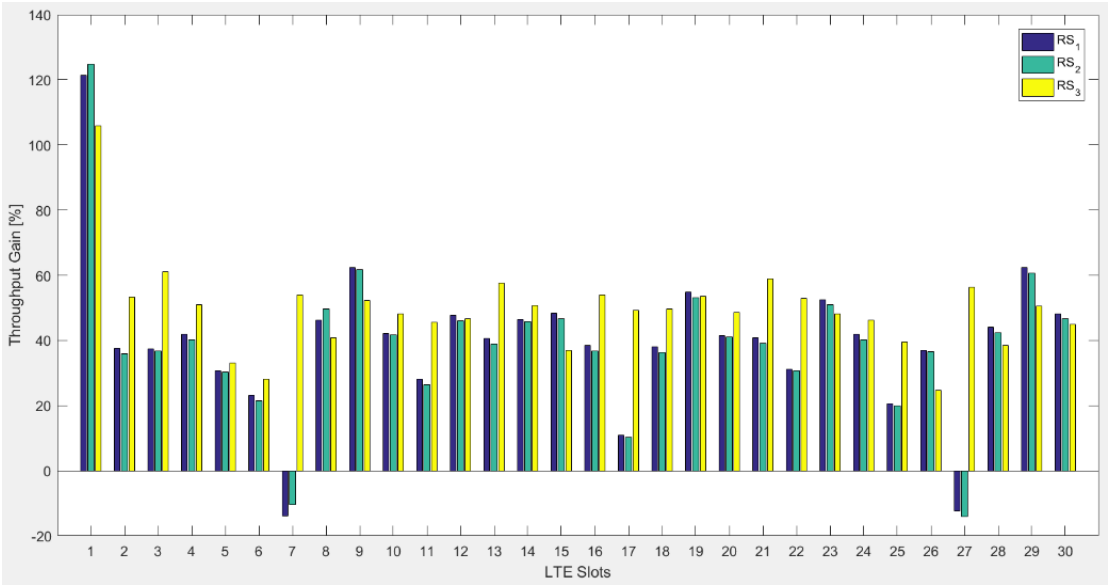

Figure 4.10 – Sparse Deployment Throughput Gain per Reference Signal for MIMO.

Table 4.9 – Sparse Deployment Throughput Gain results for Diversity Combining.

		Array 1			Array 2			MIMO		
		RS_1	RS_2	RS_3	RS_1	RS_2	RS_3	RS_1	RS_2	RS_3
$R_{b,s}^{G_{div}}$ [%]	**μ**	62.92	61.87	80.90	15.53	15.02	16.75	39.65	38.86	49.35
	σ	31.73	31.80	18.01	15.96	16.42	10.52	23.32	23.57	13.73
	MAX	165.02	167.77	149.57	75.70	79.95	60.77	121.27	124.76	105.85
	MIN	-10.75	-12.34	44.56	-16.98	-15.94	3.18	-13.82	-14.09	24.70

4.2.2 Scheduling Algorithms Performance

The implemented scheduling algorithms are frequency selective, thus the resource allocation for the secondary nodes can be made both on time and frequency. To fully exploit the frequency selectivity of the scheduling algorithms, the wideband CQI reporting cannot be considered. Since a single CQI is reported for the whole band and thus the scheduling algorithm would only allocate users in time as the total bandwidth is allocated to a single user.

To compare the improvements of the proposed scheme, a sub-band reporting is considered where the secondary node reports the average CQI for *k*-sized sub-bands. The sub-band size *k* in resource blocks, for a bandwidth of 20 MHz, is 8 resource blocks [3GPP17b], thus comprising 12 sub-bands within the whole LTE bandwidth. By dividing the whole bandwidth of 100 resource blocks in 12 sub-bands of 8 resource blocks, one is left with 4 resource blocks. For this analysis, the 4 resource blocks not considered to calculate the average CQI nor for secondary node scheduling are the two initial and last resource blocks in a slot.

For a Two-Tier Cellular Network, the number of secondary nodes can be assumed as being smaller than a regular UE, meaning that for this analysis a maximum number of five secondary nodes are considered for the three scheduling algorithms. Given that the static captures occurred at the same location, to mimic the different behavior of the secondary nodes the method used to determine the CQI for both the proposed scheme and sub-band scheme is varied.

The first secondary node, with the worst channel conditions, performs the calculation of the received power per resource block from the average of the reference signals, being the 27th second capture of the measuring interval in the sparse deployment scenario. Three secondary nodes with similar channel conditions make use of the individual reference signals for received power calculation per resource block, corresponding to the 22nd, 34th and 38th second of the measuring interval for RS_7, RS_2 and RS_3 respectively. The final secondary node with best channel conditions consists of the 23rd second File, employing MIMO with two antenna arrays of eight antennas. For the three scheduling algorithms, the total cell throughput along slots in addition to individual secondary throughput are shown in Annex D.

The properties of this algorithm can be parametrized by the means of its fairness and overall cell throughput. A comparison of the two evaluated schemes can be found in Figure 4.11 for the two referred parameters. In terms of fairness, the proposed scheme's performance exceeds the sub-band scheme

in all the studied slots. This can be explained by how the resources are allocated in the two schemes. For the proposed scheme, since the allocation is done on the resource block level the probability of a secondary node to be allocated a lower SINR resource block is higher than when one allocates an entire sub-band composed of 8 resource blocks as the channel conditions are averaged out on this sub-band.

In terms of the overall cell throughput, the proposed scheme also exceeds the average sub-band one, again due to consistent behavior of consecutive slots which overall improve the throughput of the proposed scheme, while the average sub-band scheme considers only a MCS for an entire sub-band reducing the maximum throughput achievable.

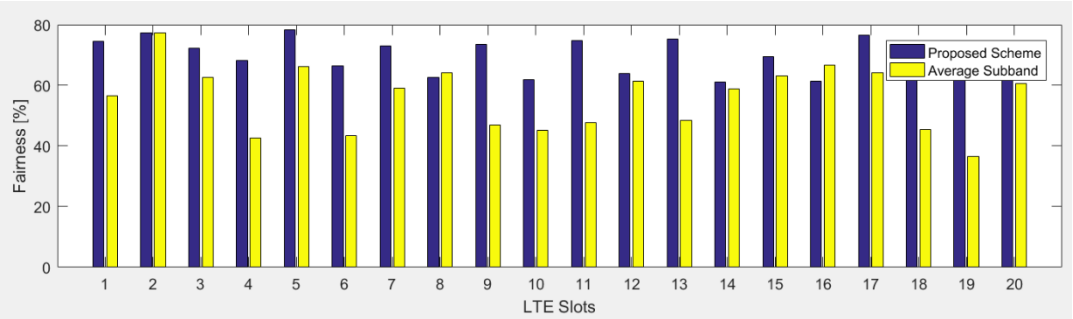

(a) Round Robin Fairness.

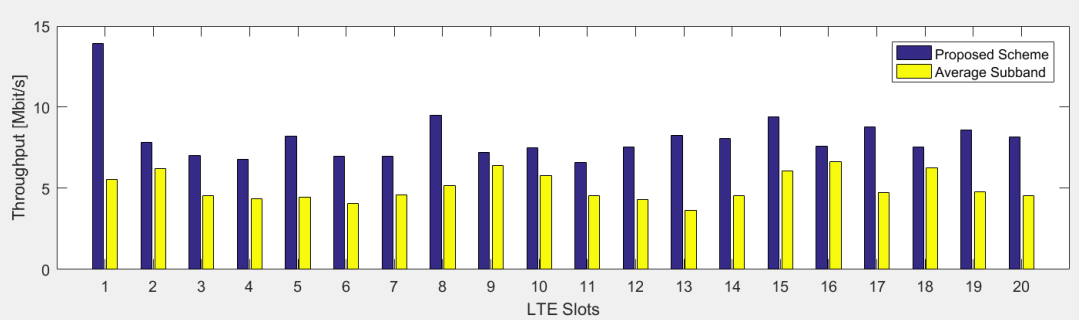

(b) Round Robin Total Cell Throughput.

Figure 4.11 – Round Robin Schemes Comparison.

Nonetheless, one sees that for the proposed scheme, the performance of the Best CQI algorithm is fairer than the average sub-band one, not suffocating the allocated resources to a single secondary. One can also observe that the overall cell throughput is also higher in each slot for the proposed scheme. In Figure 4.12 the two schemes are again compared in terms of fairness and total cell throughput per slot.

Similar to the Round-Robin algorithm, the proposed scheme has a better performance in the two parameters than the average sub-band scheme. Although the performance shares the same improvements as the previous algorithm, in terms of fairness in general has decreases mainly due to the overallocation of a single secondary with the best channel conditions. As the overallocation is more severe in average sub-band scheme, the fairness per slot is also lower than the proposed scheme. The total cell throughput is also greater in this algorithm for the two schemes, reaching twice the throughput value experienced in the previous scheduling algorithm in some of evaluated slots.

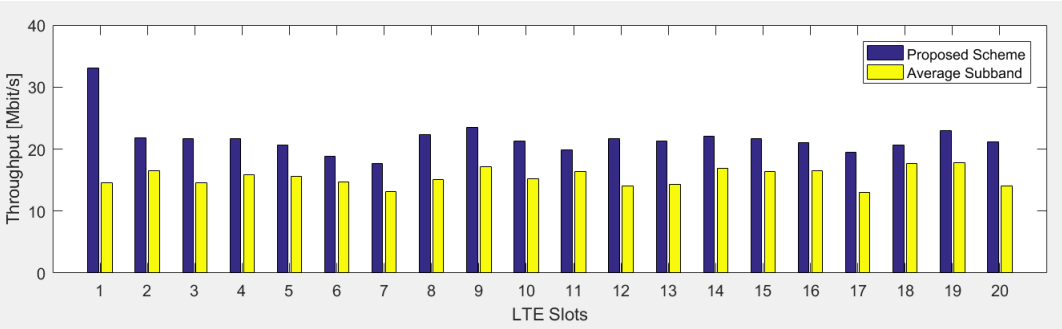

(a) Best CQI Fairness.

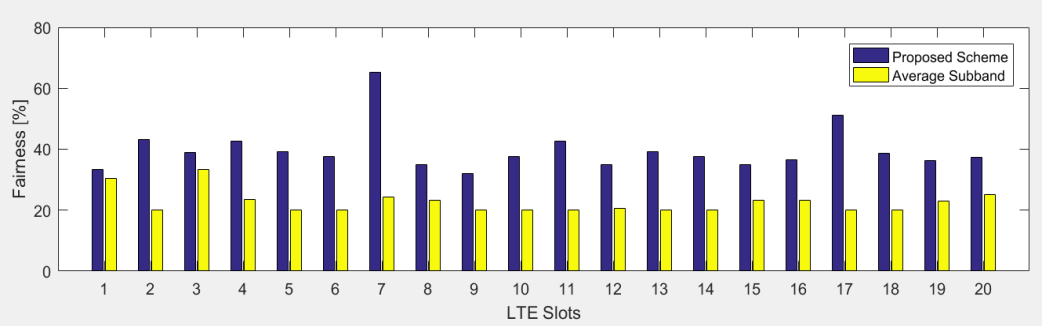

(b) Best CQI Total Cell Throughput.

Figure 4.12 – Best CQI Schemes Comparison.

The final algorithm to be evaluated is the Proportional Fair one,

Figure 4.13. The main limitation on the analysis of this algorithm in the studied framework is in terms of the available LTE slots. Given that the fairness behavior is only observed after a long number of consecutive slots, the fairness results may indicate a seemingly random behavior, originated simply because the algorithm has not stabilized for the number of slots in question.

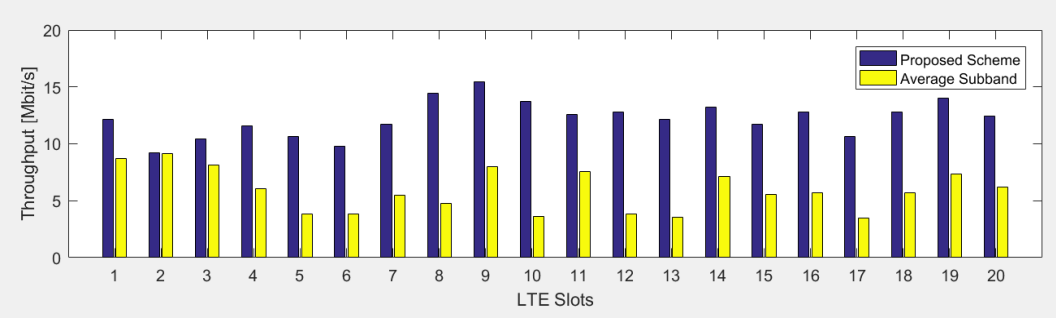

(a) Proportional Fair Fairness.

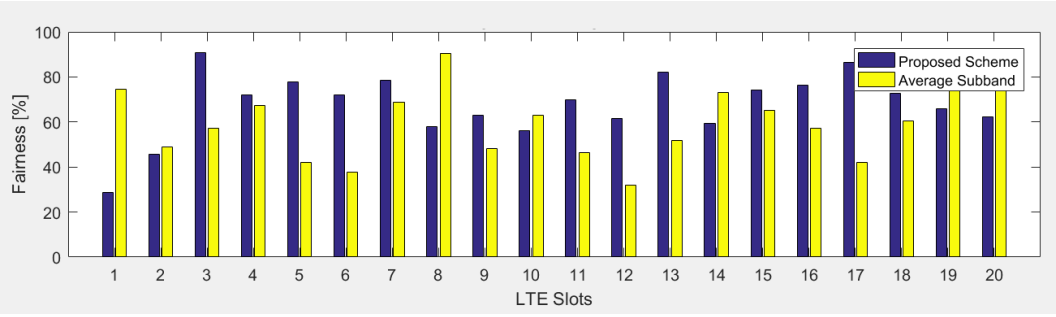

(b) Proportional Fair Total Cell Throughput.

Figure 4.13 – Proportional Fair Schemes Comparison.

As observed in

Figure 4.13, contrary to the previous two algorithms, the level of fairness in the proposed scheme is not always greater than the average sub-band scheme. Again, this behavior can be explained by the reduced number of LTE slots being evaluated, not allowing the Proportional Fair algorithm to reach stability and yield the fairness results it is known for after a long number of consecutive LTE slots. For the second metric under study, the Proportional Fair algorithm assumes the same behavior as the previous scheduling algorithms, with total cell throughput being always great in the proposed scheme than in the average sub-band scheme.

A summary of the improvements on both metrics for the two schemes being evaluated and the three algorithms under test can be found in Table 4.10.

Table 4.10 – Fairness Improvement and Total Cell Throughput Gain.

		Round Robin	Best CQI	Proportional Fair
Fairness Improvement [%]	**μ**	28.91	80.19	24.13
	σ	26.22	40.13	47.34
	MAX	81.18	169.89	104.95
	MIN	-8.15	8.83	-61.72
Total Cell Throughput Gain [%]	**μ**	63.96	41.15	128.52
	σ	35.81	22.80	75.00
	MAX	151.64	127.17	281.88
	MIN	12.54	16.65	1.30

4.3 Dense Deployment Scenario

In this section the performance impact of the proposed scheme is evaluated for a dense deployment scenario. The only difference from this scenario and the previous studied reference scenario is in terms of cell density within a radius of 500 m, since the rest of the measurements setup remains unchanged. While the sparse deployment scenario only considered two interfering cells, as their deployment site was within 500 m of the DMA capture, in this scenario four cells are assumed as interferers. The location of this scenario is presented in Figure 4.14 in Hoskin Avenue near Queen's Park, for a static secondary node synchronized to the eNB with the cell-ID 113 colored in turquoise. One can also see the interfering cells with the cell-IDs 400, 457, 121 and 120.

A total of 21 DMA captures were performed on June 28th between 02:10:29 PM and 02:10:53 PM. To evaluate the impact of the deployment of a secondary node within a dense deployment scenario, the same set of tests done for the sparse one were performed. In general, the expected results are a lower

secondary node throughput due to the large number of interfering cells, presenting however throughput peaks due to the proximity of the secondary node to the synchronized cell. These factors contribute to an increase of radio channel variations, creating fluctuations on the expected throughput scheme.

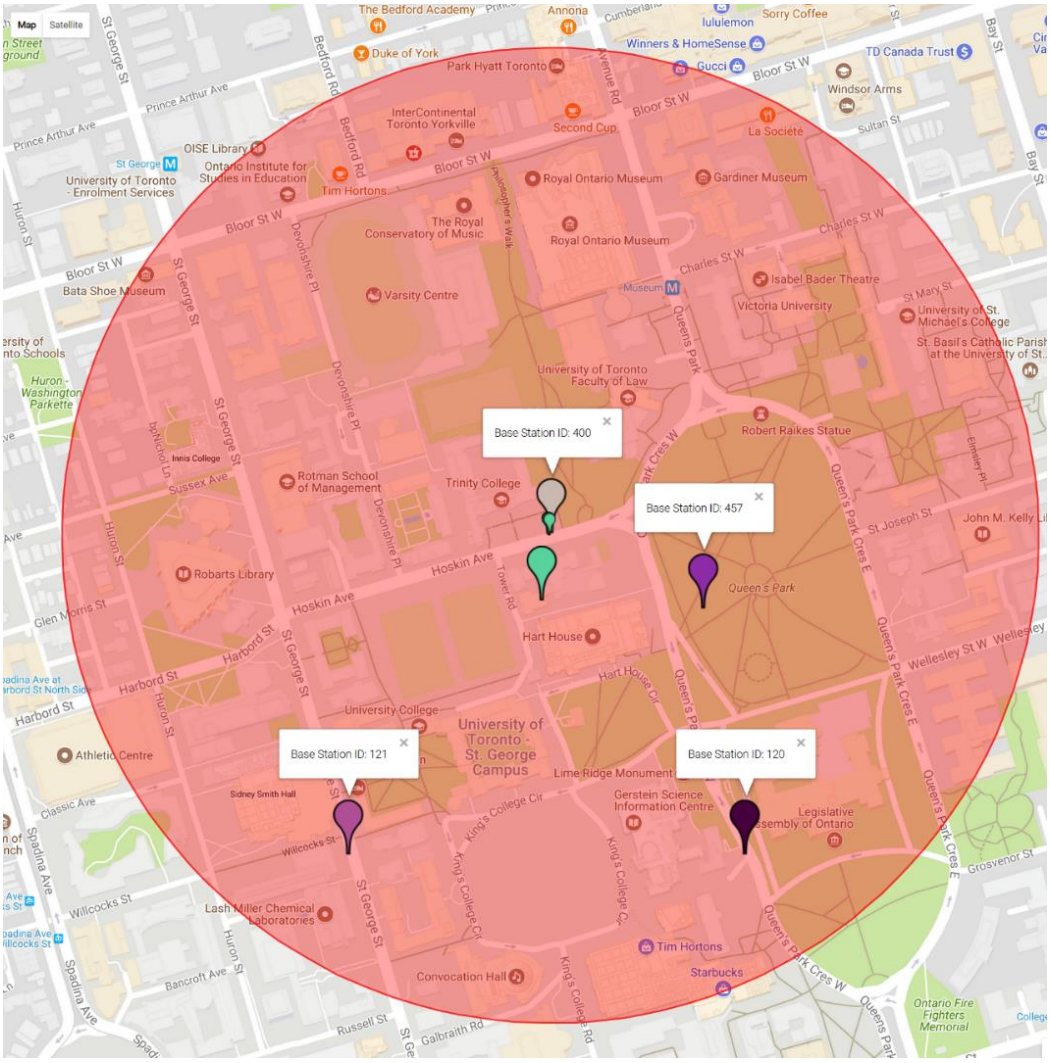

Figure 4.14 – Dense Deployment Scenario.

The first set of tests is to evaluate the behavior of the performance parameters for a received power calculation based on the average of the reference signals within the resource block. After this initial step the individual reference signals for received power calculation are analyzed.

Following the same three categories, from the 21 files, no captures had a constant expected throughput, with all of the captures suffering fluctuations along the demodulated LTE slots. As there is no file with the first category under evaluation, this trend changes when one moves to the second category.

The total number of captures in the measured interval have a greater optimal throughput based on individual MCS per resource block than the expected throughput, even with the added fluctuations in this scenario. For the third and final category, only eight files presented a higher proposed scheme actual optimal throughput than the actual throughput based on the expected scheme, a trend that was already observed in the sparse deployment scenario.

The minimum number of fluctuations considering the average of the reference signals had the duration of a LTE slot, happening in files corresponding to the 42nd and 49th second capture with 16 and 18 demodulated slots respectively.

The following step of the evaluation is to consider individual reference signals for receiver power calculation. Similar to the sparse deployment scenario the categorization can be seen in Table 4.11. In comparison with the sparse deployment, the number of files within the first category decreased severely, indicating the fluctuating behavior of the expected throughput. Due to the constant update of the MCS after each fluctuation, the trend of the proposed scheme actual throughput is to match the optimal throughput. The increase of the optimal throughput over the expected throughput can also be explained from the variation of the expected throughput.

Table 4.11 – Dense Deployment Files Categorization for Individual Reference Signals.

Cell-Specific Reference Signal	Category 1	Category 2	Category 3
RS_1	0%	100%	61.9%
RS_2	0%	100%	66.7%
RS_3	4.8%	100%	85.7%
RS_4	4.8%	100%	81.0%
RS_5	0%	100%	23.8%
RS_6	0%	100%	38.1%
RS_7	4.8%	100%	33.3%
RS_8	14.3%	100%	38.1%

Only four files are within the three categories in the captures performed in this scenario being presented in Table 4.12. An analysis on the file corresponding to the 30th second capture of the measuring interval, given that it follows the three categories in two reference signals and has the highest number of demodulated slots tied with the 45th second capture.

Table 4.12 – Files in three categories for dense deployment scenario.

File	Number of slots	Reference Signal
06_28_02_10_30.txt	24	RS_7, RS_8
06_28_02_10_42.txt	16	RS_8
06_28_02_10_45.txt	24	RS_8
06_28_02_10_49.txt	18	RS_3, RS_4

A summary of the obtained curves for the dense deployment scenario can be found in Table 4.13 for each considered reference signal, with the absolute results being located in Annex D.

In terms of throughput gain, from Figure 4.15 one sees that although the throughput curves have

suffered a general increase in all slots, the throughput gain remains fairly similar to the one observed in the sparse deployment scenario. This promotes the notion that the proposed scheme is scenario independent in terms of the throughput gains, when steady channel conditions are verified.

Table 4.13 – Dense Deployment Throughput Curves Performance for Individual Reference Signals.

	RS$_7$				**RS$_8$**			
	μ	**σ**	**MAX**	**MIN**	**μ**	**σ**	**MAX**	**MIN**
$R_{b,s}^{opt}$ **[Mbit/s]**	5.03	0.31	5.76	4.52	4.96	0.28	5.57	4.48
$R_{b,s}^{\exp}$ **[Mbit/s]**	2.74	0	2.74	2.74	2.74	0	2.74	2.74
$R_{b,s}^{act}$ **[Mbit/s]**	2.29	0.07	2.39	2.17	2.29	0.07	2.39	2.17
$R_{b,s}^{act-opt}$ **[Mbit/s]**	3.77	0.39	5.17	3.26	3.74	0.38	5.13	3.22

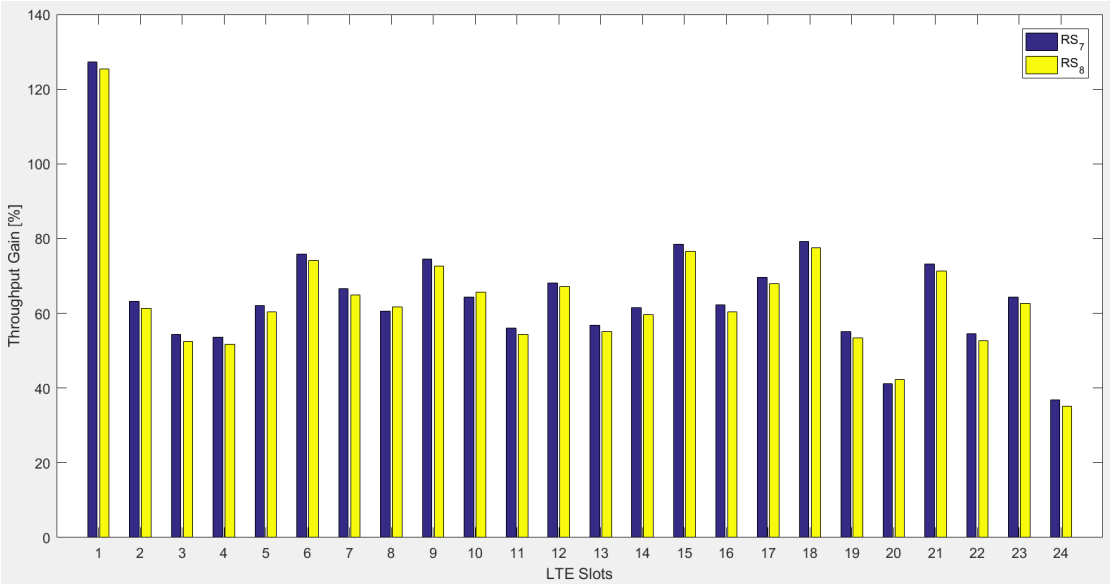

Figure 4.15 – Dense Deployment Throughput Gain for Individual Reference Signals.

The summary of the throughput gain results is presented in Table 4.14.

Table 4.14 – Dense Deployment Throughput Gain Results for Dense Deployment.

	RS$_7$				**RS$_8$**			
	μ	**σ**	**MAX**	**MIN**	**μ**	**σ**	**MAX**	**MIN**
$R_{b,s}^{G}$ **[%]**	64.98	16.91	127.23	36.80	63.60	16.73	125.45	35.10

Chapter 5

Conclusions

This chapter details the main conclusions of the thesis with a main summary of all the chapters composing it. It finishes by providing suggestions for framework improvement and future work to enhance the obtained results.

The objective of this work was to develop a model to optimize the link between the primary and secondary nodes of a Two-Tier Cellular Network. The optimization is in terms of throughput/capacity by performing Link Adaptation/Adaptive Modulation and Coding considering multiple Modulation Coding Schemes for individual PRBs within a slot. The secondary node was implemented in hardware using the MegaBEE prototyping platform for data acquisition purposes, and software in MATLAB to perform the demodulation and radio channel characterization. The operations of link adaptation and throughput calculation were all done in software also in MATLAB, mimicking the behavior of a eNB.

In the first chapter, an overview of the past mobile communications systems is presented along with the evolution of each standard and the overall traffic trends for the current mobile communication system and for future generations. The motivation regarding the use of a Two-Tier Cellular Network in replacement of a regular one tier cellular network, in terms of the advantages of a secondary node when compared to a regular user equipment.

Regarding the second chapter, the fundamental concepts are studied presenting the basic concepts prior to the development of the model. The beginning of the chapter contains an in-depth study of LTE-A in terms of this system's architecture and its evolution from the previous mobile communications systems generations, explaining in detail each component and interface that compose the architecture. In the same section, LTE-A's radio interface is evaluated in terms of the multiple access techniques both in DL and UL, the supported bandwidths and the more important physical channels for this thesis, with an overview of the recent technologies introduced in LTE-A such as Carrier Aggregation and Coordinated Multipoint. The following section encompasses the multiple antenna enhancement techniques available in LTE-A. The main technology under study in this section is spatial multiplexing used in MIMO providing an outline of the future application of Massive MIMO. The second technique under study in this section is beamforming, a technique that allows the generation of a more directive beam by controlling the phase and magnitude of the multiple antenna elements in the array. The general aspects of the Two-Tier Cellular Networks are then approached in what concerns its main advantages compared to a regular UE in terms of computational power and the mitigation of space constraints to deploy multiple antennas. Its main drawbacks in terms of interference and mobility are also evaluated, with addition of the current backhaul solutions used in this type of networks. Given the advantages of Two-Tier Cellular Networks, the main services and applications are then studied to foresee the practical aspects one gains in this extent when considering the deployment of multiple secondary nodes over a main primary node. The state of the art works related to Two-Tier Cellular Networks optimization finalize this chapter.

After the fundamental concepts are introduced and properly studied, the model development ensues in the third chapter. In this chapter, the solutions for the optimization of the link between the primary and secondary node are fully described, implemented and assessed, showing also the main performance parameters used in this analysis. The start of this chapter refers to the model description, providing an overview of the main modules composing the model. It follows with the secondary node development, the performance parameters determination, finalizing the chapter with the model implementation and assessment. The performance parameters are mainly in terms of throughput determination based on a

proposed scheme using individual MCS per resource block and the expected scheme throughput based on an average MCS for the whole bandwidth or sub-bands. As the analysis aims to prove the validity of the proposed scheme and its improvements over the expected scheme two types of analysis are performed. The first analysis relates to the throughput gain when one performs the proposed scheme, and the second analysis is in terms of the improvements evaluation when one applies three different scheduling algorithms. In both analysis, the comparison is always done in terms of the improvements one obtains when using the proposed scheme over the expected scheme.

The model can thus be divided in two modules in what concerns which node in a Two-Tier Cellular Network performs a given operation. The first module refers to the secondary node operations, being that the second module relates to the primary node operations. The secondary node in this thesis is interpreted as a regular UE, with the main difference being the possibility of using multiple antennas in its deployment. The development of this module is done in a first phase in hardware and on a second phase in software.

The first phase comprises the overview of the hardware platform used for the receiver of the secondary node and the method description for the data acquisition procedure. Three methods are considered for data acquisition, with each method being given the name of the main block used in its implementation. Regarding the first method, with the name of BRAM method, it consists of a simple storing system for the captured samples in the MegaBEE transceiver, using the Xilinx Shared BRAMs available in hardware. Multiple BRAMs can be used to increase the number of stored samples, providing the need of the implementation of a demultiplexing mechanism to select the BRAM to fill with the received data. The second method makes use of the Direct Memory Access following the AXI-4Stream protocol to transfer huge amounts of data between the programmable logic to the processing system of the MegaBEE. In this method, a multiplexing system was needed in order to control the flow of data to be transferred as control flags based on a reference counter were implemented. Aside from the reference counter, by using the GPS within the MegaBEE, the coordinates are also stored in the transferred data. The third and final method consisted on a UDP stream over a 10 GbE connection using the SFP+ outputs of the MegaBEE. Allowing the usage of up to eight antennas perf MegaBEE by using two 10 GbE connections, this method provided a continuous acquisition capture system with a variable capture length. The data to be streamed would then be divided in UDP packets, with the addition of a frame to control the transferred data.

The second phase of the secondary node development referred to the captured radio channel characterization, in terms of cell synchronization and LTE demodulation. The main output of this procedure is not only the physical cell-id of the cell the secondary node is synchronized to, but also a demodulated grid in terms of subcarriers and OFDM symbols, enabling the easy indexing of the several resource elements composing the received signal. After these two parameters are obtained the received power per resource block can be calculated based on the reference signals within the resource block which depend on the physical cell-id of the synchronized cell. Knowing the interfering cell-ids, one can also determine the interference power by performing the same set of operations as the synchronized cell received power. From the received power per resource block one can determine the average

received power within a slot, being given by the mean of the received power of all the resource blocks within the slot. These two received power values are the foundation of the proposed and expected throughput schemes. The proposed scheme is based on individual MCS per resource block thus the SINR measuring and CQI reporting is based on a resource block level. On the other hand, the expected scheme performs its SINR measuring and CQI reporting based on a wideband level.

Regarding the second module of the model, its operations are determined by the primary node. The primary node functions in this model is not only to determine the MCS based on the CQI reported by the secondary node, but also as a scheduler for the multiple secondary nodes within a Two-Tier Cellular Network. In what concerns the proposed and expected scheme, the primary node performs the conversion from the reported CQI to the throughput measured slot by slot. From the CQI reports, the primary node performs the resource block scheduling using three frequency selective scheduling algorithms, Round Robin, Best CQI and Proportional Fair. The comparison from the proposed and expected scheme for the scheduling procedure is performed based on the overall cell throughput per slot and the fairness along slots experienced for the two schemes.

After the model is implemented and its assessment is completed, one will test it on two different scenarios. The scenarios description entails the fourth chapter, also providing an explanation of the several assumptions taken for the measurements. In this first section, the two scenarios are built based on a preliminary synchronization run with the objective of establishing a map of the several cells around the measurements location. This location is the city of Toronto in Canada, in particular the St. George Campus of University of Toronto and its surrounding streets. The synchronization run consisted of acquiring several captures using the implemented data acquisition methods, performing the synchronization algorithm to determine for each capture which was the synchronized cell. Parallel to the run, several records of the cell information were collected using the embedded application Test Field Menu on a Iphone cell phone. These two procedures allowed the mapping of the eNBs overlaid in the measuring environment and to evaluate the type of deployment used in this part of Toronto. The reference scenario pertained to a static secondary node in a sparse deployment, being that a second scenario was built based on this one but considering a dense deployment. The calibration of MegaBEE as well as the whole equipment setup and the type of analysis remained equal in both scenarios.

Three categories were defined to evaluate the correct functionality of the proposed scheme. The first category pertained to a constant expected throughput, while the second and third categories evaluate if the proposed scheme optimal and actual optimal throughput were greater than the respective expected scheme throughputs. The main results on the reference scenario of a sparse deployment reveal a significant improvement of the proposed scheme compared to the expected scheme. The first analysis aimed to evaluate the behavior of the throughput schemes when the received power per resource block was determined based on the average of the reference signals within each resource block. On this scenario, no capture file followed the three defined categories, although the majority had a constant expected throughput proving the channel steady behavior. For the two evaluated capture files, the proposed scheme optimal throughput was always lower than the expected throughput, a behavior that can be explained by the variations within each reference signal. In terms of the throughput gain, for the

two files one obtained an average improvement of 5.85% and 5.24% and a maximum improvement of 11.39% and 8.08% respectively, even though the optimal throughput had not reached higher values than the expected throughput.

When considering individual reference signals, this trend changes as 43% of the capture files were within the three categories at the same time, for at least one reference signal. For the file with the most demodulated slots, the average and maximum throughput gain over the expected scheme was of 10.23% and 48.61% for RS_7 with an average and maximum improvement of 9.66% and 49.71% for RS_8. To improve the performance gains, the usage multiple antennas was considered. One defined two arrays of eight equally spaced antennas to evaluate the improvement when using diversity and 2x2 MIMO with the two antennas at the receiver being the two arrays. For the reference signal with the best performance, RS_3, one obtained an average and maximum throughput gain of 80.90% and 149.57% for the first array, whereas the second array had and average and maximum of 16.75% max 60.77% respectively. Considering MIMO, as the two arrays had two different performance gains, the obtained results were an average throughput gain of 49.35% and a maximum value of 105.85%, although when using MIMO the throughput increased to approximately twice of the value obtained for the two individual arrays.

For the same scenario, three scheduling algorithms were tested for capture files with different channel conditions, considering the allocation of individual resource blocks for the proposed scheme and sub-bands to the expected scheme. One defined a maximum number of five secondary nodes deployed in the Two-Tier Cellular Network. The secondary node with the worst channel conditions performed the received power calculation based on the average of the reference signals, while three other secondary nodes performed the same calculation but considering individual reference signals. Finally, the secondary node with the best channel conditions considered individual reference signals for received power calculation and also the usage of 2x2 MIMO with two arrays of eight antennas. The performance improvement evaluation was based on the fairness and overall cell throughput. For the Round Robin algorithm, the improvements of the two parameters had an average value of 28.91% for fairness and 63.96% for the cell throughput. The Best CQI algorithm had a fairness improvement 80.19% and overall cell throughput gain of 41.15%, whereas the Proportional Fair algorithm had the values of 24.13% and 128.52% respectively. One concludes that the individual resource block scheduling shows a great improvement over the allocation of sub-bands in both fairness and overall cell throughput for the three scheduling algorithms.

Proceeding to next evaluated scenario in a dense deployment zone, the number of files within the three categories reduced severely considering both average and individual reference signals for received power calculation. Similar to the sparse deployment scenario, no file respected the three categories in the dense deployment scenario, although in the latter this behavior is aggravated due to no file being within the first category of constant expected throughput. Considering individual reference signals, 19% of the capture files were within the three categories for at least one reference signal, decreasing when compared to the sparse deployment scenario. For the file with the most demodulated slots, two reference signals, RS7 and RS8, obeyed the three categories. The average and maximum throughput

gain was 64.98% and 127.23% for RS7, and 63.60% and 125.45% for RS_8.

For the two scenarios, one sees an improvement of the proposed scheme relative to the expected scheme, being enhanced when one considers individual reference signals for received power calculation. This is due to their more constant behavior, contrary to when one performs the average, as the channel variations impact the constant behavior of the expected throughput.

A final view of the implemented model and the framework associated with it, leads one to suggest work improvements and future work to enhance the reliability of the model and the results. The first improvement refers to the synchronization of the multiple antenna elements. The implemented model made use of the General Purpose Input/Output blocks to send the trigger signal to multiple sides of the MegaBEE. As the equipment possessed imperfections in terms of latency, it led to synchronization issues that nullified the improvement when using multiple antennas. One way to improve this problem is to make use of the White Rabbit protocol using the block with the same name on BPS. The White Rabbit block provides an implementation of sub-nanosecond synchronization on the megaBEE platforms using a master-slave protocol. Sharing the same reference clock, one could have one master MegaBEE controlling another equipment, achieving a more accurate synchronization between the platforms. This leads to another improvement, by generating the reference clocks externally using a more accurate clock source, for example a rubidium clock being constantly calibrated over GPS. The local oscillator frequencies of the MegaBEE are generated from this reference clock, however it can also be generated externally from a more accurate source to minimize the carrier frequency offset between the transmitter and receiver oscillator.

In terms of the data acquisition procedure, the next step would be to fix the XGE data acquisition method packet loss rate. One could reduce this loss by reducing the number of XGE connections to the host computer thus reducing its load and improving the rate of received packets. For the proposed scheme, one way to improve is to determine the SINR value more accurately taking into account the cell load and the RSRQ value, as the implemented model does not perform any evaluation of the cell load to calculate the SINR. The SINR calculation is also affected by the number of cells considered as interferers. By obtaining the exact location of the several eNBs around the environment one can have a more accurate description of the two scenarios under question. Given that cell location API used in this thesis possesses location inaccuracies, it can lead to possible misinterpretations of what is a sparse or dense deployment influencing the SINR calculation.

Annex A

Additional Data Acquisition Methods Implementation

Annex A

This annex contains the implementations of the BRAM and XGE Method using the prototyping platform MegaBEE.

The schematic model represented in Figure A.1 refers to the BRAM Method using two Shared BRAM blocks to store the captured data.

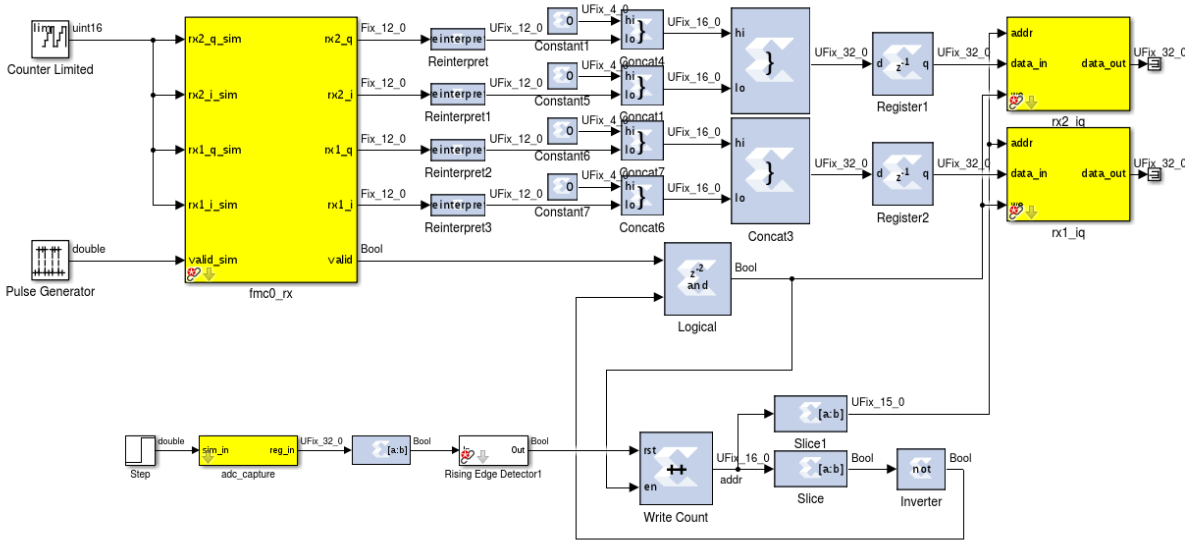

Figure A.1– BRAM Method capture subsystem.

The block labelled “fmc0_rx” is the interface for the FMC112 receiver, providing one I and Q samples every 4 reference clock cycles. Each receiver block supports two RF ports, meaning that two receiver blocks would need to be used to provide the output for one side of the MegaBEE.

The four outputs corresponding to the IQ samples of the receiver are a 12-bit signed two’s complement number which is then converted to a 12-bit unsigned number, using the Reinterpret block and appended extra bits to convert it to a 16-bit unsigned number. The four outputs are then concatenated in groups of two, each group belonging to the corresponding RF port, creating a 32-bit unsigned number which is being stored in Shared Bram blocks, labelled “rx1_iq” and “rx2_iq”.

To increase the number of samples captured, one would need to add to the model an additional counter of higher order for when a set of BRAM is already filled, it would trigger the filling process of another set of BRAMs, as seen in Figure A.2. The mechanism makes use of the “Write count” counter to control a de-multiplexer whose outputs are used to control which BRAM is filled with data coming from the receiver block. When the counter reaches its maximum count, the writing process is completed by slicing the most significant bit of the counter.

The maximum number of BRAMs that can be used for this type of acquisition of RF data, is 20 BRAMs. For the purposes of testing the performance of this design it was used this maximum number to store the acquired data of only one RF port of the MegaBEE, achieving a total of 655 360 samples of the in-phase and quadrature phase components of the signal. The maximum value of 655 360 samples would have to be divided by the number of ports to be used in the design model, given that when used in its full capacity of 4 ports, the obtained value is 163 840 samples which is not enough to capture a whole LTE frame of 10 ms.

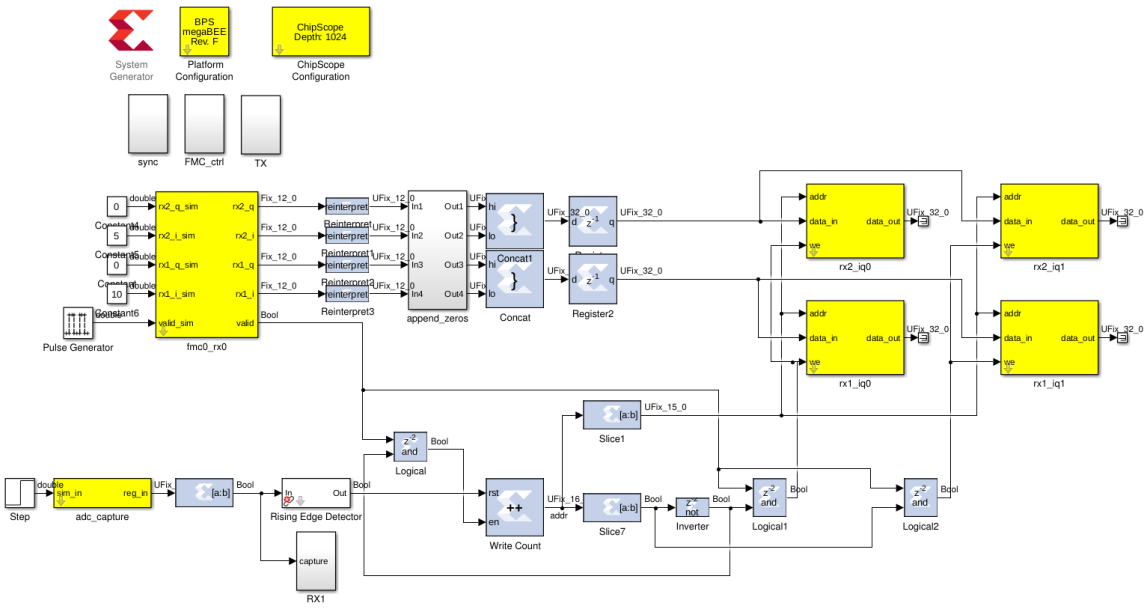

Figure A.2 – Mechanism for storing in multiple BRAMs.

Regarding the XGE Method, similarly to the previous methods, the main subsystem in Figure A.3 (a), contains the Software Register that triggers the capturing procedure, “adc_capture” and two subsystems regarding the receivers for all ports in a MegaBEE side. The synchronization procedure employing GPIO blocks used in the DMA method is also used in this method. Five subsystems were created to perform the described functionalities for the XGE method as seen in Figure A.3 (b).

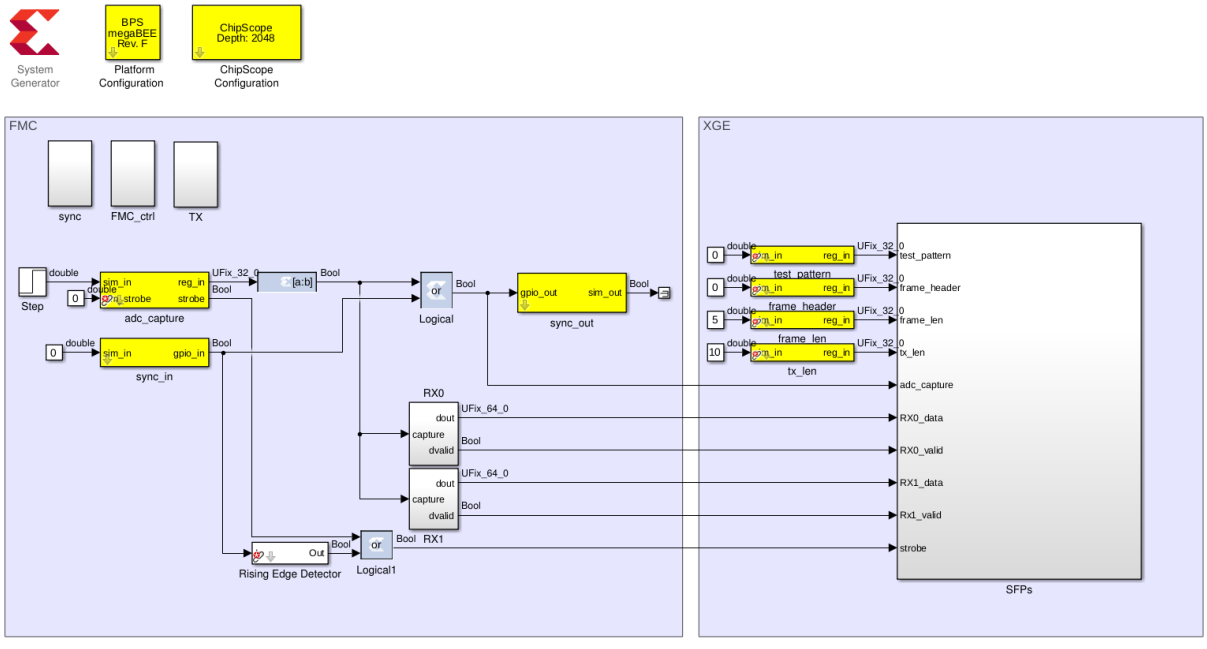

(a) BPS high-level model for the XGE Method.

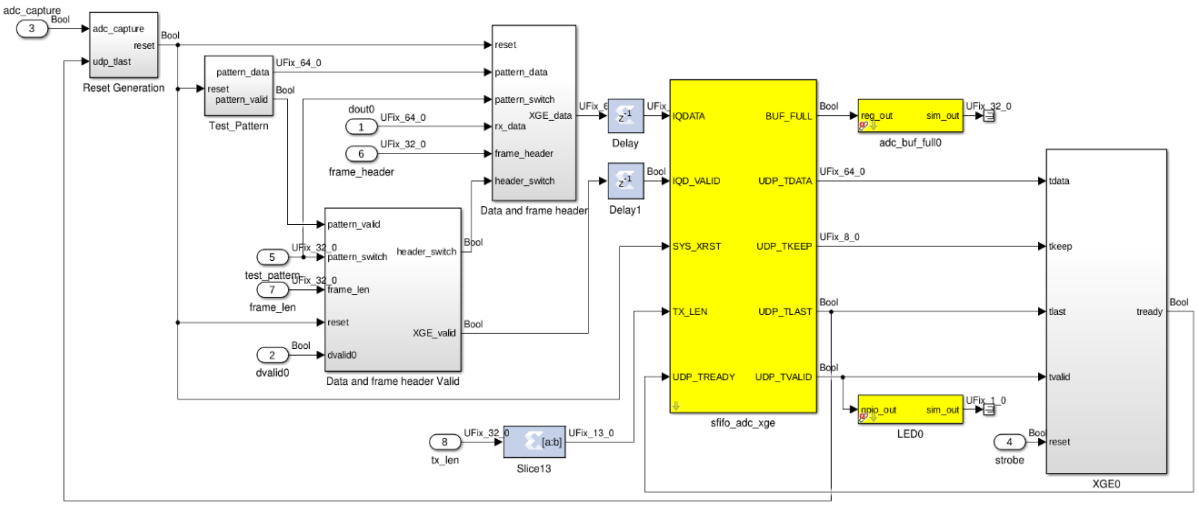

(b) Frame Generation for data transfer with XGE Method.

Figure A.3– XGE Method main subsystems.

The data to be transferred using the XGE method can either have origin from the RF transceiver or from the test pattern subsystem. To control which data is transferred a software register “test_pattern” is used as a switch, given that when this software register is assigned, test pattern data is streamed and no frame header is appended to the transmitted payload data. The frame structure is generated with the “Data and frame header” subsystem, where the “test_pattern” is used to select which data is transmitted. As the transmission procedure follows a protocol similar to DMA FIFO, the data generated by the aforementioned subsystem is equivalent to TDATA flag used in the DMA method. For the TVALID flag assignment, the subsystem “Data and frame header valid” is used not only to generate this flag but also to select whether there will be a header in the transmitted data. Lastly, in the “XGE0” subsystem, the XGE and UDP TX blocks undergo their setup via multiple software registers, and in the “Reset Generation” subsystem a common reset signal for the multiple counters used in this model is created.

The “Reset Generation” subsystem, as presented in Figure A.4, has the function of resetting all the existing counters of the subsystem in the XGE method.

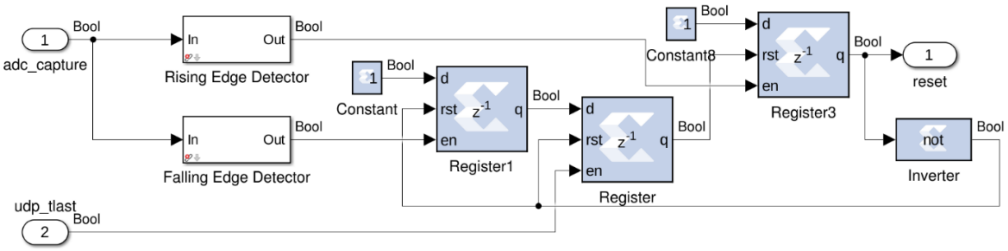

Figure A.4 – "Reset Generation" Subsystem.

The two inputs of this subsystem are “adc_capture” software register and the flag “udp_tlast” generated by FIFO subsystem “sfifo_adc_xge”. The output is a simple delay of the “adc_capture” signal, meaning that when the capturing procedure is triggered, the reset signal is generated as a copy of the triggering

signal. This is achieved with two registers that introduce a delay of a clock cycle, being enabled by the rising and falling edge of the triggering signal. After the “adc_capture” is set to low, the XGE transfer is completed which will enable the “udp_tlast” signal and reset the register that produces the output of the “Reset Generation Subsystem”. There is also a delay for this subsystem reset in order to complete the XGE transfer during the cycle that “udp_tlast” is assigned.

The flag IQ_VALID assignment in the “sfifo_adc_xge” is similar as the TVALID assignment undertaken using the DMA method. A master counter and a relational method are used to generate a square wave shaped signal for the outputs of the “Data and frame header Valid” subsystem presented in Figure A.5. The output XGE_valid is a mixture between the valid signal originated by the FMC112 receiver blocks (“dvalid”), which is assigned every four clock cycles, and a delayed version of the Relational block output signal “header_switch”. This signal is assigned whenever the output of a counter is equal to the chosen frame length. A delay is added to this signal in order to append the frame header before a new frame begins. The assignment of the IQ_VALID flag will dictate how XGE transfers to the FIFO “sfifo_adc_xge” happen, as it operates in a similar manner as the TVALID flag in the DMA FIFO, thus by assigning this flag as mixture between the two aforementioned ports allows the correct sorting of the transceiver data and also the frame header appending to the transmitted data.

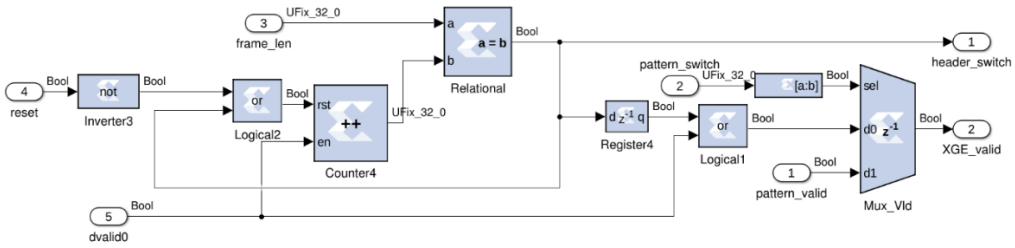

Figure A.5 – "Data and frame header Valid" Subsystem.

For the generation of test pattern data, Figure A.6, one would have to take into account how the data is being packed in a UDP packet. Knowing that a UDP packet has a width of 32 bits and a variable payload depth, the 64-bit input of the “sfifo_adc_xge” block must be divided in blocks of 32 bits, being that the first 32 bits will correspond to the first payload word and proceeding 32 bits the following word. The pattern data aimed to recreate a counter. By using this storing system of 32 bits per UDP payload word, one would have to generate a given number on the first 32 bits and on the next 32 bits an increment of this number, given that in each clock cycle both these numbers would increment one value as well. The transmitted data would then have a counter pattern in every 32 bits, facilitating any debugging or analysis of the received data and it would also show an indicator of packet losses, as the received data would have gaps, without the need of adding a frame header. The pattern data, p_data, was thus generated as a function of a 32-bit counter according to:

$$p_{DATA[0:63]}(k) = \begin{cases} p_{DATA[0:31]}(k) = n(k) \,||\, 0_{(2)} \\ p_{DATA[32:63]}(k) = n(k) \,||\, 1_{(2)} \end{cases} \tag{A.1}$$

Where the operator || refers to concatenation operation and:

- $n(k)$: Counter value at clock cycle k.

In terms of generating the IQ_VALID flag, a square wave waveform with a duty cycle of 8 periods was created by using a single input AND gate of a free-running 3-bit counter.

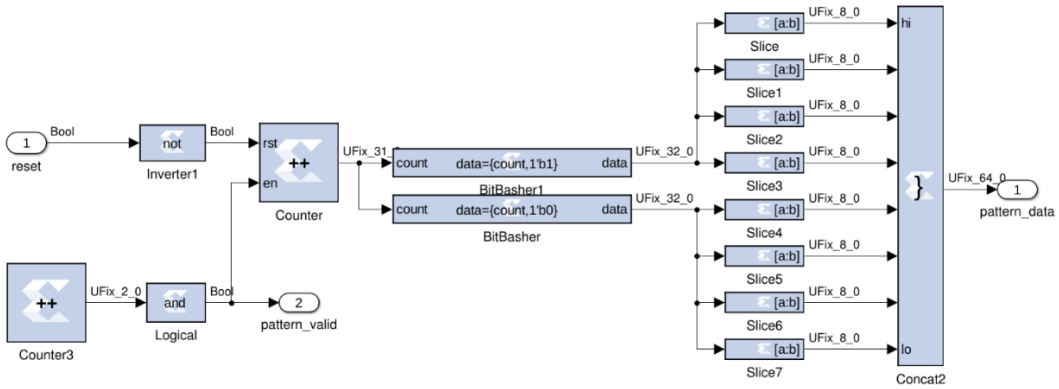

Figure A.6 – "Test_Pattern" Subsystem.

The assignment of IQ_DATA in the “sfifo_adc_xge” block is performed by the “Data and frame header” Subsystem represented in Figure A.7. Similar to how TDATA is assigned in the DMA method, in this method the assignment of this flag is done with a simple multiplexing engine to append the frame header to the payload data. The signal “header_switch” generated by the “Data and frame header Valid” subsystem is used to select when the frame header is to be appended, being that this frame header follows the structure already detailed before and is the result of the concatenation of a known frame pattern and a counter. The “pattern_switch” signal is then used to select which data is to be transferred to the FIFO “sfifo_adc_xge”. When this signal is low, the source of the data to packetized is from the RF transceivers with the added frame header, and when it is high, the data to be transmitted becomes solely the test pattern data without any type of appended frame header.

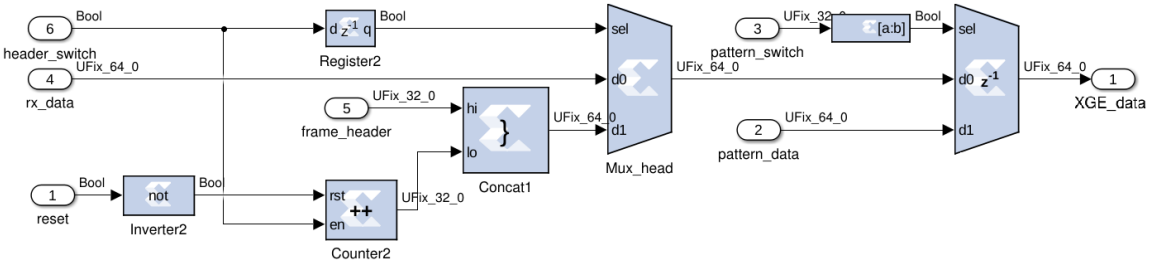

Figure A.7 – “Data and frame header” Subsystem.

The final subsystem “XGE0” refers to the setup of the XGE connection from the MegaBEE and a host computer. The 10 GbE block, “XGE0” in Figure A.8, when used on its own only instantiates an Address Resolution Protocol (ARP) responder, access to MAC and network configuration, and a physical connection to the pins and ports to be used in the design [BEEc17a], in this case the SFP+ outputs. The inputs of this block refer to the assignment of the MAC address and IP address for the XGE interface in the MegaBEE. The UDP Stream TX block is used jointly with the XGE block to stream data from a BPS design and a host computer, representing the XGE endpoint.

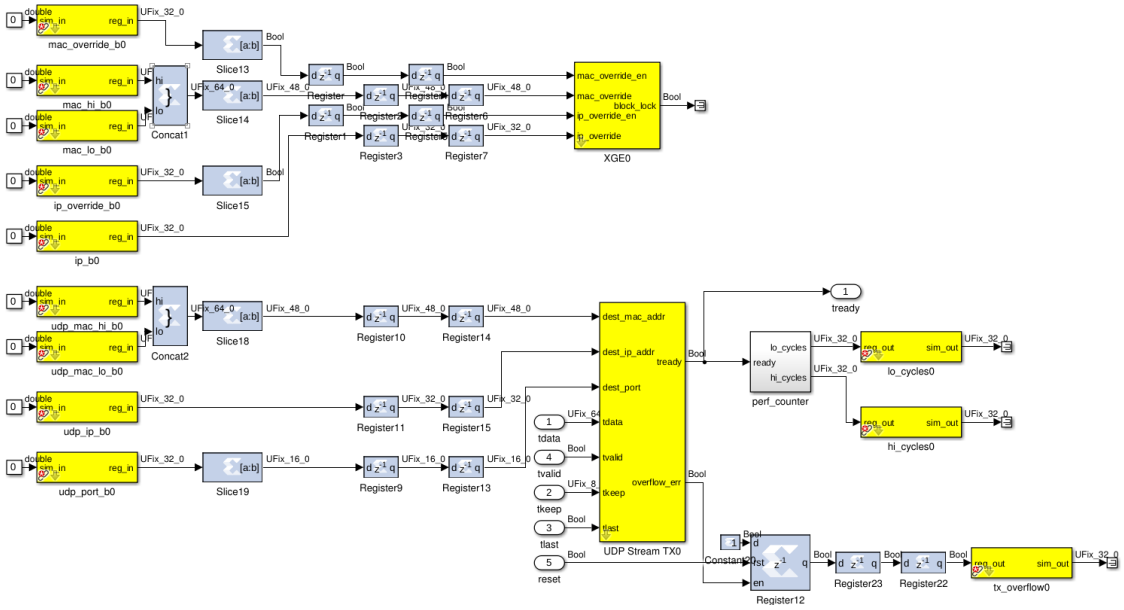

Figure A.8 – “XGE0” Subsystem.

In hardware, the ports on this block provide an AXI-4Stream [ARM10] interface to a UDP packetizing core and the inputs of this interface correspond to the outputs of “sfifo_adc_xge” block. There are two FIFOs involved in the XGE method, the first FIFO pertains to the “sfifo_adc_xge” block that stores the payload data to be packetized. The second FIFO refers to the UDP Stream TX block where the entire payload is buffered and counted before the transmission begins. This block fills the Ethernet, IPv4, and UDP headers of the UDP packet according to the IP and MAC addresses assigned in the XGE block and the destination IP and MAC addresses and port of the host computer. The assignment of all the addresses and destination port is done via Software Register, given that in the case of the assignment of a MAC address, two SRs must be used as a MAC address is 48-bit word while a Software Register can only store 32-bit words.

Annex B

Data Acquisition Methods Simulations

This annex contains the simulations performed to assess the functionality of the three implemented methods for data acquisition using the prototyping platform MegaBEE.

The assessment of the the three methods for data acquisition was done by the means of simulations, using the Vivado System Generator for DSP Gateway Out blocks that convert the fixed point binary integer to Simulink double. The evaluated flags correspond to the outputs of the several subsystems created, by plotting the converted value with a Scope block.

In Figure B.1 it is presented the first assessment test for the BRAM method in regard to the Addressing Mechanism used to switch the BRAM to store the captured data. As mentioned in the implementation section for the BRAM method, a set of BRAMs is filled when the previous set is completely filled with 2^{15} samples from IQ data provided by the receiver. To assess the functionality of this mechanism, 4 BRAMs are considered for the data storing, and two simulations are performed to verifiy if the counter resets when a BRAM is completely filled, and if the selected BRAM changes when the the counter resets.

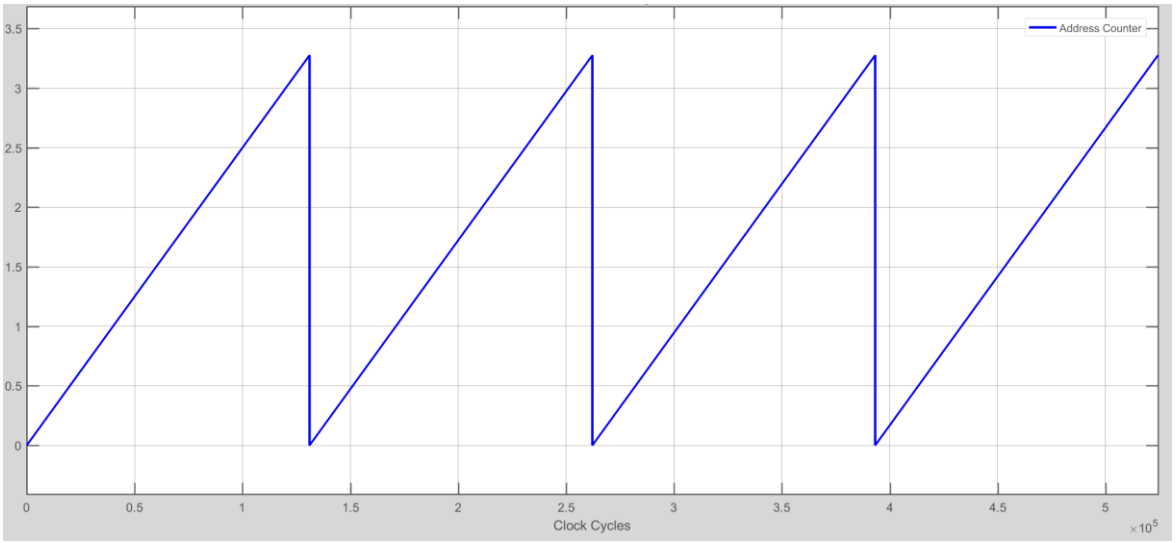

(a) Addressing Simulation.

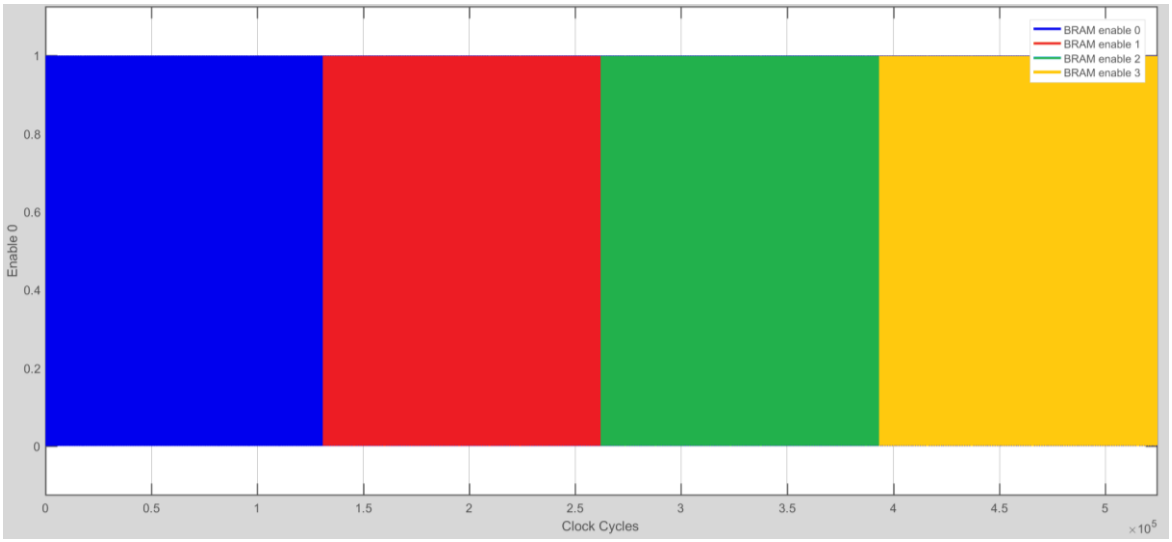

(b) Shared BRAM enable Simulation.

Figure B.1 – BRAM Addressing Mechanism Simulation.

In Figure B.1 (a), one can see that the addressing counter do resets when its counter value reaches 2^{15}, being that the enable flag for the BRAM to be filled changes when the address counter reaches its full count as seen in Figure B.1 (b). The mechanism to store in multiple BRAMs is thus assessed. The second test of the BRAM method is presented in Figure B.2. This test corresponds to the final simulation to assess the total functionality of the BRAM method to store the capture RF data. With the BPS receiver block, one can simulate RF data by using its simulation inputs. The simulated input used for the port 0 of the MegaBEE is thus a simple step function with magnitude 10 as seen in Figure B.2 on the variable "RX0_data". The data is store every 4 clock cycles in the BRAM blocks, being that the addressing counter has to increment its values in every 4 cycles in order to store the captured data in each address of the BRAM. From Figure B.2, this behavior can be observed, where the enable flag is asserted every 4 cycles and address counter increments its value as mentioned before, proving the correct functionality of the implemented method.

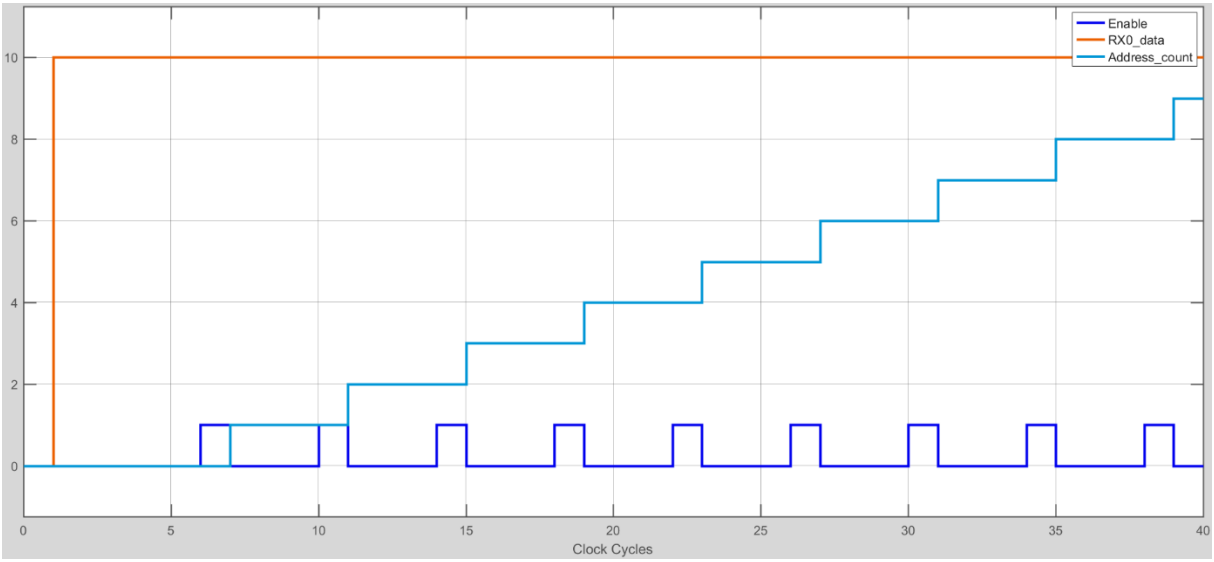

Figure B.2 – BRAM Method Final Simulation.

Two simulations were performed to assess the functionality of the DMA Method. The first test verifies the correct functionality of the multiplexing mechanism created to transfer GPS data, reference counter data on the first and second counting cycles, and RF data on the preceding counting cycles. To emulate the transferred data, different values are given to the GPS coordinates and the transmitted RF data. For the GPS data, the simulated value was a constant function with magnitude of 15, for the received RF data, the simulated value differs from ports 0 and 1, and ports 2 and 3. In regard to ports 0 and 1 the constant value chosen for simulation had a magnitude of 10 whereas for ports 2 and 3 the magnitude was of 5. In Figure B.3, the multiplexed data, TDATA, is plotted together with the counter "count" that controls the multiplexing mechanism. One can see that on the on the first counting cycle, the multiplexed data takes the value of 15 meaning that GPS data is selected. On the other hand, for the second counting cycle, the multiplexed data takes the current value of the free counter used as a reference, incrementing its value during two clock cycles. For the preceding counting cycles, the multiplexed data switches the magnitude from 10 to 5, meaning that the multiplexed value takes the value from the simulated inputs of ports 0 and 1, and ports 2 and 3. The plotted TDATA, however, possesses a delay

of 1 counting cycle, meaning that the selection of the multiplexed data from the counter is delayed before being used as input to the DMA FIFO block.

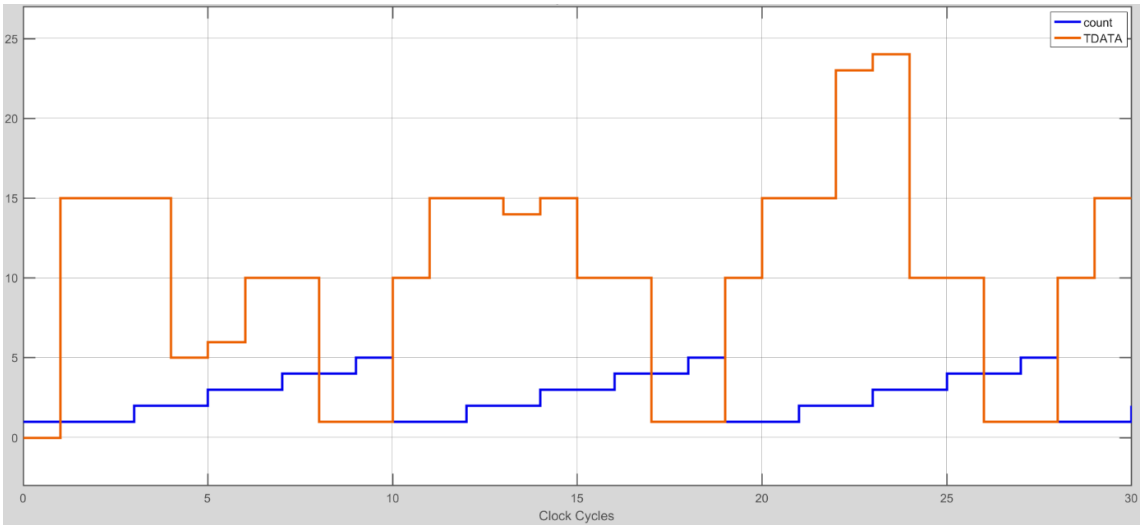

Figure B.3 – DMA Multiplexing Mechanism Simulation.

The second simulation, similar to the BRAM method, aims to assess the full functionality of the implemented method. For this simulation, the flags TDATA and TVALID for the DMA transfer are tested to verify if there is any synchronization issue in their assignment. The TVALID assignment must be synchronized to the overall behavior of TDATA to guarantee that the way the information is organized during the transfer is respected. As the DMA transfer occurs when the TVALID and TREADY flags are assigned, and the TREADY in the Simulink environment is always assumed to have magnitude of 1, the TVALID assignment indicates that the portion of TDATA assigned during the same cycle is transferred. From Figure B.4, one can see that the TVALID flag is assigned every two clock cycles after the “adc_capture” value is set, and during the cycles that the TVALID is assigned the transferred data follow the expected format for the transfer: the first cycle refers GPS data whereas in the second the reference counter data is selected. On the following cycles data from ports 0 and 1, and ports 2 and 3 are transferred.

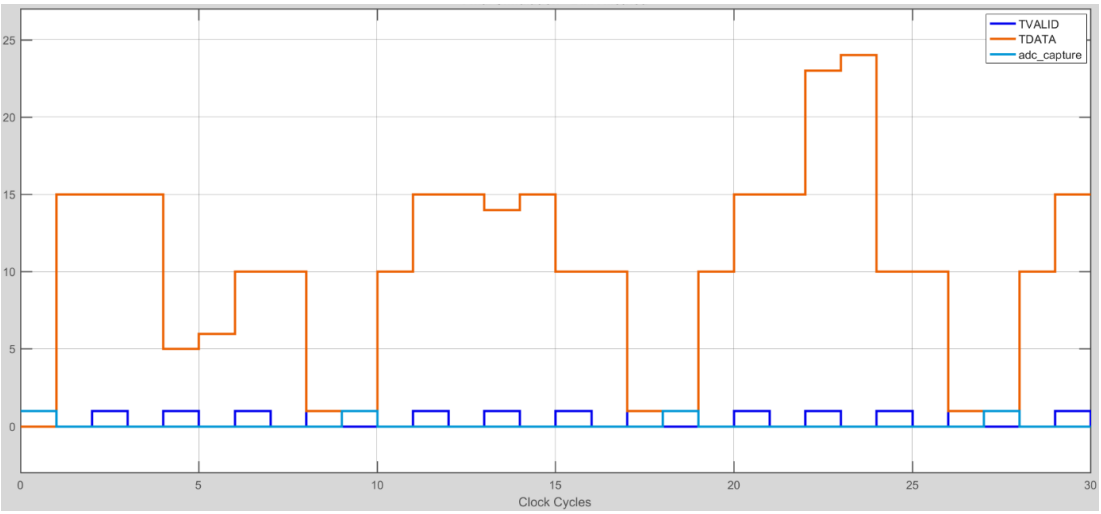

Figure B.4 – DMA Method Final Simulation.

The assessment of the XGE Method was done in a similar fashion as the previous DMA Method in what concerns the IQD_Valid flag assignment in the “sfifo_adc_xge” subsystem as it is equivalent to the TVALID flag. The assignment of this flag is performed by a similar multiplexing mechanism as the DMA method, given that the data to be transferred using the XGE method needs to have a frame appended for control purposes. The IQD_VALID flag presented in Figure as “XGE_Valid” is generated by two waveforms presented in Figure B.5 (a) and Figure B.5 (b). In Figure B.5 (a), the “header_switch” variable is assigned according to the frame length of the data to be transferred. For simulation, the frame length was set to 5, being that the “header_switch” is expected to be assigned when five payload words are transferred. By observing the simulation results, this behavior is obtained being that there is a delay of 1 clock cycle for the “header_switch” assignment. In Figure B.5 (b) the “rx_valid” flag is assigned five times in the first 20 clock cycles, meaning that five words from the receiver block can be transferred to the “sfifo_adc_xge” block. The resulting “XGE_Valid” assignment can be seen in Figure B.5 (c) where the assignment is done every 4 clock cycles, with an extra assignment during the 20th clock cycle due to the frame header appendage.

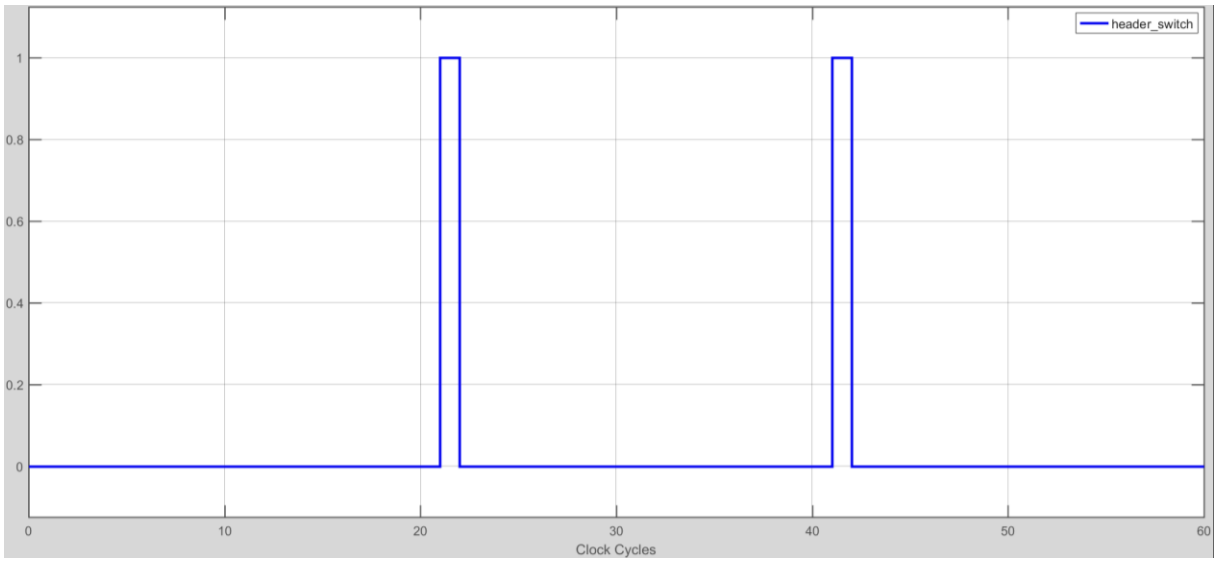

(a) “Header Switch” assignment.

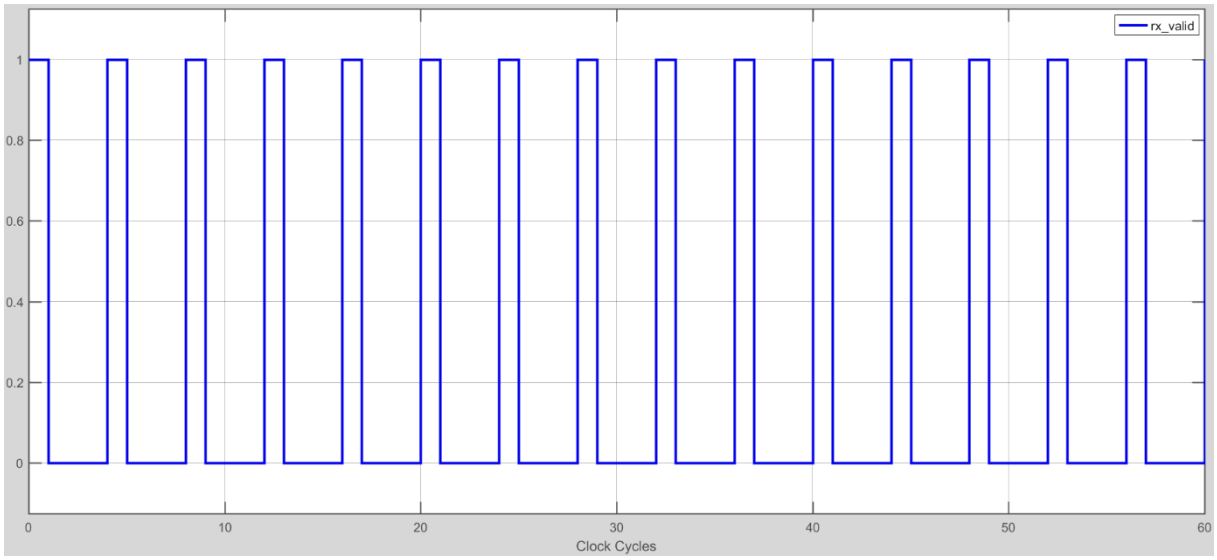

(b) “rx_valid” assignment.

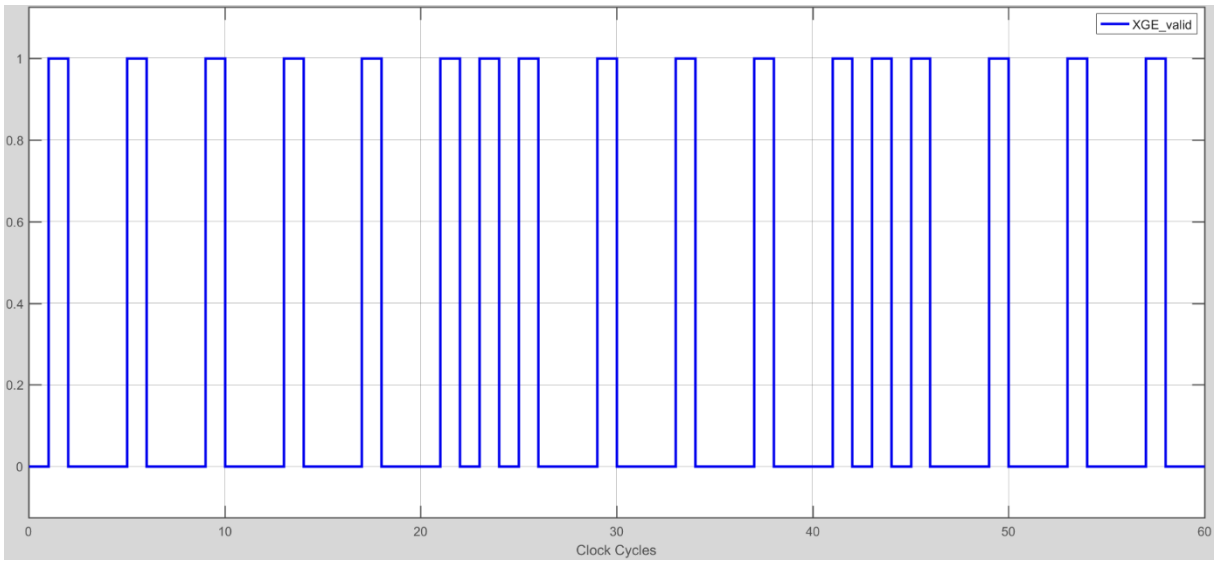

(c) “TVALID” assignment.

Figure B.5 – “Frame and header valid" Subsystem Simulation.

The final simulation is presented on Figure B.6 for the simulated data of ports 0 and 1. Given that the subsystem responsible for the transfer of ports 2 and 3 is identical to the one employed in ports 0 and 1, only the latter is simulated as the results are guaranteed to be equal. For this simulation, the simulated value for the ports is a constant value with magnitude, and the frame header only possesses the frame counter not any frame pattern. The expected behavior for this simulation is that the flag “XGE_Valid” should be synchronized with how the data to be transferred, “XGE_data”, is formatted. For the first 5 “XGE_Valid” cycles after the “adc_capture” is triggered, one can observe that the transferred data is the one from ports 0 and 1. The additional assignment of the “XGE_Valid” flag preceding the initial 5 cycles pertains to transfer the frame header containing the frame counter. From Figure B.6, one can observe the describe behavior for both the transceiver data and the frame counter.

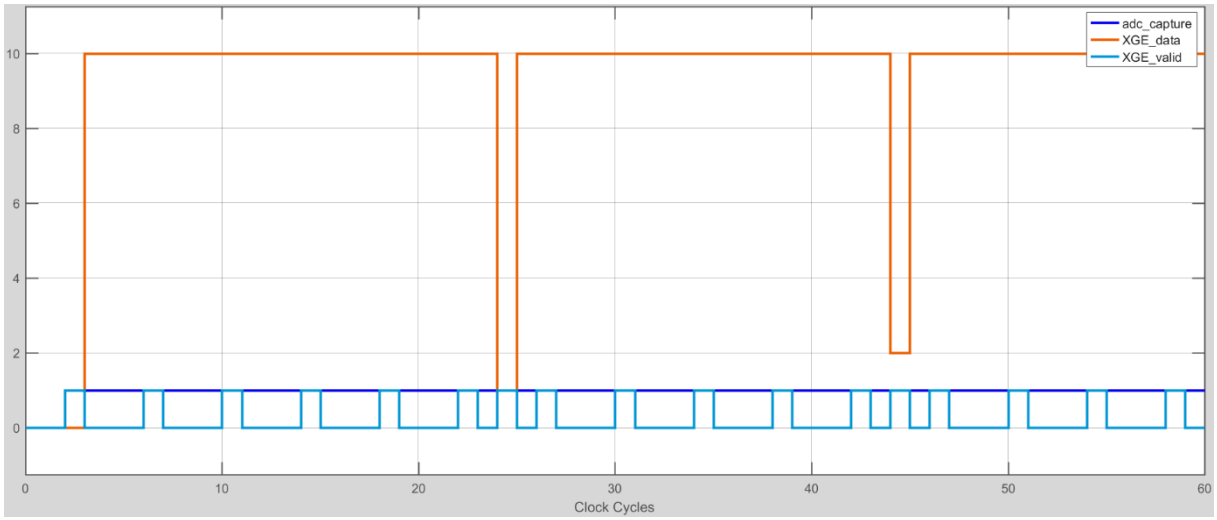

Figure B.6 – XGE Method Final Simulation.

Annex C

Base Stations Information

Annex C

This annex contains the simulations performed to assess the functionality of the three implemented methods for data acquisition using the prototyping platform MegaBEE.

The location of the base stations for the considered environment were obtained based on the information collected on the Iphone's Test Field Menu, being presented in Figure C.1.

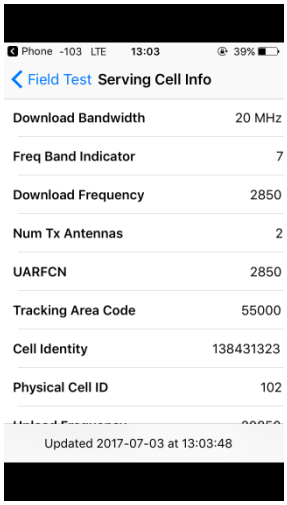

(a) Cell-ID 102.

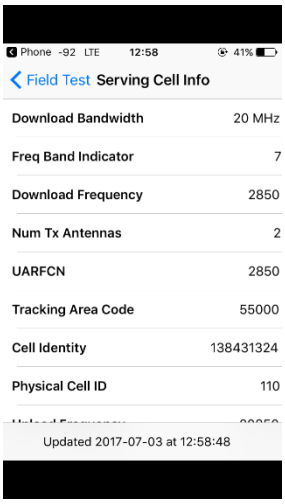

(b) Cell-ID 110.

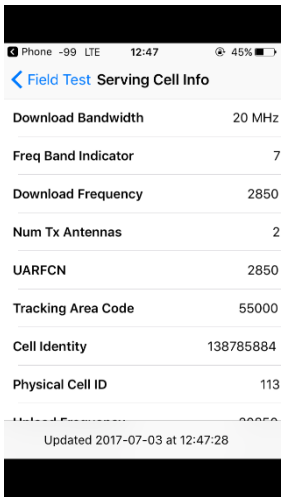

(c) Cell-ID 113.

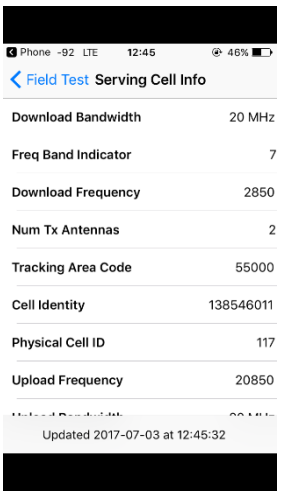

(d) Cell-ID 117.

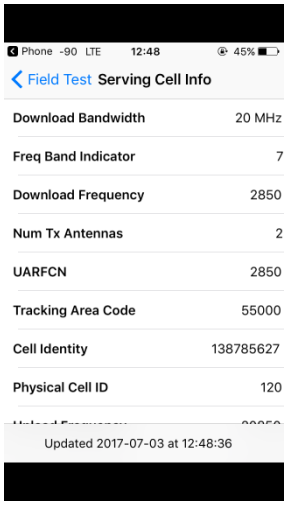

(e) Cell-ID 120.

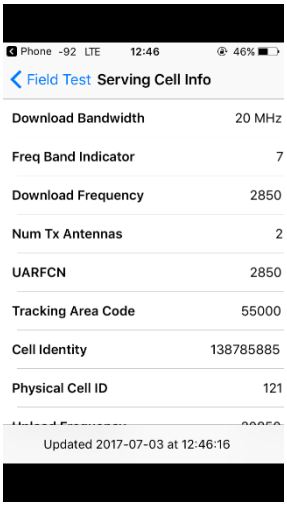

(f) Cell-ID 121.

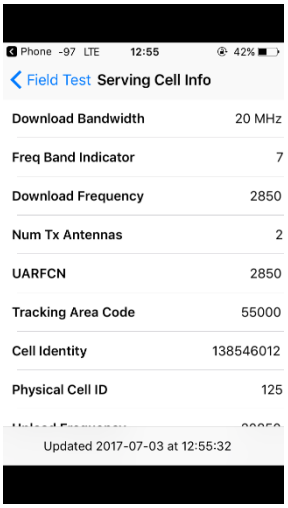

(g) Cell-ID 125.

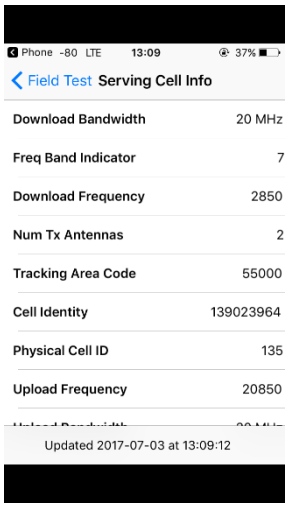

(h) Cell-ID 135.

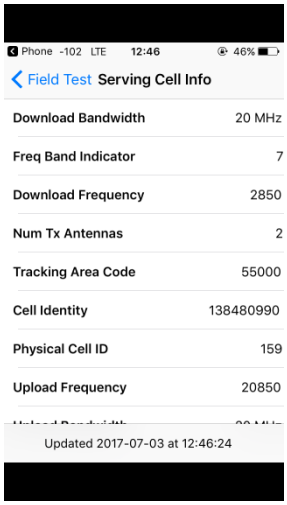

(i) Cell-ID 159.

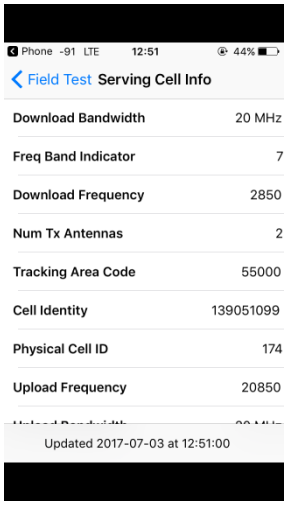

(j) Cell-ID 174.

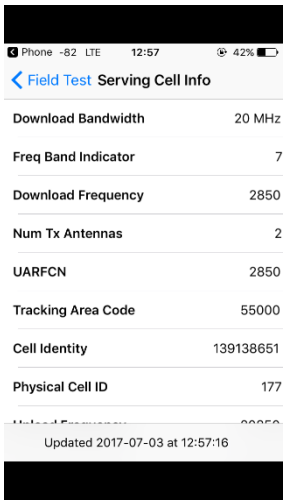

(k) Cell-ID 177.

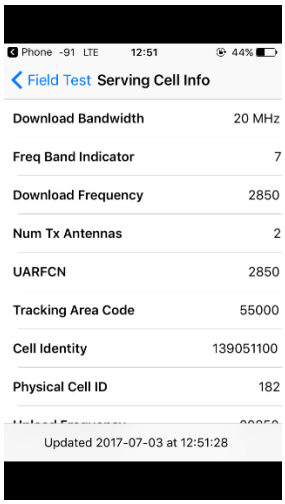

(l) Cell-ID 182.

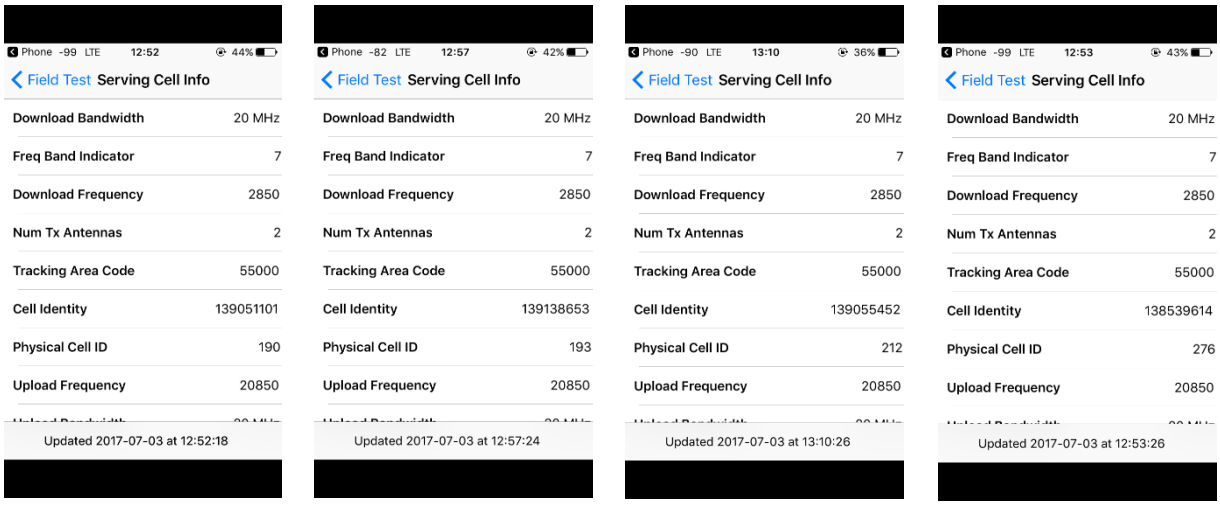

(m) Cell-ID 190. (n) Cell-ID 193. (o) Cell-ID 212. (p) Cell-ID 276.

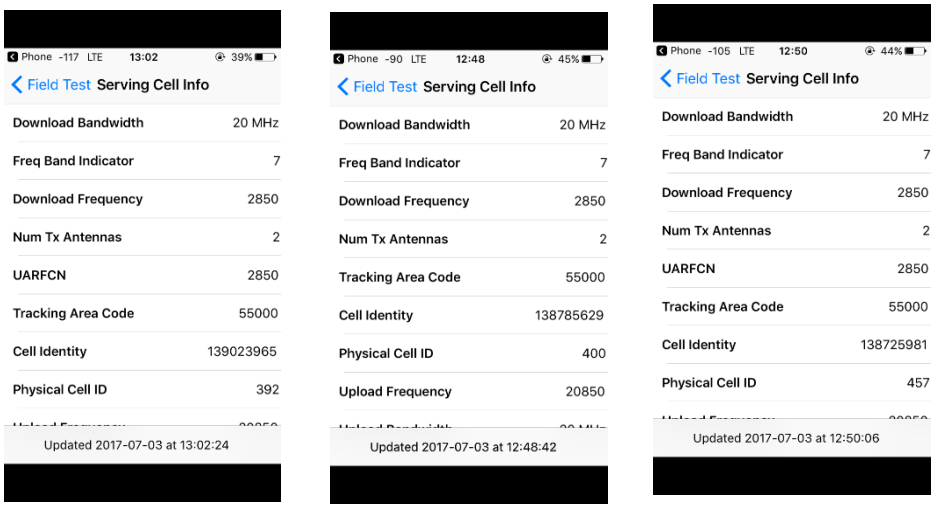

(q) Cell-ID 392. (r) Cell-ID 400. (s) Cell-ID 457.

Figure C.1 – Base Station Recordings.

Annex D

Additional Results

This annex contains the absolute results obtained of the evolution of the throughput schemes along the demodulated LTE slots for the two scenarios under analysis.

The absolute results obtained for the two files within Categories 1 and 3 in the sparse deployment scenario for average reference signals correspond to captures taken at the 38th and 40th second of the measured interval, being presented in Figure D.1 (a) and (b) respectively. Since the optimal throughput in both files is always lower than the expected throughput, no diversity was considered for this initial analysis.

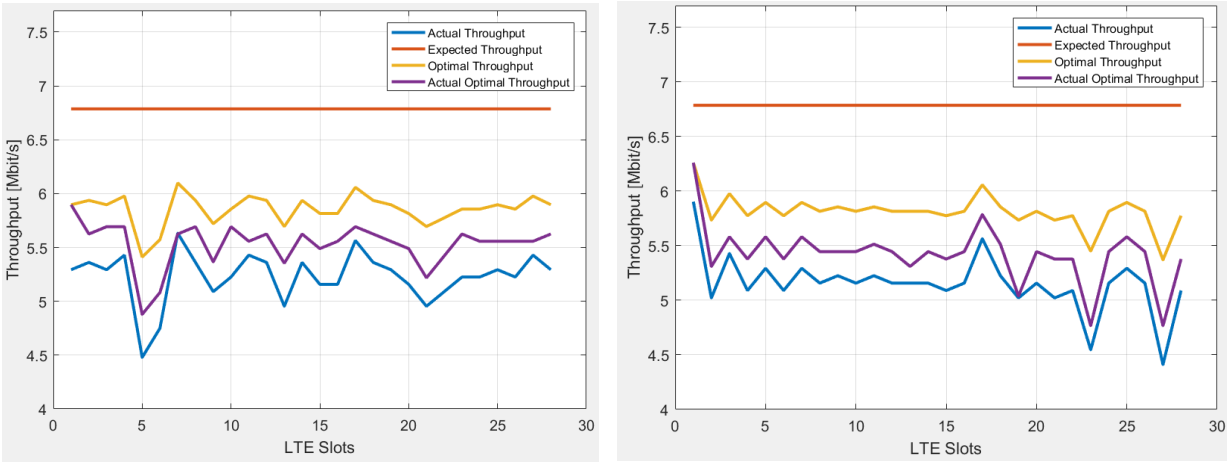

(a) File 38. (b) File 40.

Figure D.1 – Sparse Deployment Throughput Curves for Average Reference Signals.

A general improvement of the throughput curves behavior was observed when considering individual reference signals. Overall the reference signals with the best performance are RS7 and RS8 being presented in Figure D.2, given that for RS1, RS2, RS3 and RS4 the actual throughput value along the slots is very similar to the proposed scheme actual optimal throughput.

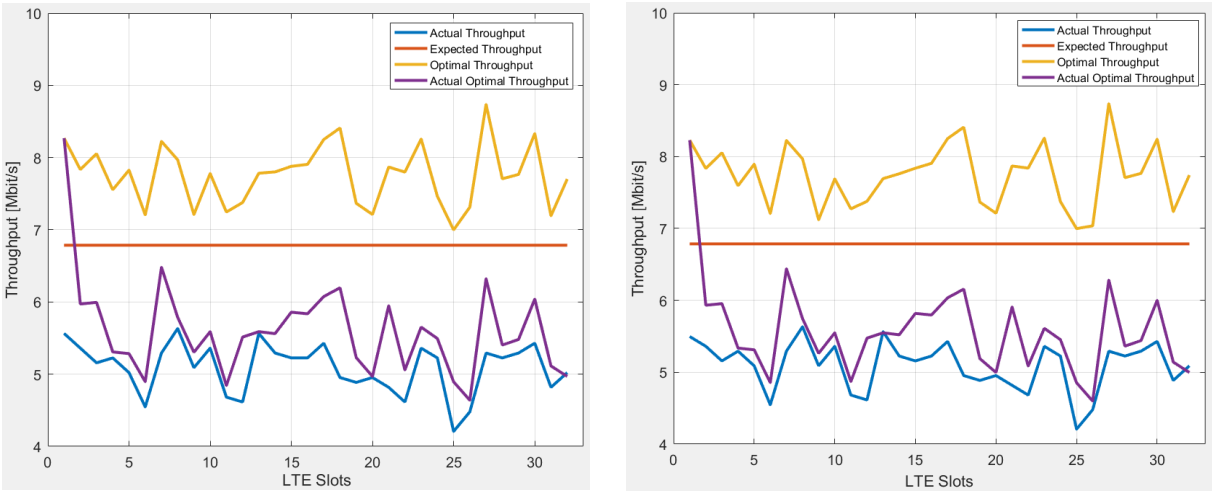

(a) RS_7. (b) RS_8.

Figure D.2 – Sparse Deployment Throughput Curves for Individual Reference Signals.

The overall trend is that the actual throughput tends to be equal to the expected throughput, being justified by the fact that for the 16 antennas used in this analysis the resource block with highest SINR is chosen for the demodulated grid. This will lead that the actual throughput, given that it is calculated by the sum of components which are more likely to be above the threshold imposed by the expected

throughput.

The aforementioned behavior is especially seen in Array 1, which leads to the conclusion that the signal being received in the 8 antennas composing this array is very similar. Nevertheless, it is worth noting that for the considered reference signals, the actual throughput does not match the expected throughput in Array 2 as accurately as the Array 1, due to the more different channel conditions experienced in the 8 antennas that form this array.

For the reference signal with the best performance, RS_3, the throughput curves can be seen in Figure D.3 (a), (b), and (c) for Arrays 1, 2 and MIMO respectively. It is worth to note the increase of the throughput in each scheme, typical in a 2x2 MIMO configuration.

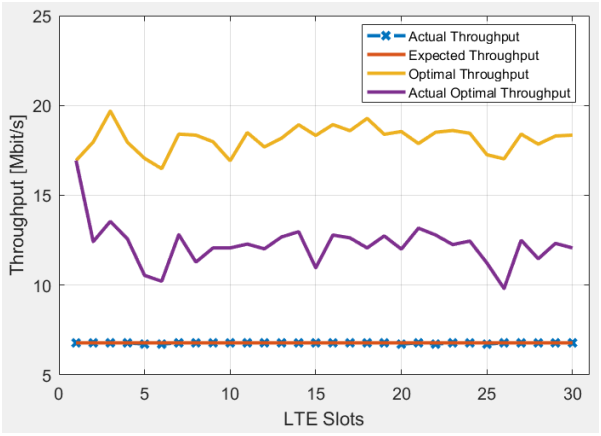

(a) Array 1.

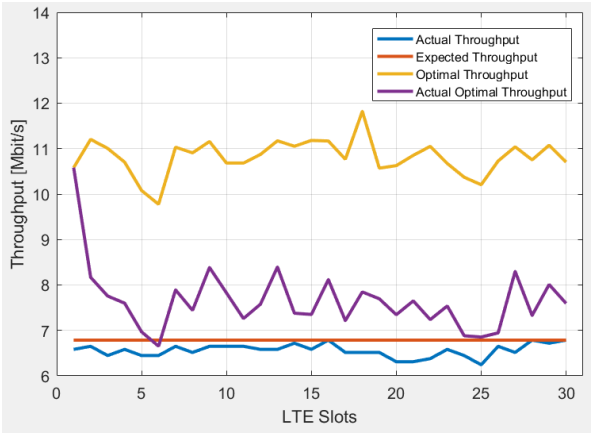

(b) Array 2.

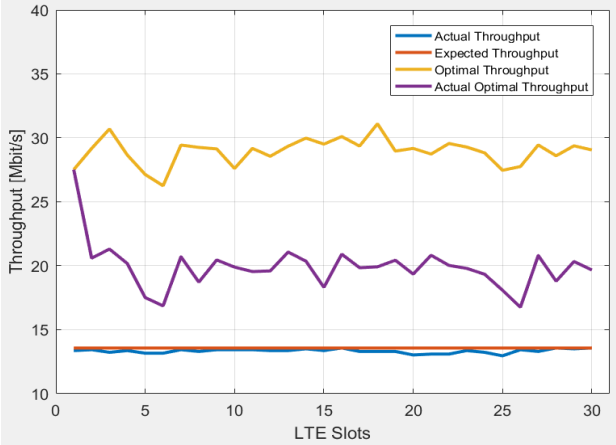

(c) MIMO.

Figure D.3 – Throughput Curves Performance considering Diversity.

Round Robin is the first scheduling algorithm to be evaluated, for both the proposed scheme and sub-band scheme. The throughput curves for each secondary node is presented in Figure D.4, with the total cell throughput being given by the sum of each element for a slot. Given that the round robin algorithm does not take into account the channel conditions of the different secondary nodes, the same number of resources is allocated to each element.

The secondary node 5 with the best channel conditions experiences a higher throughput than the

remaining nodes, however not as severe as it is expected for the proceeding scheduling algorithms. Comparing the proposed scheme and the average sub-band one, it can be seen that the overall cell throughput is greater in the latter, being also possible to observe a higher level of fairness between secondary nodes as seen from the smaller gaps from node to node.

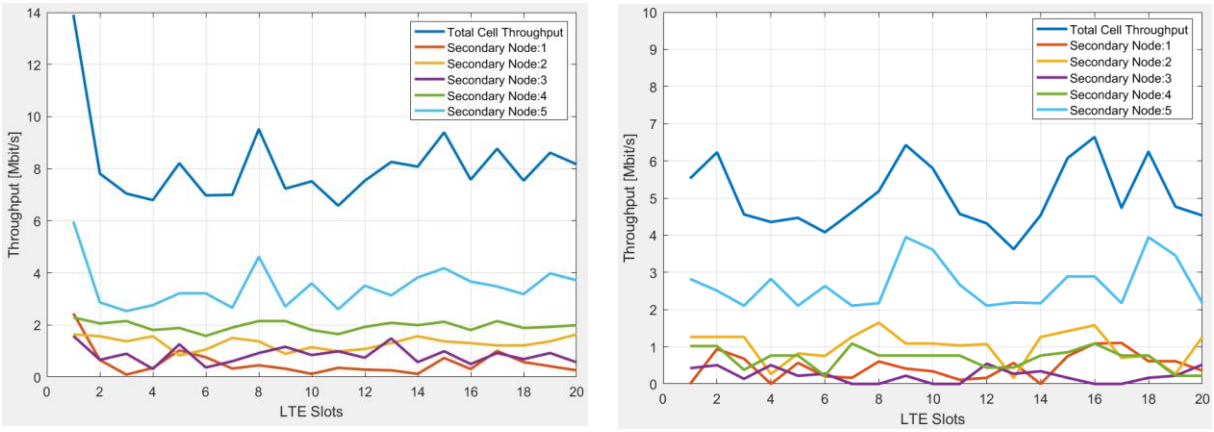

(a) Proposed Scheme. (b) Average Subband Scheme.

Figure D.4 – Round Robin Algorithm Performance.

The main theoretical premise behind the Best CQI algorithm is that the secondary node which has the best channel conditions (highest reported CQI) is the one that is allocated. This behavior is seen in Figure D.5, where for both schemes the secondary node 5, with the best channel conditions, is allocated in detriment of the remaining secondary nodes. Although there is overallocation in both schemes, the throughput experienced in each secondary node is greater in the proposed scheme than the average sub-band one, indicating an increase in both fairness and total cell throughput.

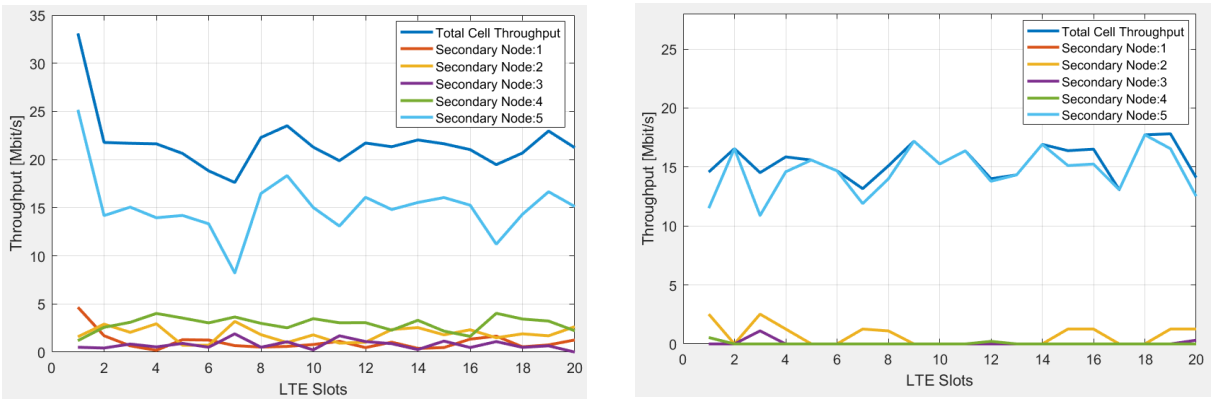

(a) Proposed Scheme. (b) Average Subband Scheme.

Figure D.5 – Best CQI Algorithm Performance.

For the Proportional Fair algorithm, in Figure D.6, one sees the throughput curves for the considered secondary nodes in both schemes for a sliding window size of 5 LTE slots. Different from the Best CQI algorithm, the Proportional Fair algorithm aims to encounter a middle ground between the fairness and total cell throughput by taking into account the previous channel conditions and not only the current ones. This creates a fairer allocation, without overallocation of a single secondary node.

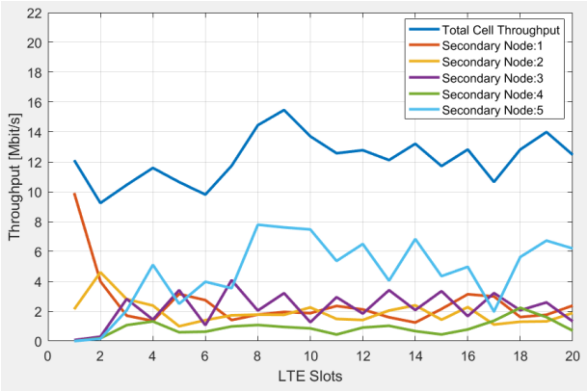

(a) Proposed Scheme.

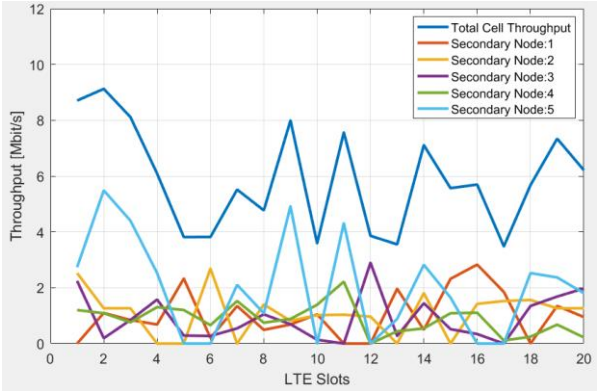

(b) Average Subband Scheme.

Figure D.6 – Proportional Fair Algorithm Performance.

For the dense deployment scenario, in Figure D.7, one can observe the throughput schemes evolution along LTE slots for the file with the highest number of demodulated LTE slots. This first analysis, determines the received power per resource block based on the average of the reference signals.

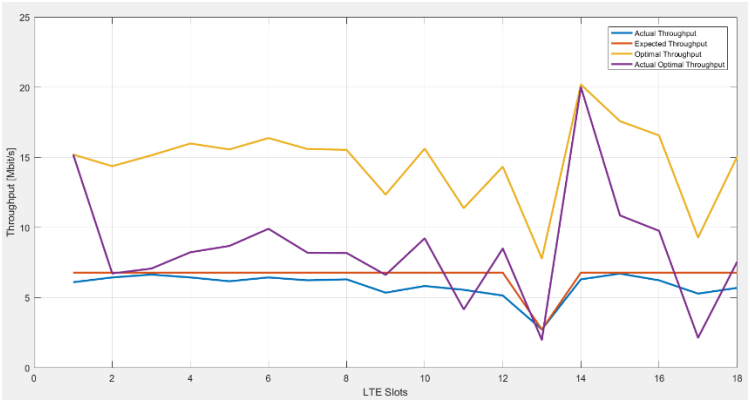

Figure D.7 – Dense Deployment Throughput Curves for Average of Reference Signals.

The throughput schemes behavior along slots in can be seen in Figure D.8 for individual reference signals RS_7 and RS_8.The behavior is similar when compared to the sparse deployment although there is a decrease of each scheme value along slots created by the interference increase in the scenario.

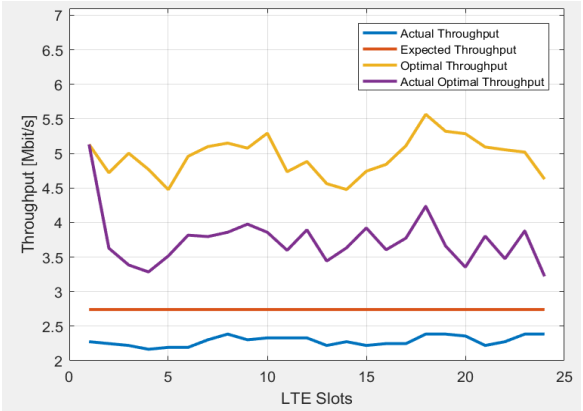

(a) RS_7.

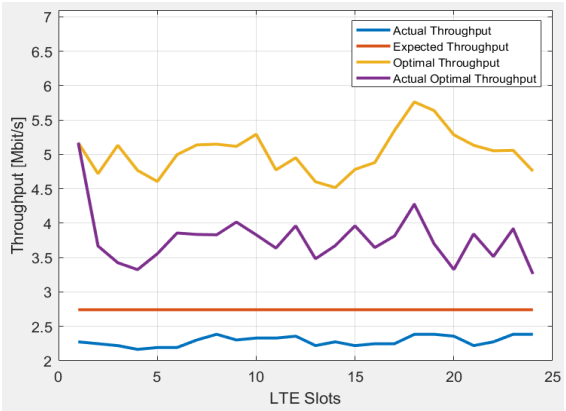

(b) RS_8.

Figure D.8 – Dense Deployment Throughput Curves for Individual Reference Signals.

References

[3GPP13d] 3GPP, *Technical Specification Group Radio Access Network; Study on Small Cell enhancements for E-UTRA and E-UTRAN; Higher layer aspects (Release 12)*, TR 36.842, Ver. 12.0.0, http://www.3gpp.org/DynaReport/WiVsSpec--580044.htm, Dec. 2013.

[3GPP15a] 3GPP, *Technical Specification Group Radio Access Network; Scenarios and requirements for small cell enhancements for E-UTRA and E-UTRAN (Release 13)*, TR 36.932, Ver. 13.0.0, http://www.3gpp.org/ftp/Specs/html-info/36932.htm, Dec. 2015.

[3GPP15b] 3GPP, *Technical Specification Group Services and System Aspects; Quality of Service (QoS) concept and architecture (Release 13)*, TS 23.107, Ver. 13.0.0 www.3gpp.org/dynareport/23107.htm, Dec. 2015.

[3GPP16a] 3GPP, LTE, http://www.3gpp.org/technologies/keywords-acronyms/98-lte, Nov. 2016.

[3GPP16b] 3GPP, *LTE-Advanced*, http://www.3gpp.org/technologies/keywords-acronyms/97-lte-advanced, Nov. 2016.

[3GPP16c] 3GPP, *LTE and the Internet of Things*, http://www.3gpp.org/news-events/3gpp-news/1607-iot, Nov. 2016.

[3GPP16d] 3GPP, *Evolved Universal Terrestrial Radio Access (E-UTRA) and Evolved Universal Terrestrial Radio Access Network (E-UTRAN); Overall description; Stage 2 (Release 13)*, TS 36.300, Ver. 13.5.0, www.3gpp.org/dynareport/36300.htm, Sep. 2016.

[3GPP16e] 3GPP, *HetNet/Small Cells*, http://www.3gpp.org/hetnet, Nov. 2016.

[3GPP16f] 3GPP, *Technical Specification Group Services and System Aspects; Policy and charging control architecture (Release 14)*, TS 23.203, V14.2.0, www.3gpp.org/DynaReport/23203.htm, Dec.16.

[3GPP17a] 3GPP, *Technical Specification Group Radio Access Network; Evolved Universal Terrestrial Radio Access (E-UTRA); Physical channels and modulation (Release 14)*, TS 36.211, V14.2.0, www.3gpp.org/dynareport/36211.htm, Mar. 2017.

[3GPP17b] 3GPP, *Technical Specification Group Radio Access Network; Evolved Universal Terrestrial Radio Access (E-UTRA); Physical layer procedures (Release 14)*, TS 36.213, V14.3.0, www.3gpp.org/dynareport/36942.htm, June 2017.

[3GPP17c] 3GPP, *Technical Specification Group Radio Access Network; Evolved Universal Terrestrial Radio Access (E-UTRA); Radio Frequency (RF) system scenarios (Release 14)*, TR 36.942, V14.0.0, www.3gpp.org/dynareport/36942.htm, Mar. 2017.

[ACGB13] I.F. Akyildiz, E. Chavarria-Reyes, D.M. Gutierrez-Estevez, R. Balakrishnan, and J.R. Krier, “Enabling next generation small cells through femtorelays”, *Physical Communication*, Vol.9, No.1, Dec. 2013, pp. 1-15.

[AD17] Analog Devices, “*AD9361: RF Agile Transceiver*”, AD9361 datasheet, Sep. 2013 [Last content update: Apr. 2017].

[ALHD14] F. Alfarhan, R. Lerbour, Y.L. Helloco, and G. Donnard, “Analysis of Practical Frequency Selective Scheduling Algorithms in LTE Networks”, *IEEE 80th Vehicular Technology Conference (VTC Fall*), Vancouver, Canada, Dec. 2014.

[ARM10] ARM, "AMBA 4 AXI4-Stream Protocol," AXI4-Stream datasheet 2010.

[BaFr15] M. Barberis, and G. Freeland, *Understanding and Demodulating LTE Signals*, Technical Article, MathWorks, Natick, MA, USA, 2015 (https://www.mathworks.com/company/newsletters/articles/understanding-and-demodulating-lte-signals.html).

[BaKo13] Y. Barayan, and I. Kostanic, “Performance Evaluation of Proportional Fairness Scheduling in LTE”, *World Congress on Engineering and Computer Science 2013 Vol II*, San Francisco, USA, Oct. 2013.

[BEEc16a] BEEcube – A National Instruments Company, *Getting started with the MegaBEE Revision F02, Firmware v1.1.2*, Santa Clara, CA, USA, 2017.

[BEEc16b] BEEcube – A National Instruments Company, *MegaBEE User Manual Revision F02, Firmware v1.1.2*, Santa Clara, CA, USA, 2017.

[BEEc16c] BEEcube – A National Instruments Company, “MegaBEE™ Datasheet”, MegaBEE Datasheet, 2016 [Last Revised: Mar. 2016].

[BEEc17a] BEEcube – A National Instruments Company, *BEEcube Platform Studio Version 5.5 User Manual*, Santa Clara, CA, USA, 2017.

[BEEc17b] BEEcube – A National Instruments Company, *Operation Guidance for XGE UDP Uplink Design (Draft v0.5)*, Internal Report, Santa Clara, CA, USA, May 2017.

[BoLe16] T.E. Bogale, and L.B. Le, “Massive MIMO and Millimeter Wave for 5G Wireless HetNet: Potentials and Challenges”, *IEEE Vehicular Technology Magazine*, Vol.11, No.1, Feb. 2016, pp. 64-75.

[Cisc16] Cisco, *Cisco Visual Networking Index (VNI): Mobile Data Traffic Update, 2015–2020*, White Paper, Cisco Systems, San Jose, California, USA, Feb. 2016.

[Corr16] L.M. Correia, *Mobile Communication Systems – Lecture Notes*, Instituto Superior Técnico, University of Lisbon, Lisbon, Portugal, 2016.

[Cox12] C. Cox, *An Introduction to LTE: LTE, LTE-Advanced, SAE and 4G Mobile Communications,* Wiley, Chichester, UK, 2012.

[DaPS14] E. Dahlman, S. Parkvall, and J. Sköld, *4G: LTE/LTE-Advanced for Mobile Broadband*,

Elsevier, Oxford, UK, 2014.

[Digi17a] Digikey, https://www.digikey.com/products/en?mpart=132169&v=115, Sep. 2017.

[GeRK12] C. Gessner, A. Roessler, and M. Kottkamp, *UMTS Long Term Evolution (LTE) Technology Introduction*, Internal Report, Rohde & Schwarz, Munich, Germany, 2012 (https://cdn.rohde-schwarz.com/pws/dl_downloads/dl_application/application_notes/ 1ma111/ 1MA111_4E_LTE_technology_introduction.pdf).

[GRMM10] A. Ghosh, R. Ratasuk, B. Mondal, N. Mangalvedhe, and T. Thomas, "LTE-Advanced: Next-Generation Wireless Broadband Technology", *IEEE Wireless Communications*, Vol. 17, No.3, June 2010, pp. 10-22.

[GSSS03] D. Gesbert, M. Shafi, D. Shiu, P.J. Smith, and A. Naguib, "From Theory to Practice: An Overview of MIMO Space–Time Coded Wireless Systems", *IEEE Journal on Selected Areas in Communications*, Vol. 21, No. 3, Apr. 2003, pp. 281-302.

[HHBD13] K. Hosseini, J. Hoydis, S. ten Brink, and M. Debbah, "Massive MIMO and Small Cells: How to Densify Heterogeneous Networks", in *2013 IEEE International Conference on Communications (ICC)*, Budapest, Hungary, June 2013.

[IwTN10] M. Iwamura, H. Takahashi, and S. Nagata, "Relay Technology in LTE-Advanced", *NTT DOCOMO Technical Journal*, Vol.12, No.2, Sep. 2010, pp. 29-36.

[JLSH15] A. H. Jafari, D. López-Pérez, H. Song, H. Claussen, L. Ho, and J. Zhang, "Small cell backhaul: challenges and prospective solutions", *EURASIP Journal on Wireless Communications and Networking*, Vol. 2015, No. 1, Aug. 2015, pp. 1-18.

[LAPI17] LocationAPI, http://locationapi.org/, July 2017.

[LETM14] E.G. Larsson, O. Edfors, F. Tufvesson, and TL. Marzetta, "Massive MIMO for Next Generation Wireless Systems", *IEEE Communications Magazine*, Vol. 52, No. 2, Feb. 2014, pp. 186-195.

[LLSA14] L. Lu, G.Y. Li, A.L. Swindlehurst, A. Ashikhmin, and R. Zhang, "An Overview of Massive MIMO: Benefits and Challenges", *IEEE Journal of Selected Topics in Signal Processing*, Vol. 8, No. 5, Oct. 2014, pp. 742-758.

[Mart13] J. Martins, *Impact of MIMO and Carrier Aggregation in LTE-Advanced*, M.Sc. Thesis, Instituto Superior Técnico, Technical University of Lisbon, Lisbon, Portugal, 2015.

[Math17] MathWorks, *LTE System Toolbox™ User's Guide*, Natick, MA, USA, 2017.

[MEJX09] K. Manolakis, D.M.G. Estévez, V. Jungnickel, W. Xu, and C. Drewes, "A Closed Concept for Synchronization and Cell Search in 3GPP LTE Systems", in *Wireless Communications and Networking Conference (WCNC 2009)*, Budapest, Hungary, Apr. 2009.

[MNGu14] Mobile Network Guide, *Iphone Field Test Mode*, Powertec Telecommunications, Australia, 2014 (http://www.mobilenetworkguide.com.au/pdf/Apple-iPhone-Field-Test-Mode.pdf).

[NFMN06] NTT DoCoMo, Fujitsu, Mitsubishi Electric Corporation, NEC, QUALCOMM Europe, Sharp, and Toshiba Corporation, *R1-060039: Adaptive Modulation and Channel Coding Rate Control for Single-antenna Transmission in Frequency Domain Scheduling in E-UTRA Downlink*, 3GPP TSG RAN WG1, LTE ad-hoc meeting, Helsinki, Finland, Jan. 2006.

[NI17a] National Instruments, *BPS xGE IP Updates – Prepared for Nokia-US*, Internal Report, Austin, TX, USA, Apr. 2017.

[NI17b] National Instruments, *Block Diagram of nanoBEE Subsystem (XGE UDP Uplink)*, Internal Report, Austin, TX, USA, May 2017.

[OSRF09] M. Olsson, S. Sultana, S. Rommer, L. Frid, and C. Mulligan, *SAE and the Evolved Packet Core*, Academic Press, Oxford, UK, 2009.

[Past13] Pasternack, "Flexible RG316 Coax Single Shielded with Tan FEP Jacket", RG316 SMA Cable Datasheet, 2013.

[Pere13] J. Pereira, *Small Cell Deployment Evaluation on LTE*, M.Sc. Thesis, Instituto Superior Técnico, Technical University of Lisbon, Lisbon, Portugal, 2015.

[RaSo16] N. Rajatheva, and E.S. Sousa, "*Hybrid Beamforming for Massive MIMO Backhaul (Working Title)*", University of Toronto, Toronto, Ontario, Canada, Feb. 2016.

[RPLL13] F. Rusek, D. Persson, B.K. Lau, E.G. Larsson, T.L. Marzetta, O. Edfors, and F. Tufvesson, "Scaling Up MIMO: Opportunities and Challenges with Very Large Arrays", *IEEE Signal Processing Magazine*, Vol. 30, No. 1, Jan. 2013, pp. 40-60.

[Rumn08] M. Rumney, *3GPP LTE: Introducing Single-Carrier FDMA*, Internal Report, Agilent Technologies, USA, 2008 (http://cp.literature.agilent.com/litweb/pdf/5989-7898EN.pdf).

[SaHa16] S. Saleem, and M. Haneef, "A review of techniques to avoid cross-tier and co-tier interference in femtocell networks", *Journal of Engineering Research*, Vol. 4, No. 3, Oct. 2016, pp. 57-84.

[SC17a] Statistics Canada, *2016 Census: Population and Dwelling Counts,* Public Consultation, Toronto, Canada, 2017 (https://www1.toronto.ca/City%20Of%20Toronto/City%20Planning/SIPA/Files/pdf/C/2016%20Census%20Backgrounder%20Population%20Dwellings%202017%2002%2009.pdf)

[SC17b] Statistics Canada, *2011 Census: Ward 20 – Trinity-Spadina*, Public Consultation, Toronto, Canada, 2017 (https://www1.toronto.ca/City%20Of%20Toronto/City%20Planning/Wards/Files/pdf/W/Ward%2020%20Profile%202011.pdf)

[SC17c] Statistics Canada, *2011 Census: Ward 27 – Toronto Centre-Rosedale*, Public Consultation, Toronto, Canada, 2017 (https://www1.toronto.ca/City%20Of%20Toronto/City%20Planning/Wards/Files/pdf/W/Ward%2027%20Profile%202011.pdf)

[SiBG15] M. Simsek, M. Bennis, and I. Guvenc, "Mobility management in HetNets: a learning-based perspective", *EURASIP Journal on Wireless Communications and Networking*, Vol. 2015,

No.1, Feb. 2015, pp. 1-26.

[Taog17] Taoglas Antenna Solutions, *TG.10.0113 Triton dipole Antenna Specification*, Last Revised: Apr. 2017.

[Toyo17] Toyota, https://www.toyota.com/camry/features/dimensions/2514/2532/2540, Sep. 2017.

[TrSS12] T.Tran, Y. Shin, and O. Shin, “Overview of enabling technologies for 3GPP LTE-advanced”, *EURASIP Journal on Wireless Communications and Networking*, Vol. 2012, No. 1, Jan. 2012, pp. 1-12.

[UTor17] University of Toronto, https://www.utoronto.ca/, Sep. 2017.

[Wils02] R. Wilson, *Propagation Losses Through Common Building Materials - 2.4 GHz vs 5 GHz*, E10589, Magis Networks, San Diego, CA, USA, Aug. 2002.

[Xili15] Xilinx, *Vivado Design Suite Reference Guide Model-Based DSP Design Using System Generator UG958 (v2015.2)*, San José, CA, USA 2015.

[YKSM15] H. Yasuda, A. Kishida, J. Shen, Y. Morihiro, Y. Morioka, S. Suyama, A. Yamada, Y. Okumura, and T. Asai, “A Study on Moving Cell in 5G Cellular System”, in *2015 IEEE 82nd Vehicular Technology Conference (VTC2015-Fall)*, Boston, USA, Sep. 2015.